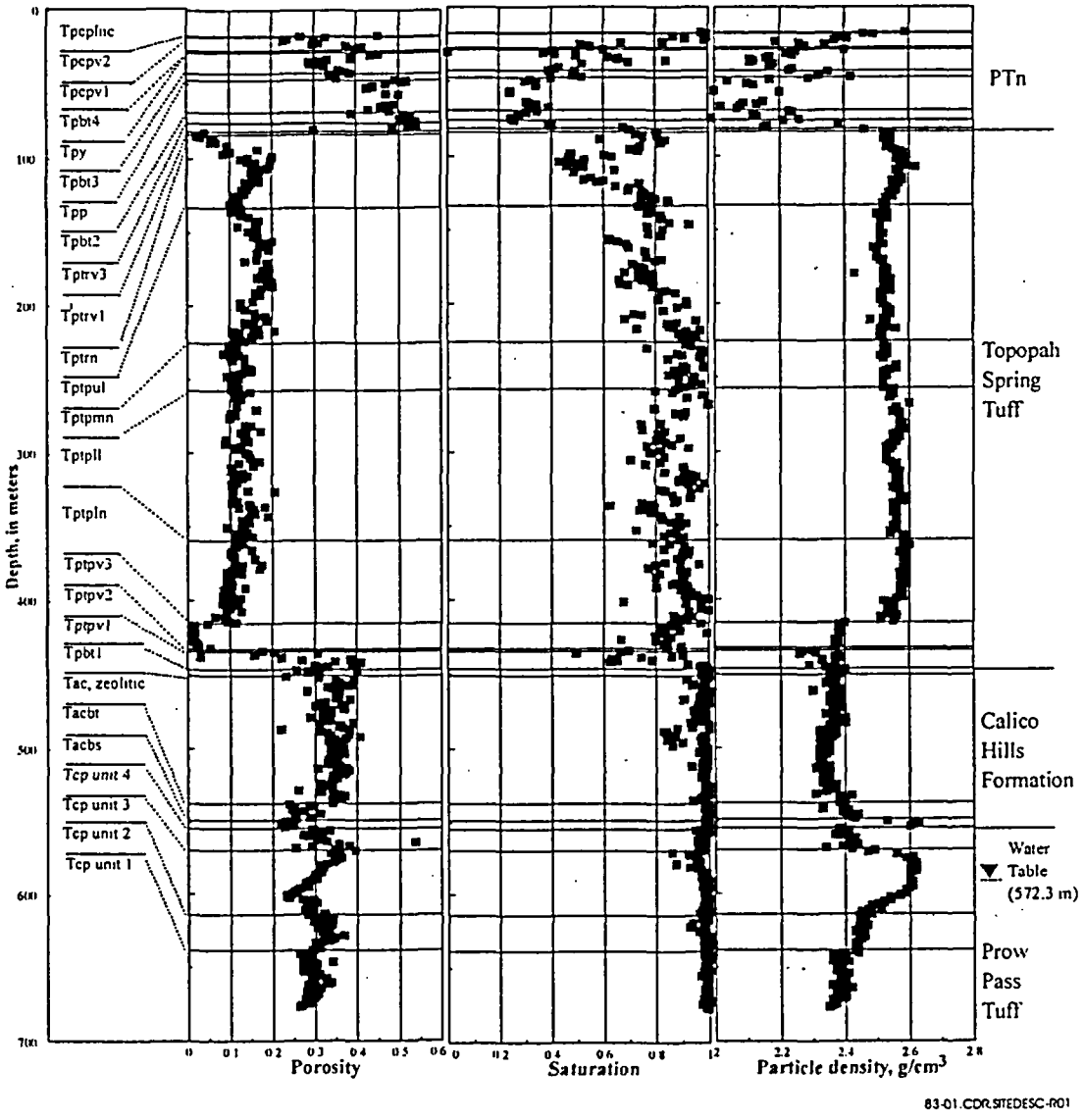

Source: Flint, L.E. (1998, Figure 4)

NOTE: Lithostratigraphic-unit assignments are from Engstrom and Rautman (1996), and Moyer and Geslin (1995).

Figure 8.3-1. Porosity, Saturation, and Particle Density with Depth for Borehole SD-9

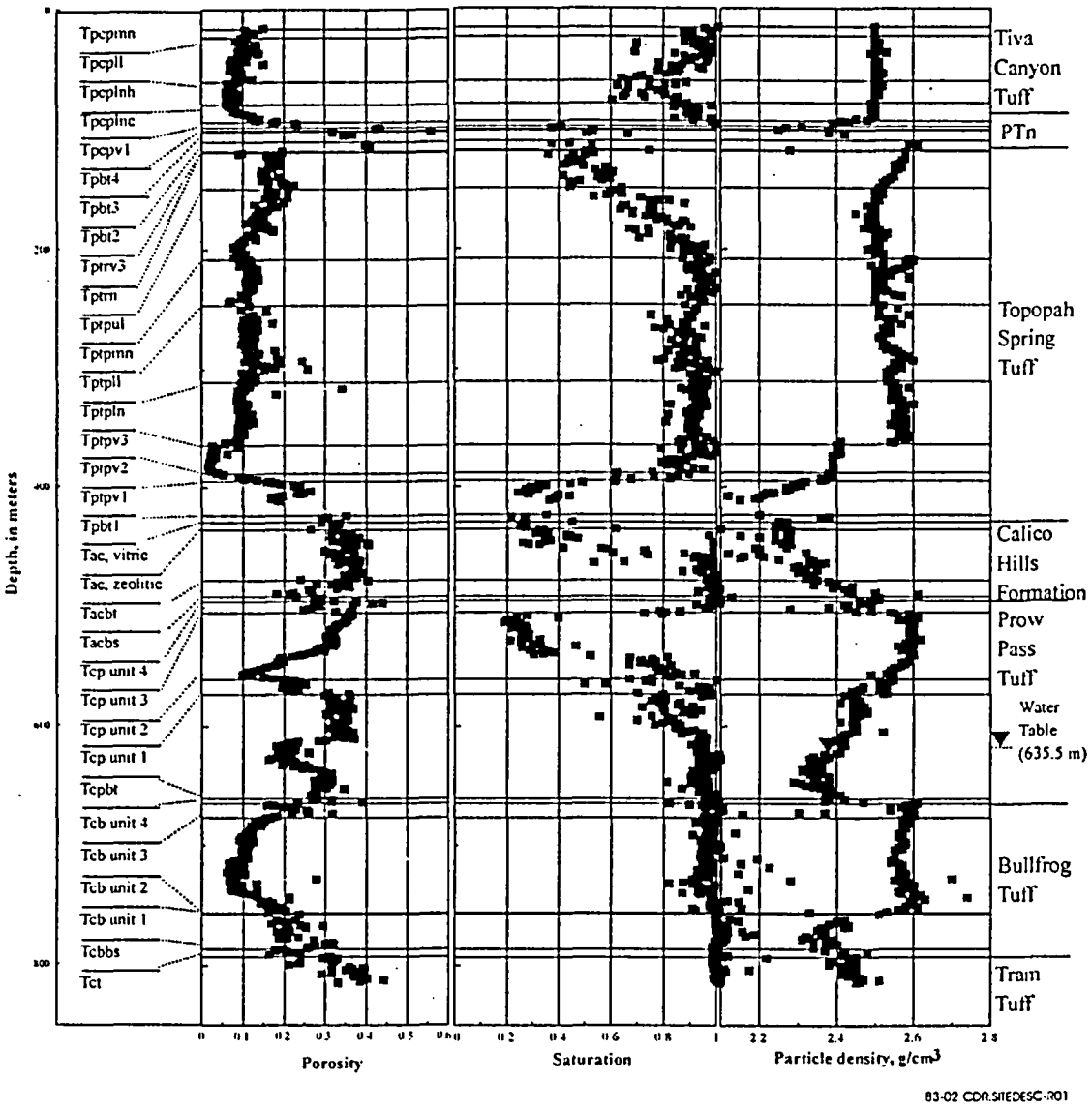

Source: Flint, L.E. (1998, Figure 3)

NOTE: Lithostratigraphic-unit assignments are from Rautman and Engstrom (1996).

Figure 8.3-2. Porosity, Saturation, and Particle Density with Depth for Borehole SD-7

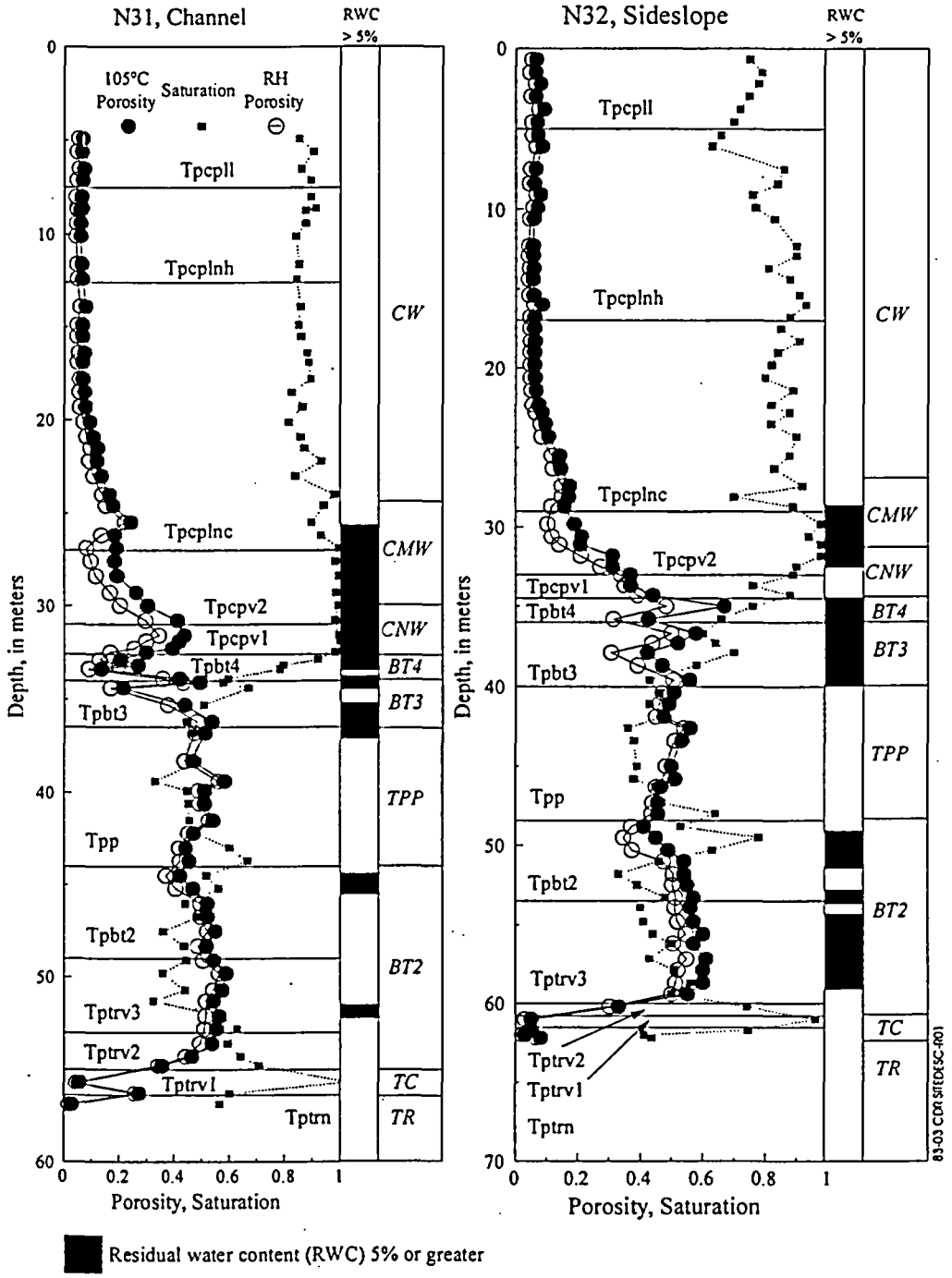

Source: Flint, L.E. (1998, Figures 7 and 10)

NOTE: Lithostratigraphic-unit assignments are from Moyer et al. (1996).

Figure 8.3-3. Porosity Calculated from Relative Humidity and 105°C Oven Drying, Saturation, and 5 Percent and Greater Residual Water Content of Samples for Boreholes N31 and N32

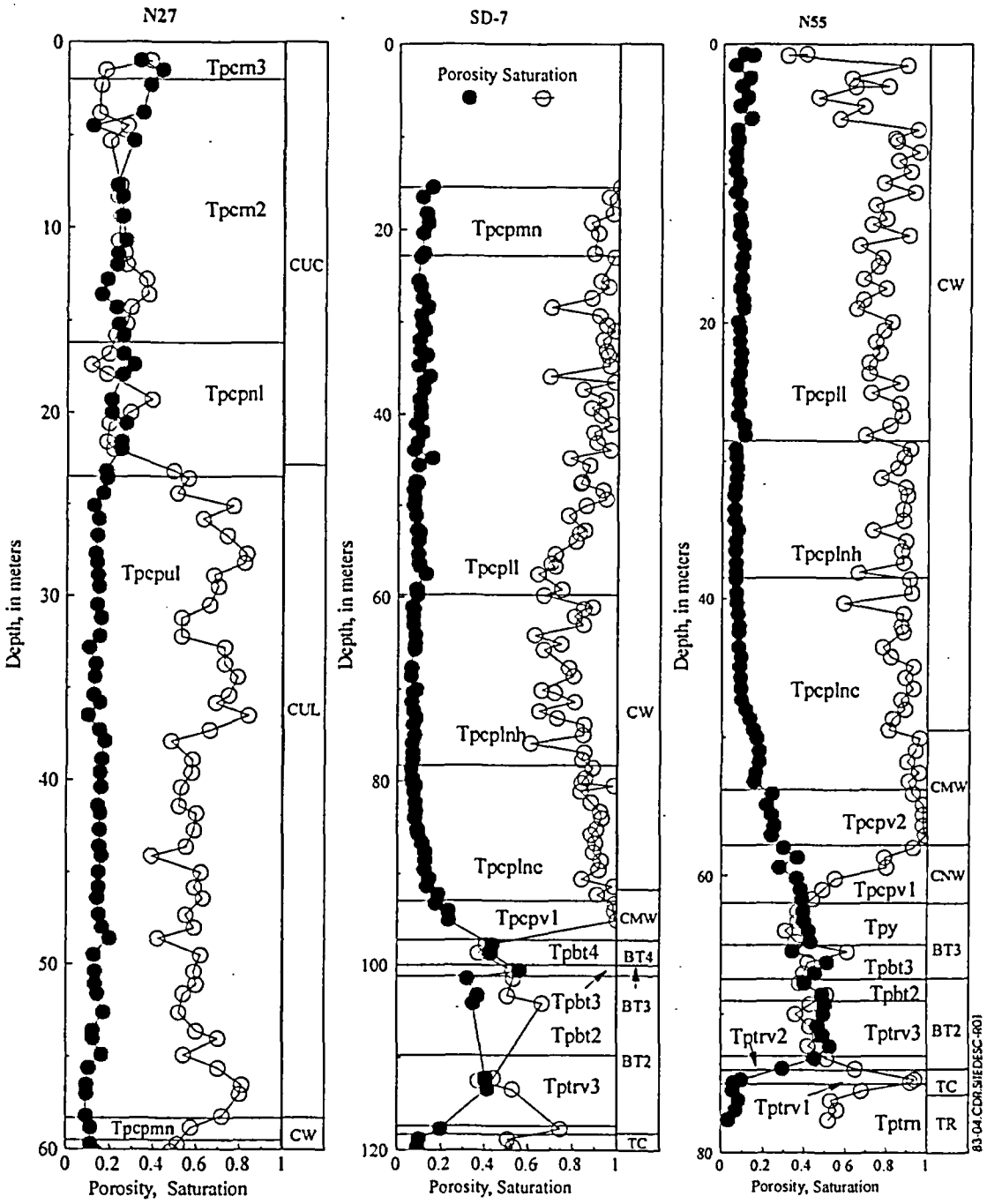

Source: Flint, L.E. (1998, Figures 5 and 6)

NOTE: Lithostratigraphic-unit assignments are from Rautman and Engstrom (1996), and Moyer et al. (1996).

Figure 8.3-4. Porosity and Saturation with Depth for Boreholes N27, SD-7, and N55, Indicating Properties of the Tiva Canyon Tuff and the Paintbrush Nonwelded Unit

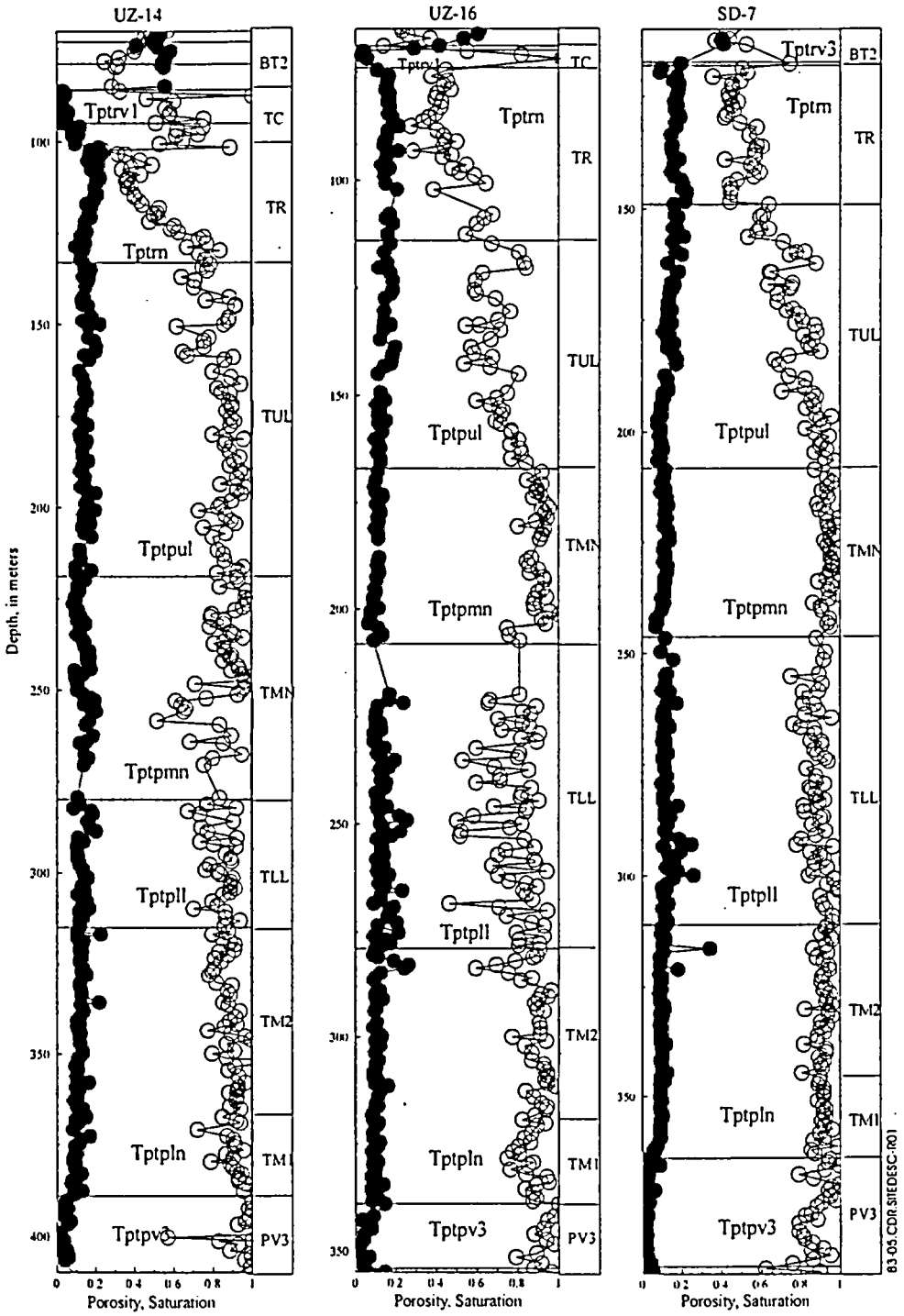

Source: Flint, L.E. (1998, Figure 8)

NOTE: Lithostratigraphic-unit assignments are from Rautman and Engstrom (1996), and Moyer et al. (1996).

Figure 8.3-5. Porosity and Saturation with Depth for Boreholes UZ-14, UZ-16, and SD-7, Indicating Properties of the Topopah Spring Tuff

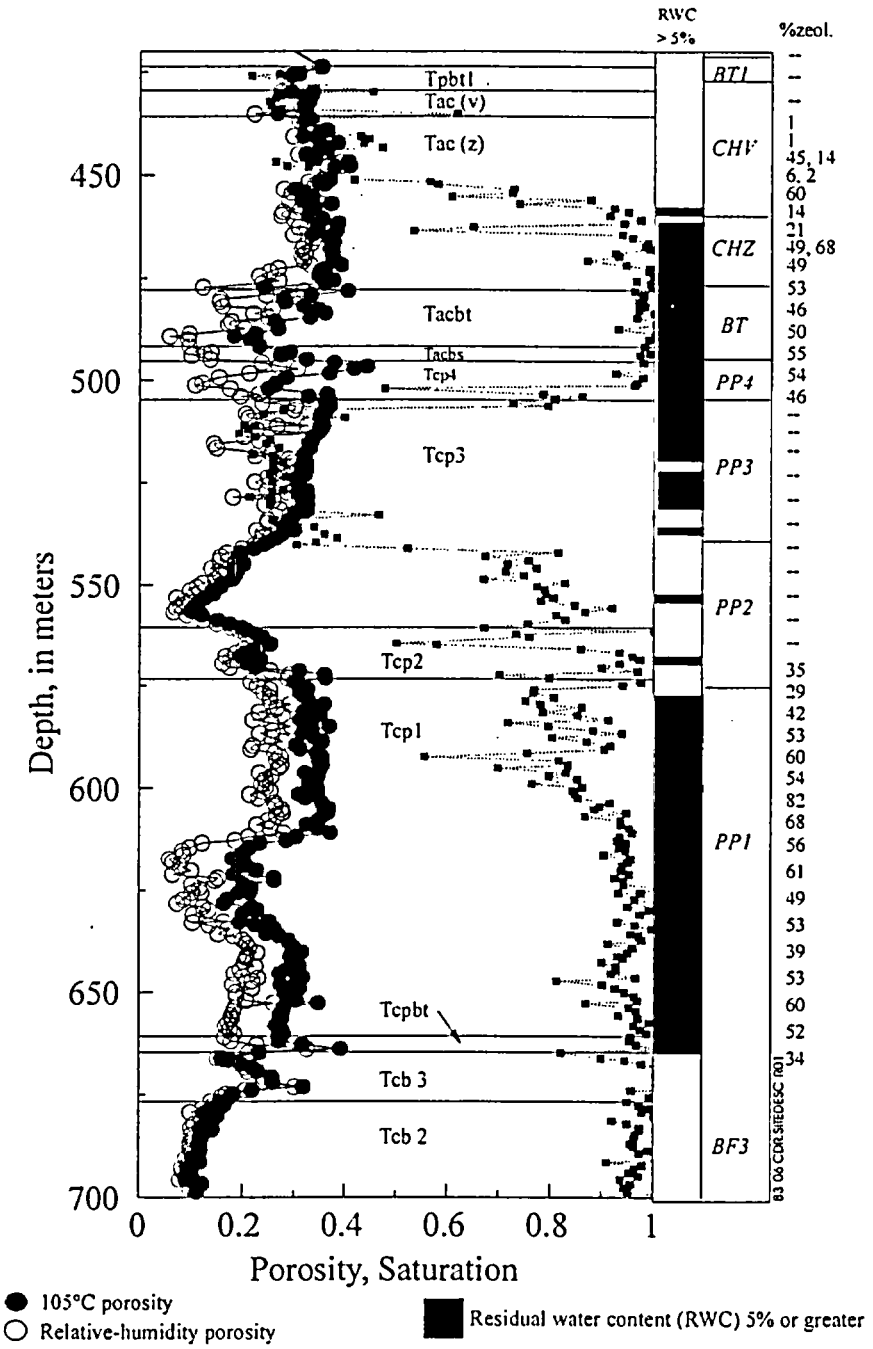

Source: Flint, L.E. (1998, Figures 9 and 10)

NOTE: Lithostratigraphic-unit assignments are from Rautman and Engstrom (1996).

Figure 8.3-6. Porosity Calculated from Relative Humidity and 105°C Oven Drying, Saturation, and 5 Percent and Greater Residual Water Content of Samples of Rocks below the Basal Vitrophyre of the Topopah Spring Tuff in Borehole SD-7

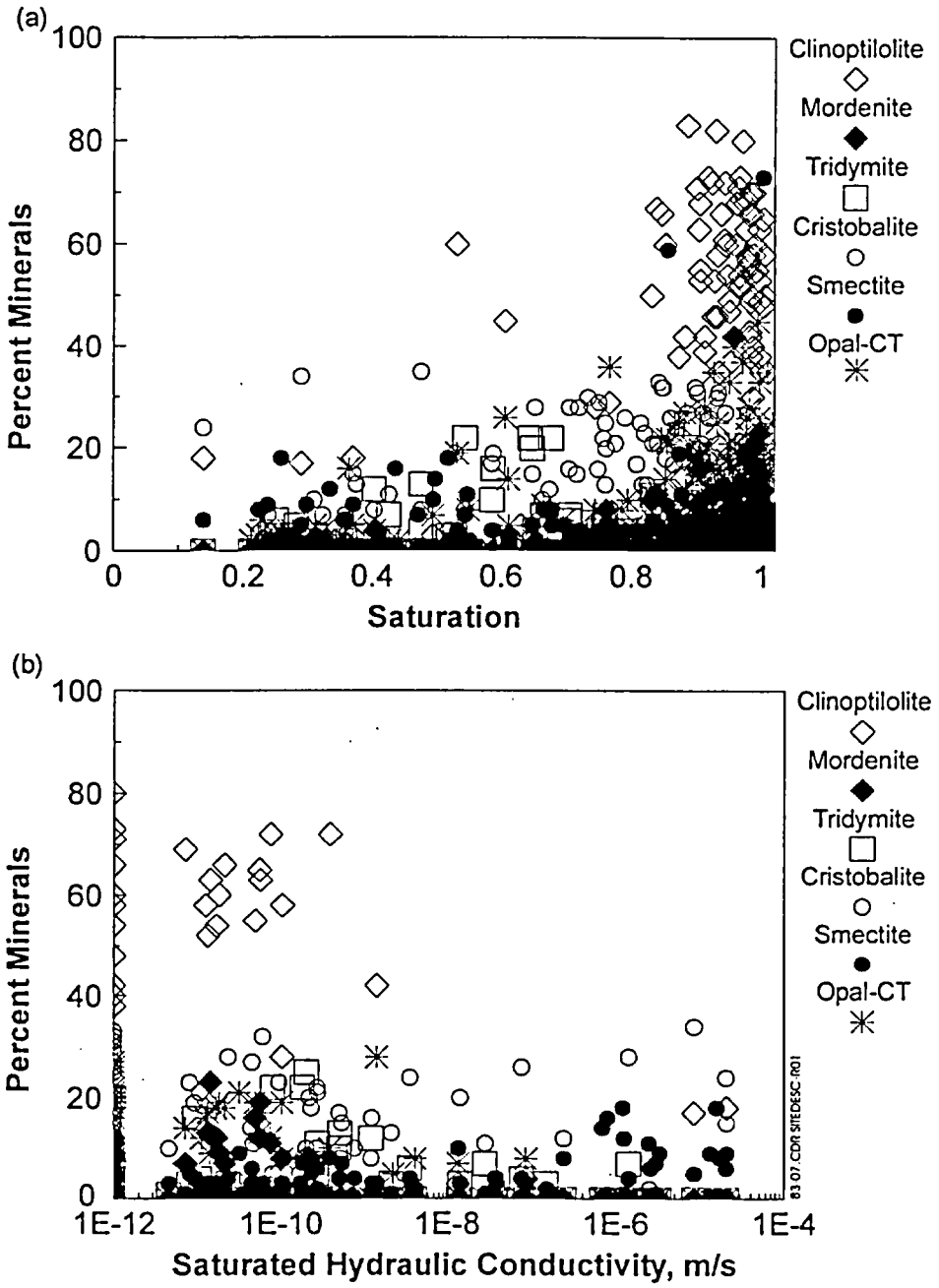

DTNs: GS960908312231.004, LADV831321AQ97.001

NOTE: Plot (a) shows the degree of saturation; plot (b) the saturated hydraulic conductivity.

Figure 8.3-7. Mineral Content for Six Minerals in Borehole SD-7 as a Function of Degree of Saturation and Saturated Hydraulic Conductivity

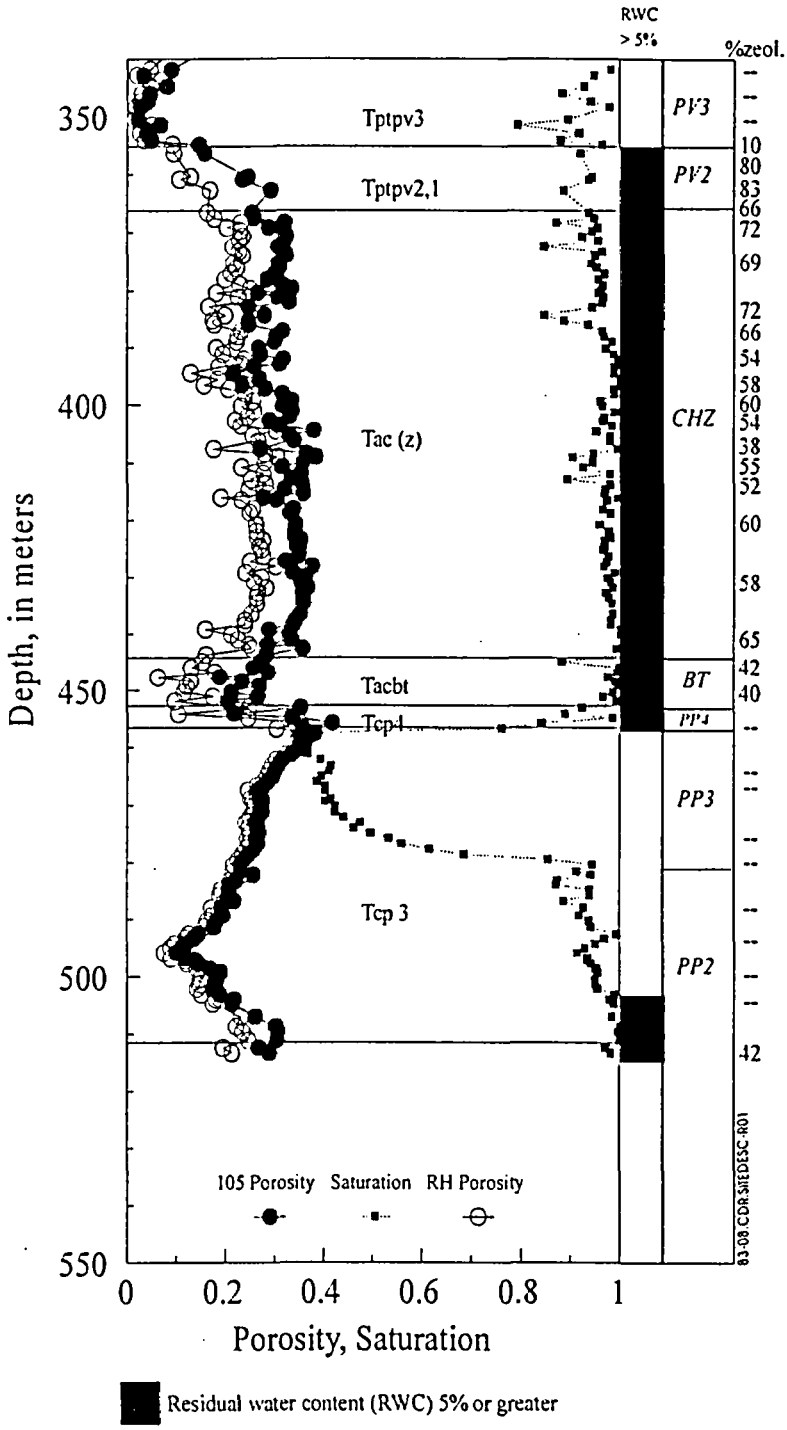

Source: Flint, L.E. (1998, Figure 9)

NOTE: Lithostratigraphic-unit assignments are from Moyer et al. (1996).

Figure 8.3-8. Porosity Calculated from Relative Humidity and 105°C Oven Drying, Saturation, and 5 Percent and Greater Residual Water Content of Samples of Rocks below the Basal Vitrophyre of the Topopah Spring Tuff in Borehole UZ-16

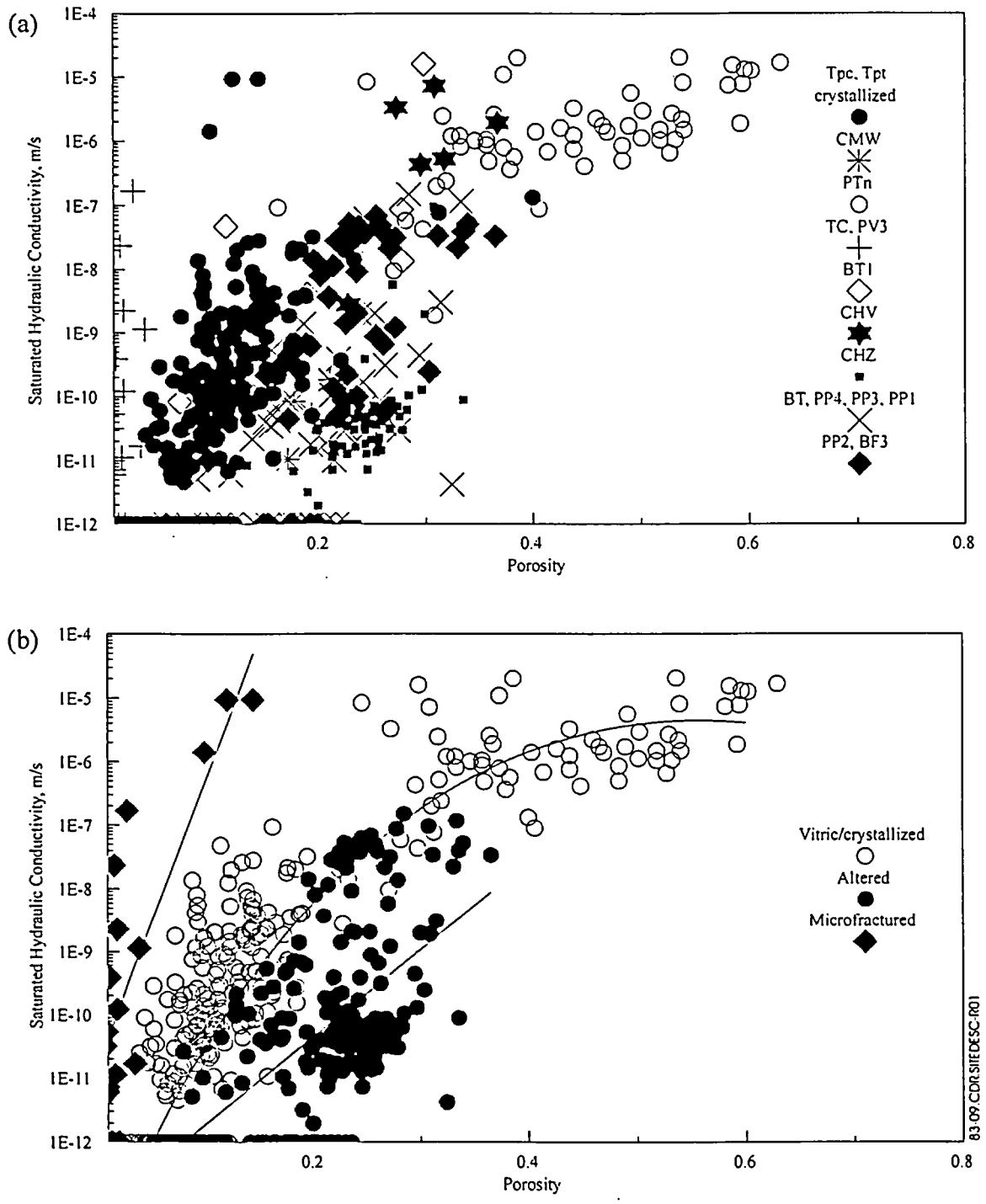

Source: Flint, L.E. (1998, Figure 12)

NOTES: Plot (a) is grouped by hydrologic unit; plot (b) by generalized rock type.
Values of 1 x 10^{-12} m/s are samples that had conductivities too low to measure.

Figure 8.3-9. Relationship between Porosity and Saturated Hydraulic Conductivity

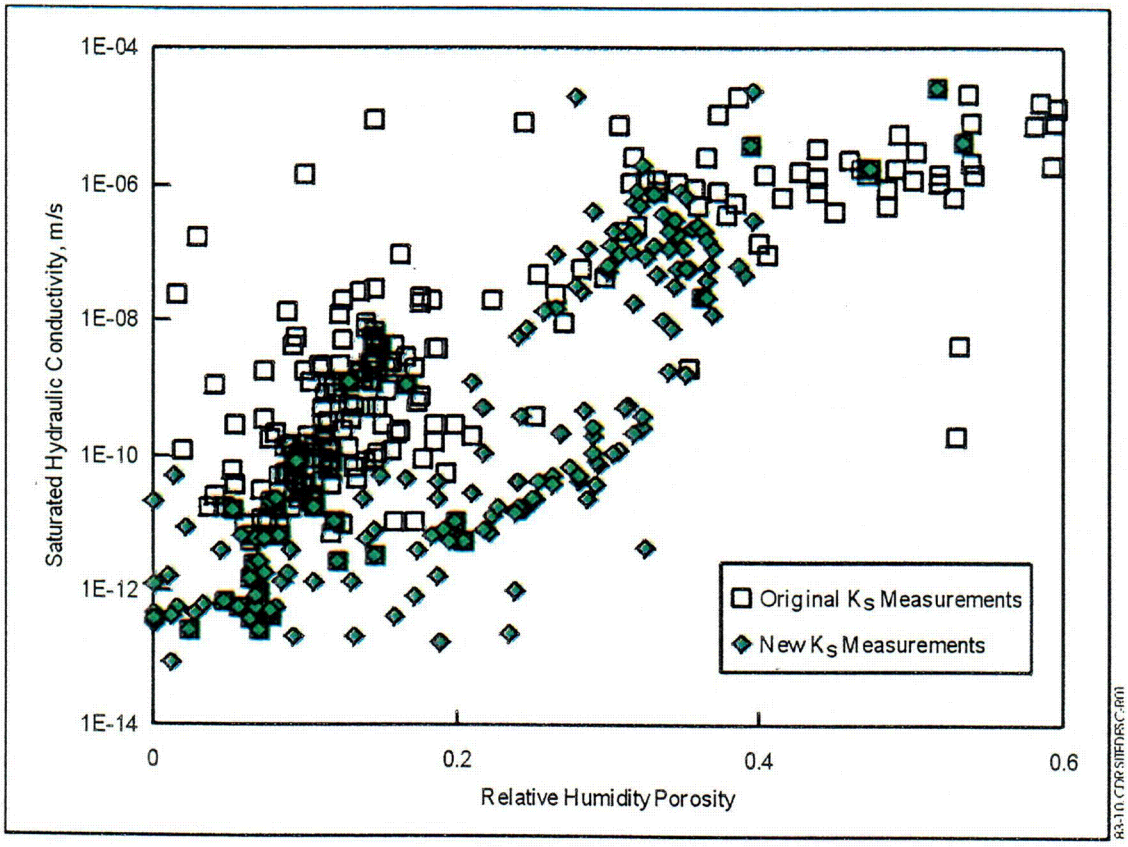

Source: Original K_s data from Flint, L.E. (1998, Figure 12)

Figure 8.3-10. Measured Saturated Hydraulic Conductivity (K_s) for Core Samples from Surface-Based Boreholes versus Relative Humidity Porosity

C042

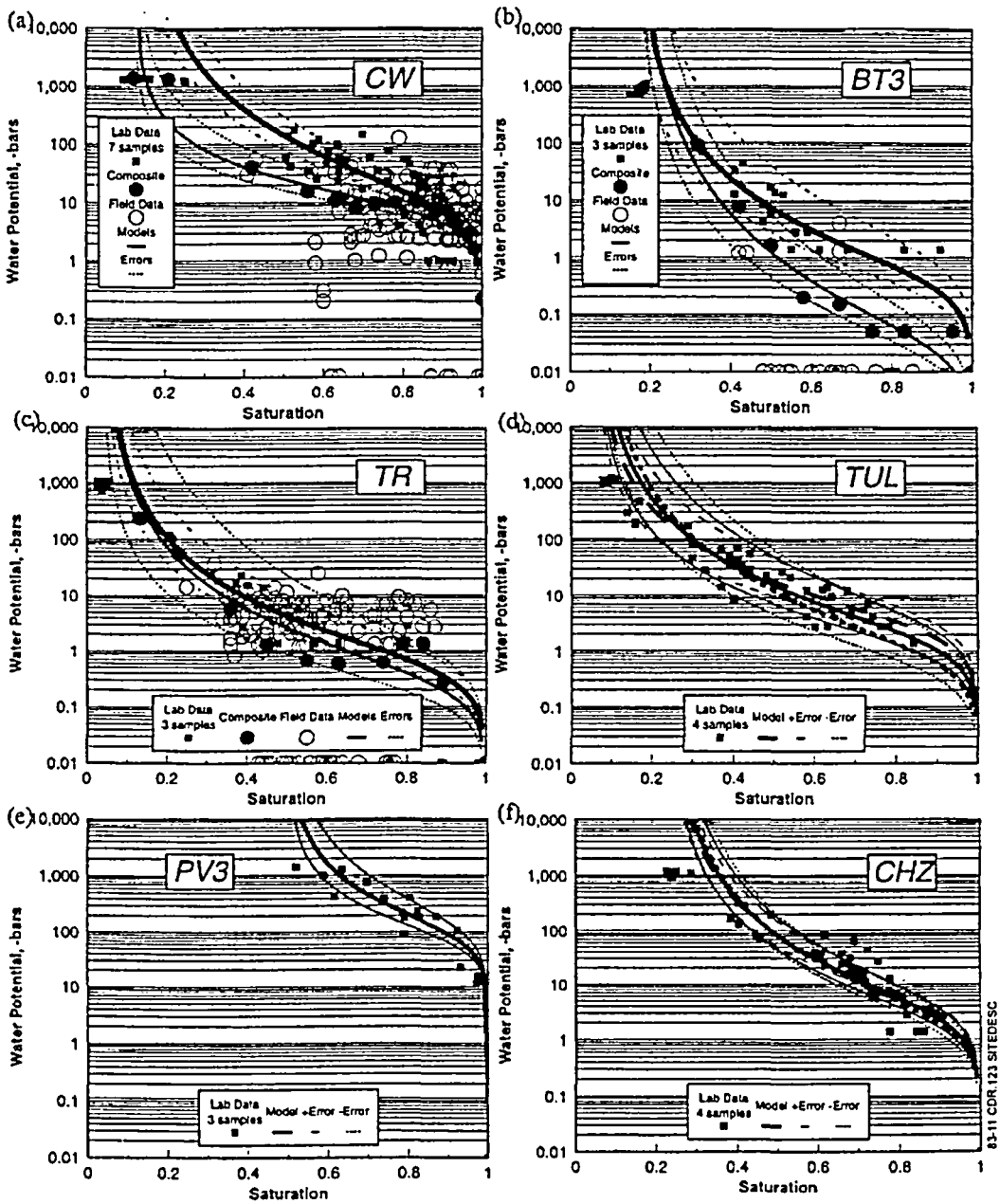

Source: Flint, L.E. (1998, Figure 13)

NOTE: Data sets for all units include laboratory measurements of core, whereas data sets for units CW, BT3, and TR also include field measurements.

Figure 8.3-11. Moisture Retention Curves for Core Samples from Six Hydrogeologic Units

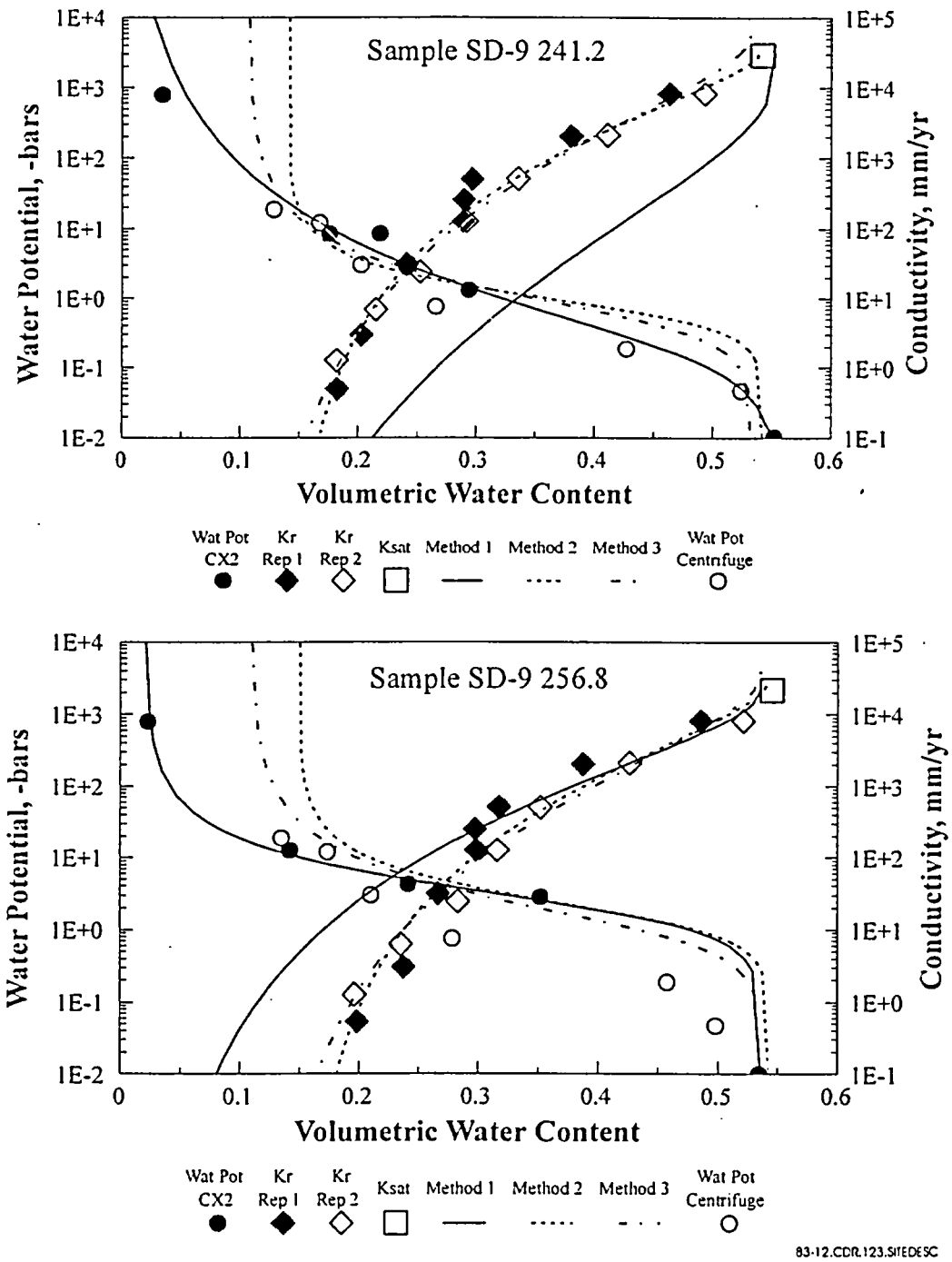

Source: Modified from Flint et al. (1999, Figure 3)

Figure 8.3-12. Measured Unsaturated Hydraulic Conductivity, and Modeled Estimates for Two Samples from Tpbt2

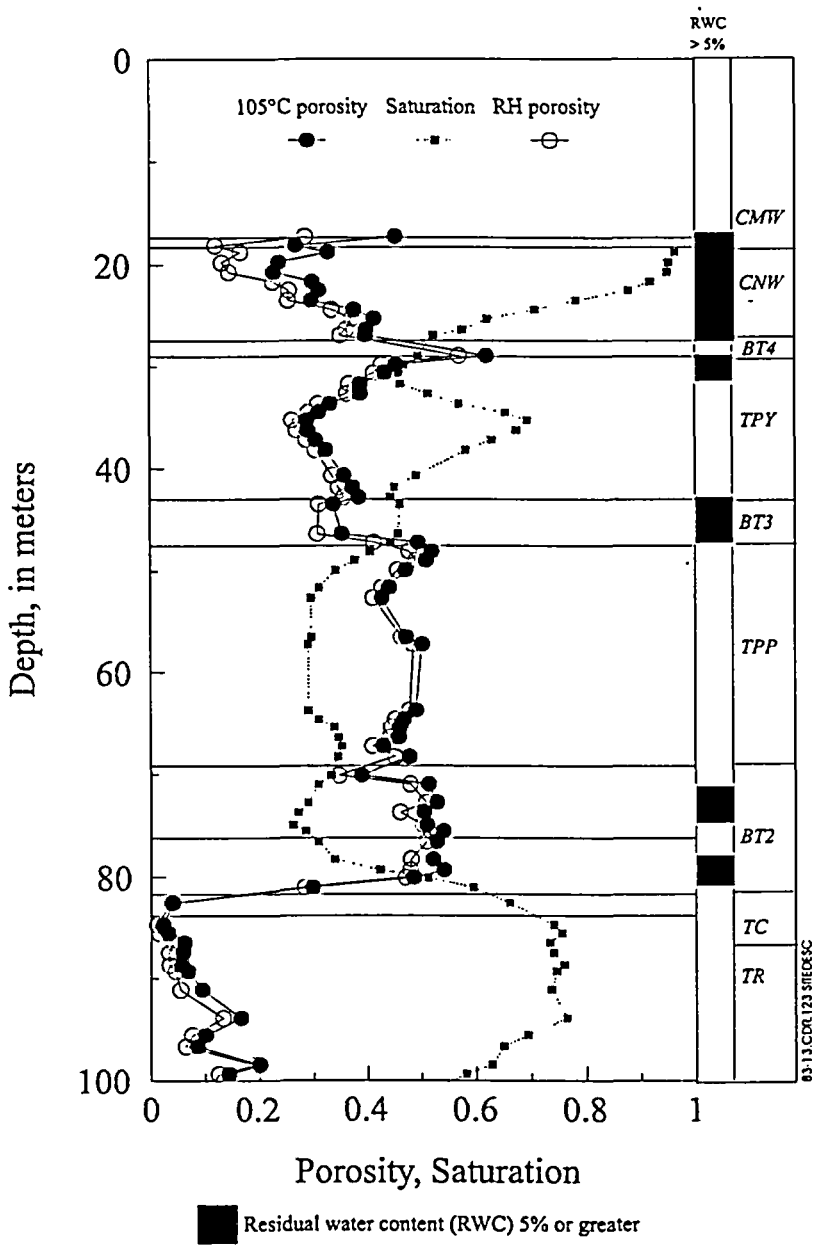

Source: Modified from Flint, L.E. (1998, Figure 7)

NOTE: Lithostratigraphic-unit assignments are from Engstrom and Rautman (1996).

Figure 8.3-13. Porosity Calculated from Relative Humidity and 105°C Drying, Saturation, and 5 Percent and Greater Residual Water Content of Samples from Borehole SD-9

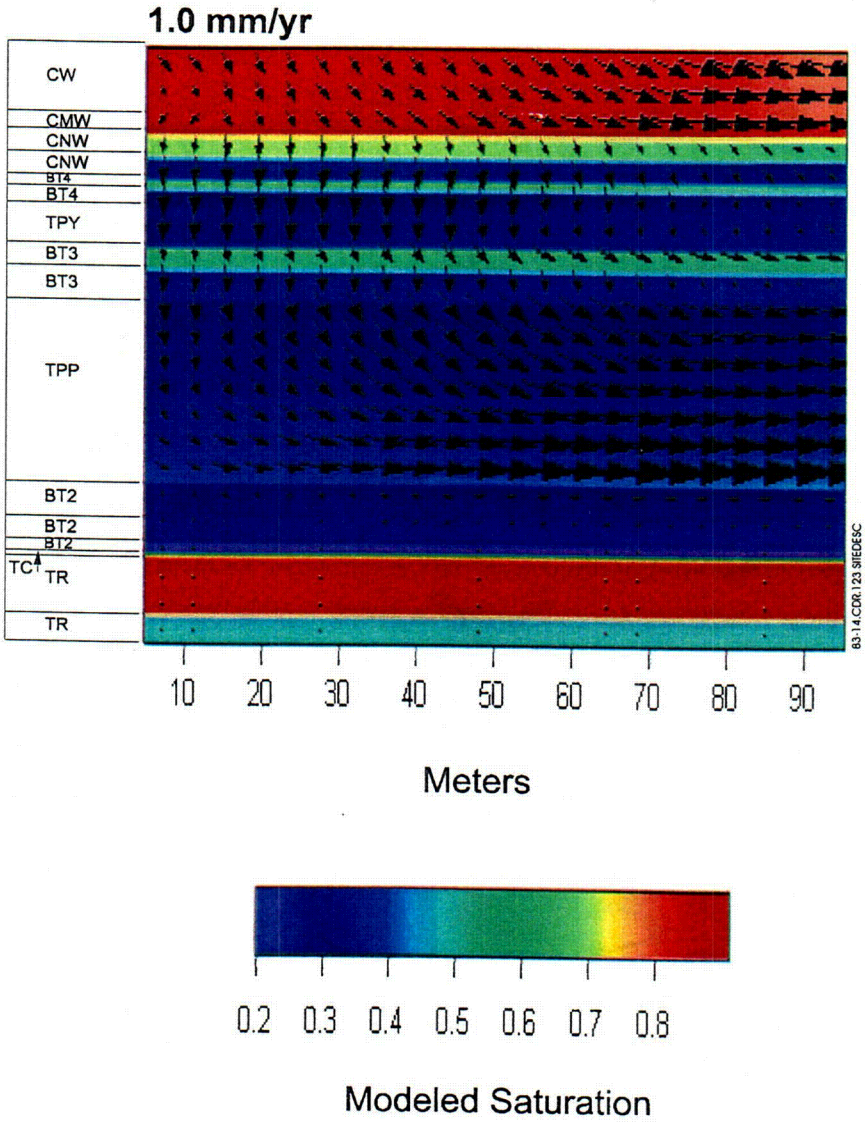

Source: Modified from Moyer, T.C. et al. (1996, Figure 48)

Figure 8.3-14. Simulated Saturation and Flow Direction for Model Layers with Properties of the Paintbrush Nonwelded Unit

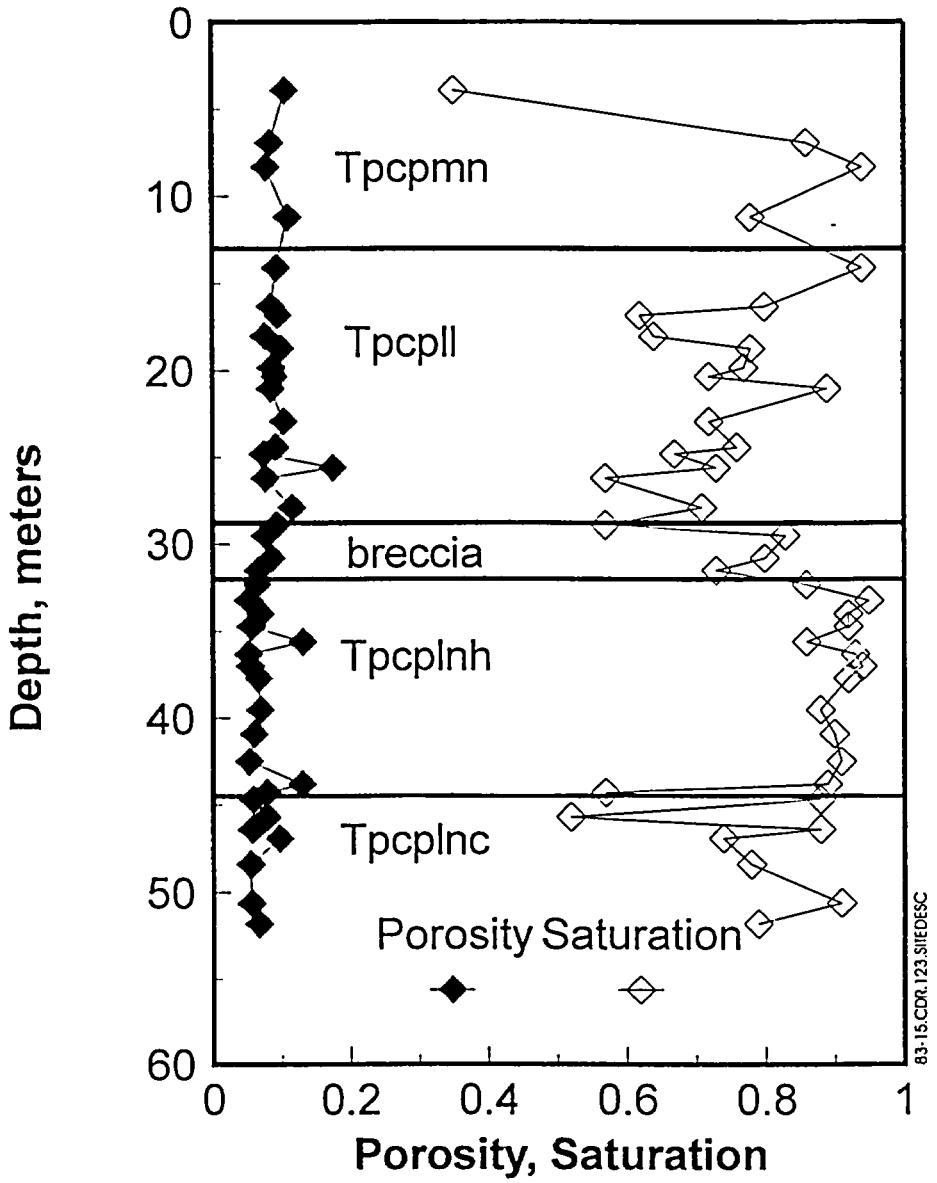

NOTE: Lithostratigraphic-unit assignments are from Moyer et al. (1996).

Figure 8.3-15. Porosity and Saturation for Borehole N35, Which Penetrates the Brecciated Zone of the Ghost Dance Fault

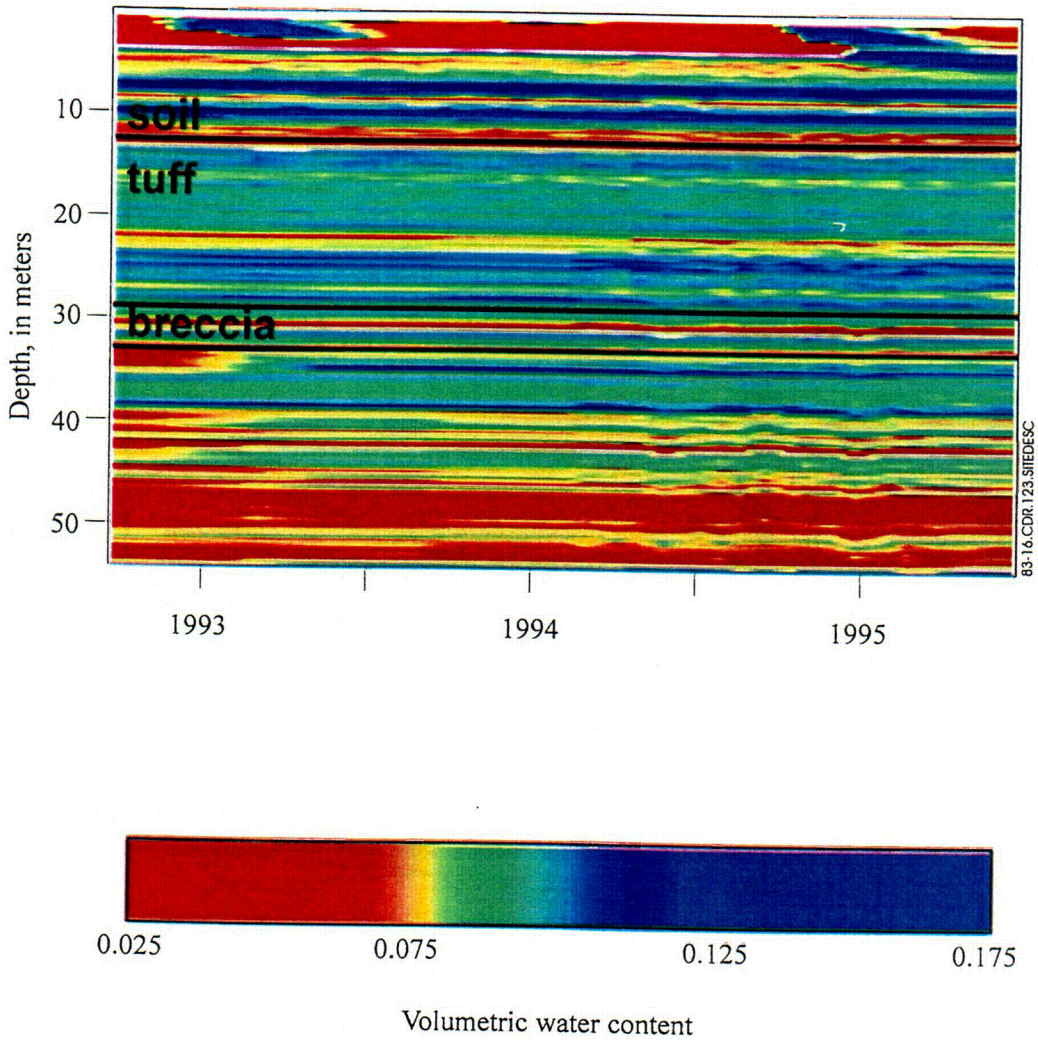

DTNs: GS940708312212.011, GS941208312212.017, GS950808312212.001, GS960108312212.001

Figure 8.3-16. Volumetric Water Content Changes with Time and Depth for Borehole N35 Located within the Ghost Dance Fault Zone

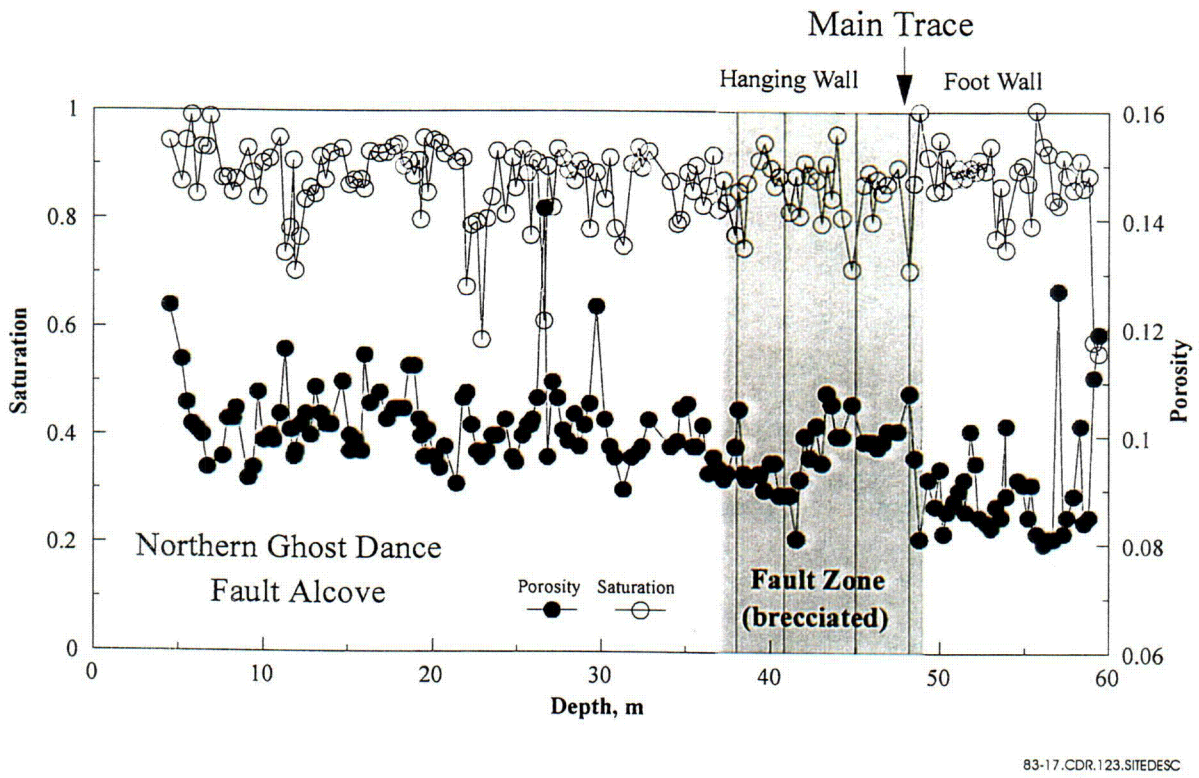

DTN: GS970208312231.003

Figure 8.3-17. Porosity and Saturation for Borehole ESF-NAD-GTB#1A in the Exploratory Studies Facility Northern Ghost Dance Fault Alcove

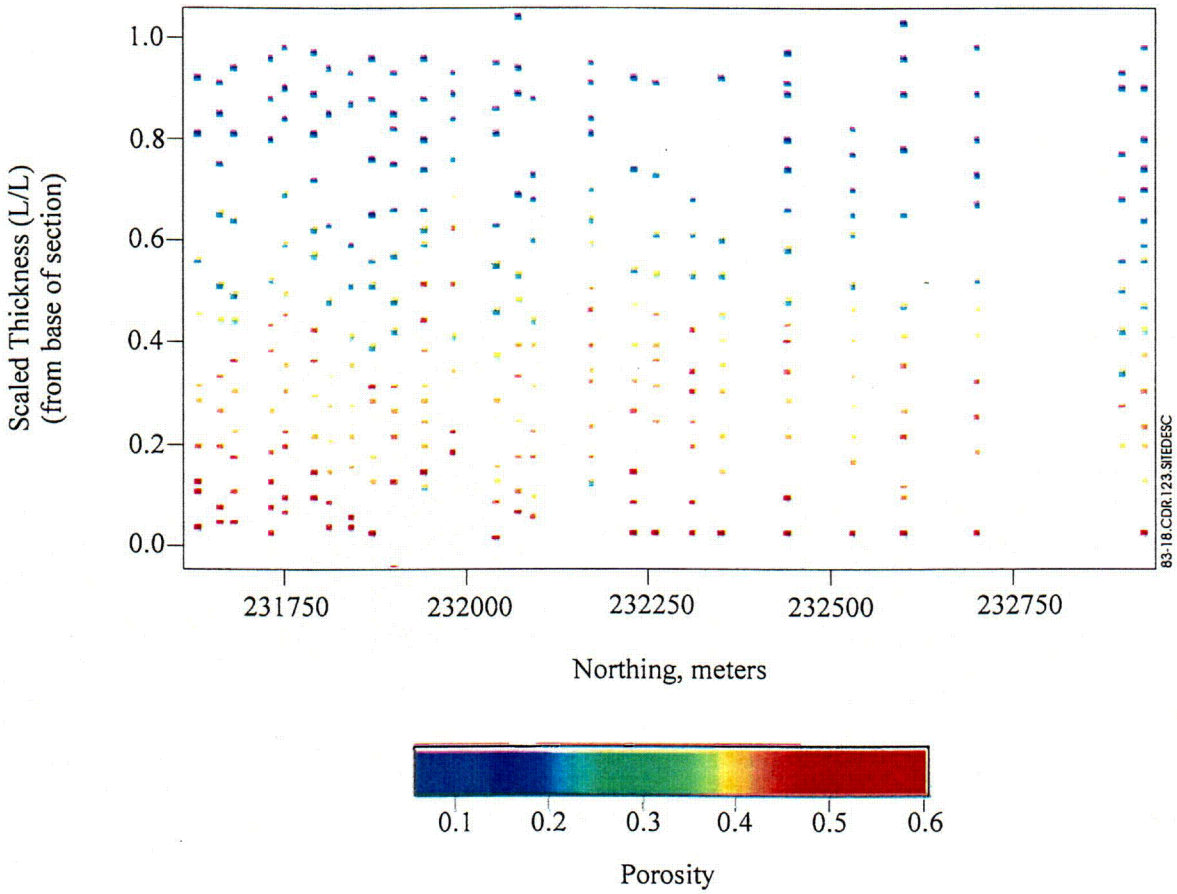

Source: Modified from Rautman et al. (1995, Figure 3)

Figure 8.3-18. Porosity of Samples Collected from 26 Vertical Transects along the Solitario Canyon Exposure of the Base of the Tiva Canyon Tuff

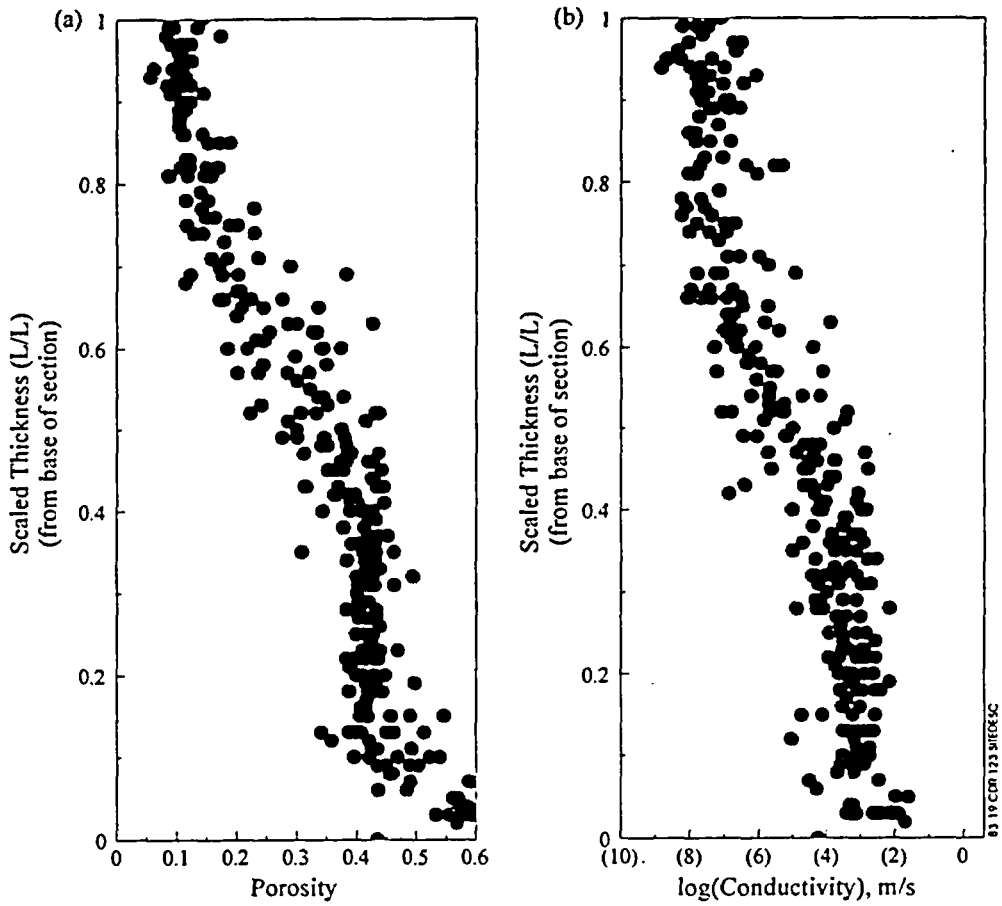

Source: Modified from Rautman, C.A. (1995, Figure 6)

Figure 8.3-19. Porosity and Log of Saturated Hydraulic Conductivity of All Samples from 26 Vertical Transects of the Base of the Tiva Canyon Tuff

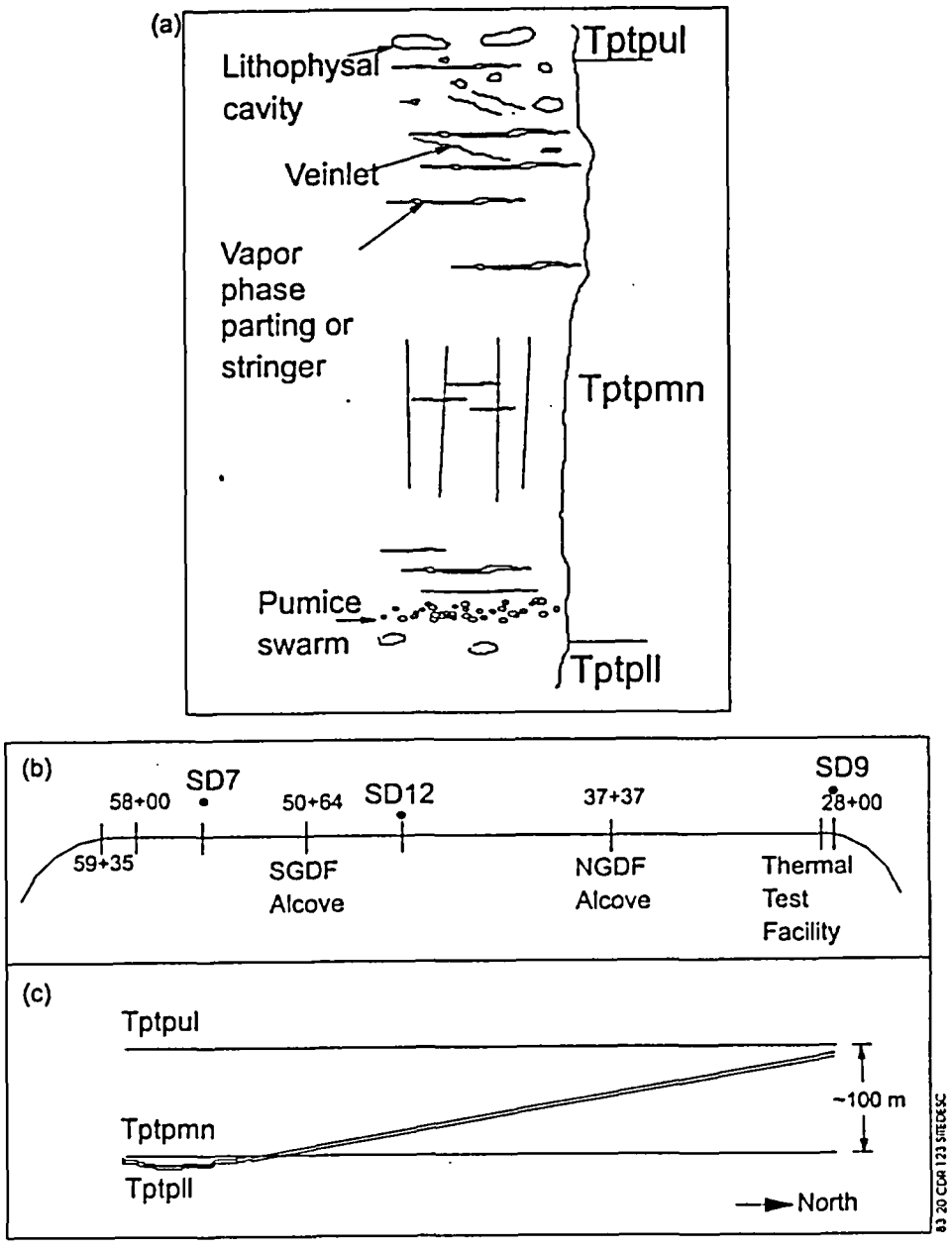

NOTES: (a) a vertical section of unit Tptpmn, (b) a plan view of the Exploratory Studies Facility where Tptpmn samples were taken, (c) a cross section showing route of Exploratory Studies Facility Main Drift and its Relationship to the Tptpmn unit.
SGDF = South Ghost Dance fault; NGDF = North Ghost Dance fault

Figure 8.3-20. Schematic Diagram of the Tptpmn Unit and Its Location in Relation to the Exploratory Studies Facility Main Drift

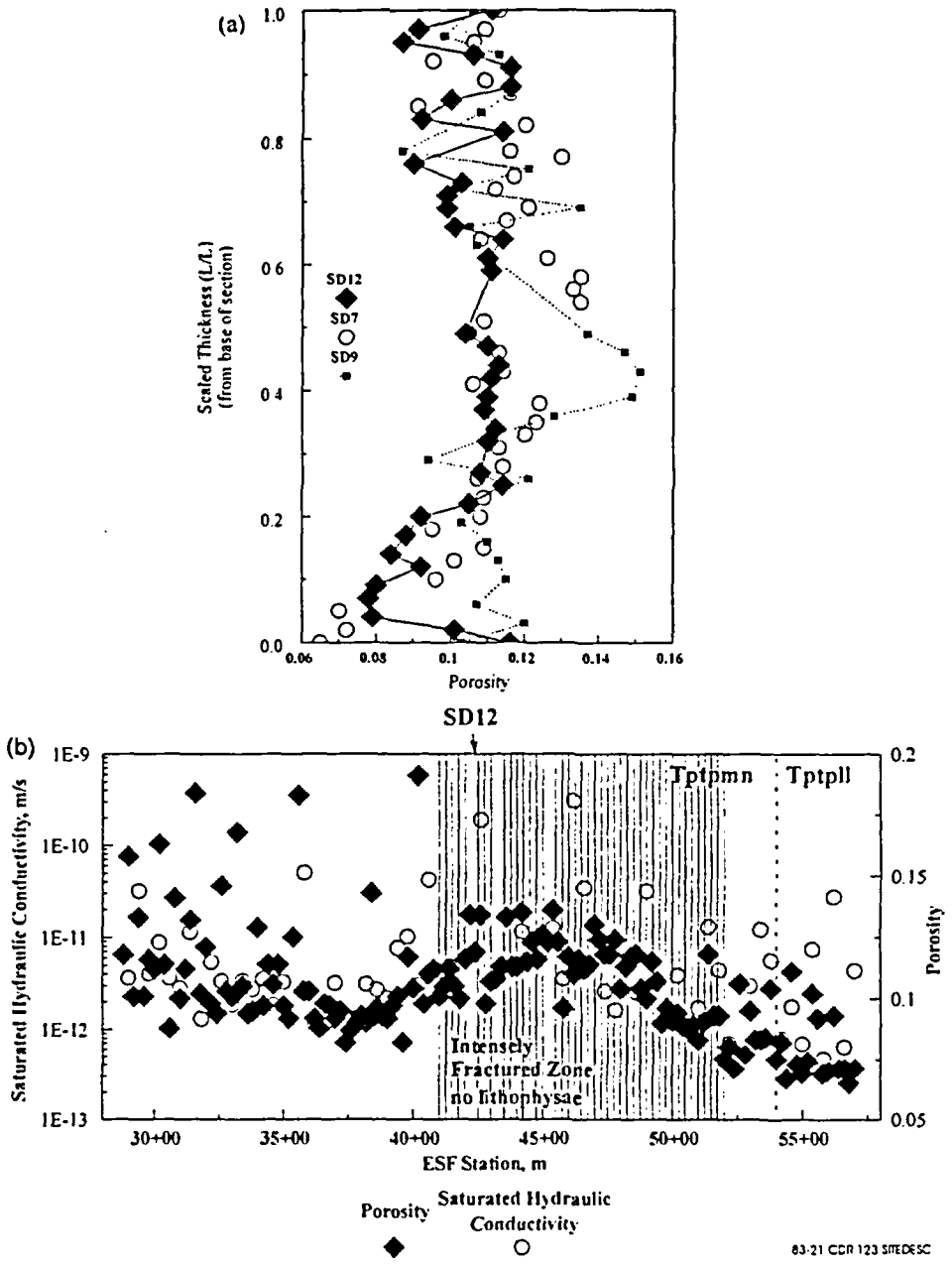

DTNs: GS960908312231.004, GS970108312231.002, GS970708312231.004, GS971008312231.006

NOTE: (a) porosity calculated from relative humidity drying of samples of the Tptpmn from three surface-based boreholes; (b) porosity and saturated hydraulic conductivity measured along the systematic-sampling transect in the Exploratory Studies Facility Main Drift

Figure 8.3-21. Porosity Profile for Tptpmn in Three Surface-Based Boreholes and Profile of Porosity and Saturated Hydraulic Conductivity for Many Samples in the Exploratory Studies Facility Main Drift

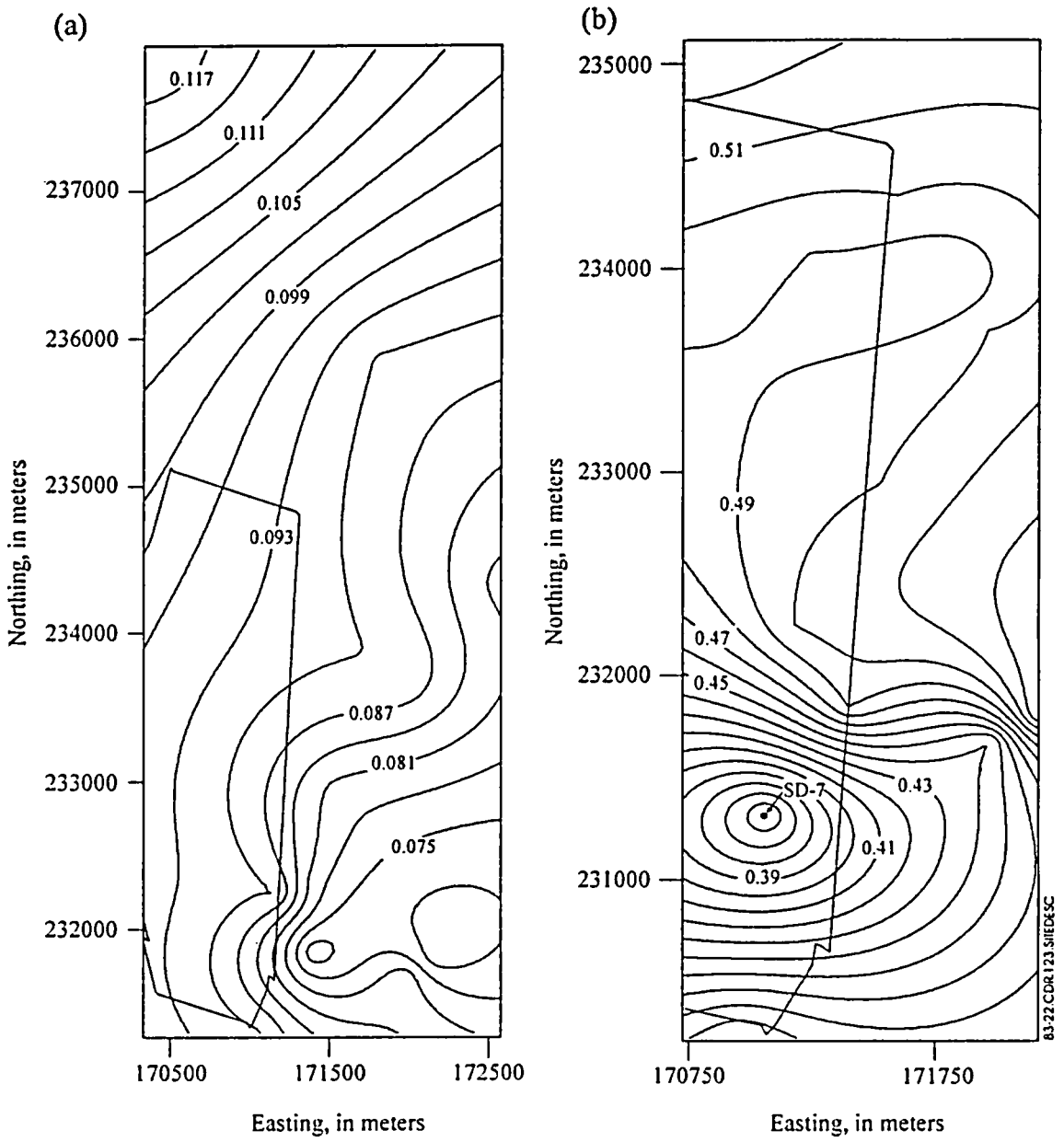

Source: Flint, L.E. (1998, Figure 16)

NOTES: Plot (a) for the CW unit was developed from data from 17 boreholes; plot (b) for the BT2 unit, from 15 boreholes. These two units are defined in Table 8.3-1.
Outline of potential repository location is indicated.

Figure 8.3-22. Contour Plots of the Spatial Distribution of Porosity for Hydrogeologic Units CW and BT2

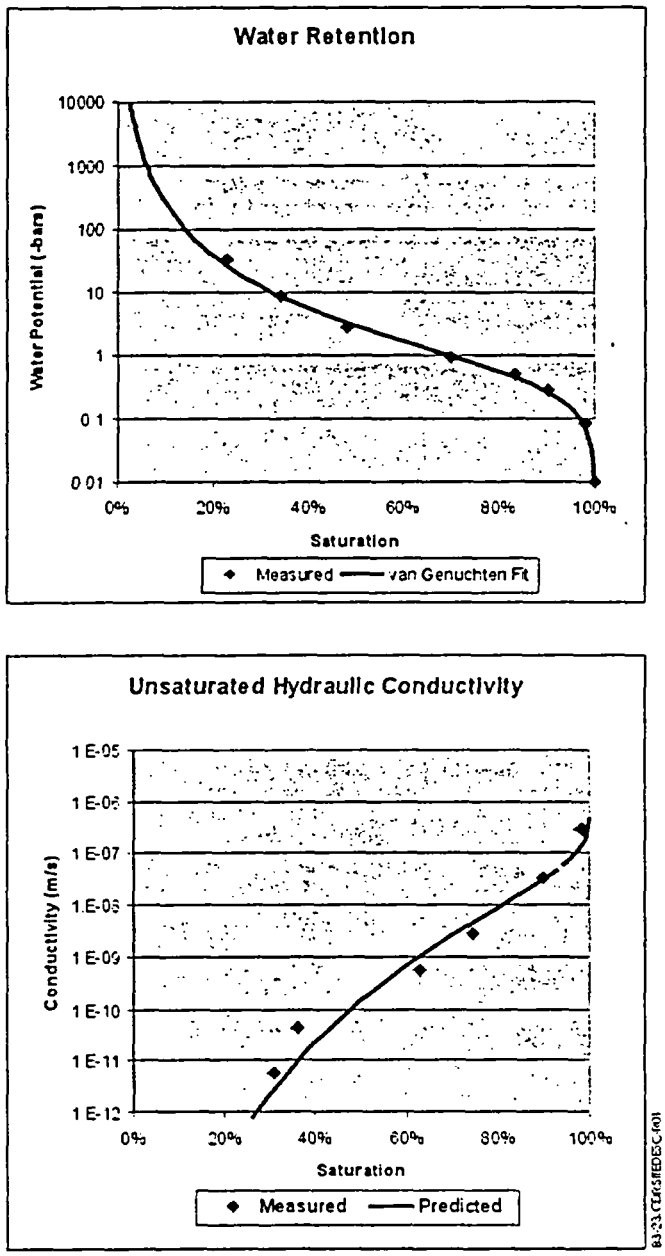

DTNs: GS990308312242.007, GS990708312242.008

Figure 8.3-23. Measured and Model-Predicted Moisture Retention and Unsaturated Hydraulic Conductivity for a Sample of the Vitric Calico Hills Formation (Tac Unit 4) from the Busted Butte Test Facility (Measurements Made Using a Steady-State Centrifuge)

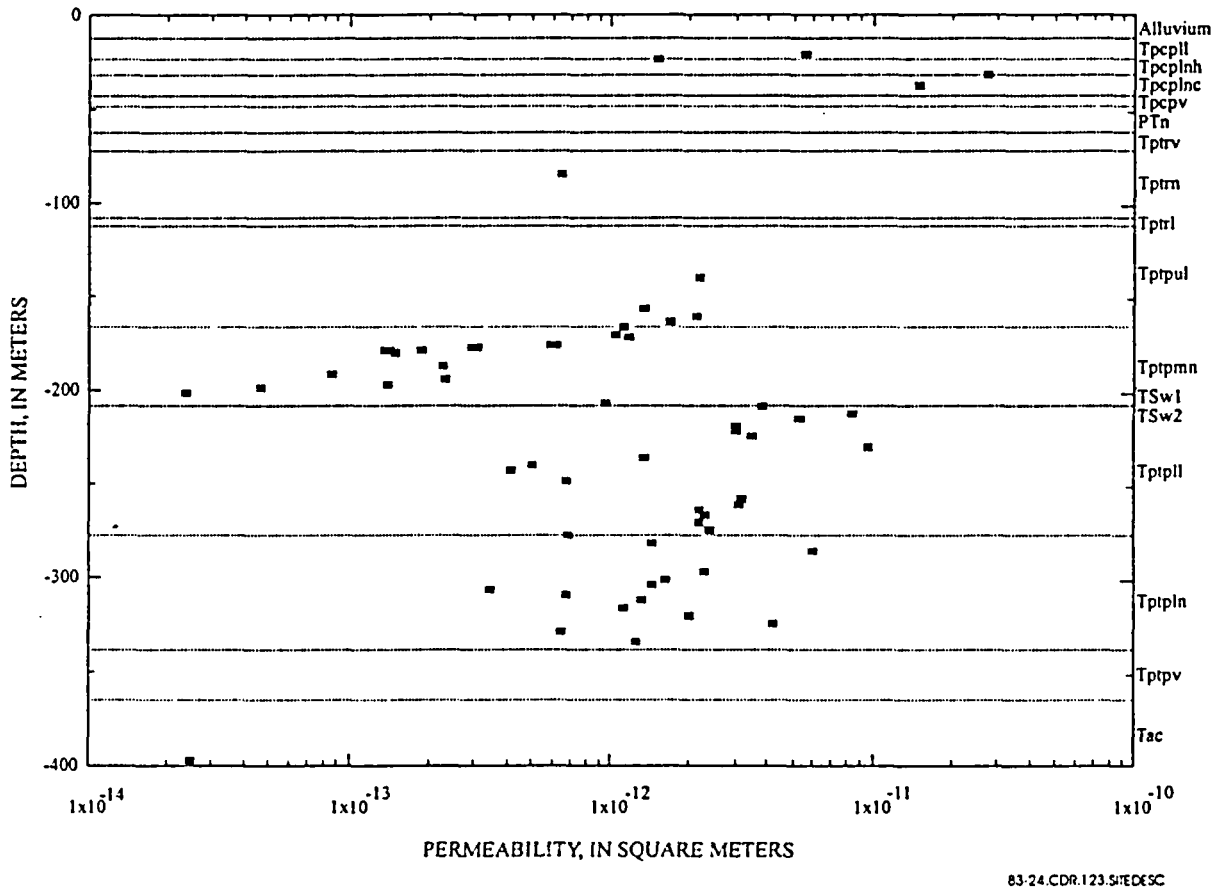

Source: LeCain, G.D. (1997, Figure 7)

Figure 8.3-24. Relation of Air-Injection Permeability Values to Depth and Lithostratigraphic Units Penetrated in Borehole UZ-16

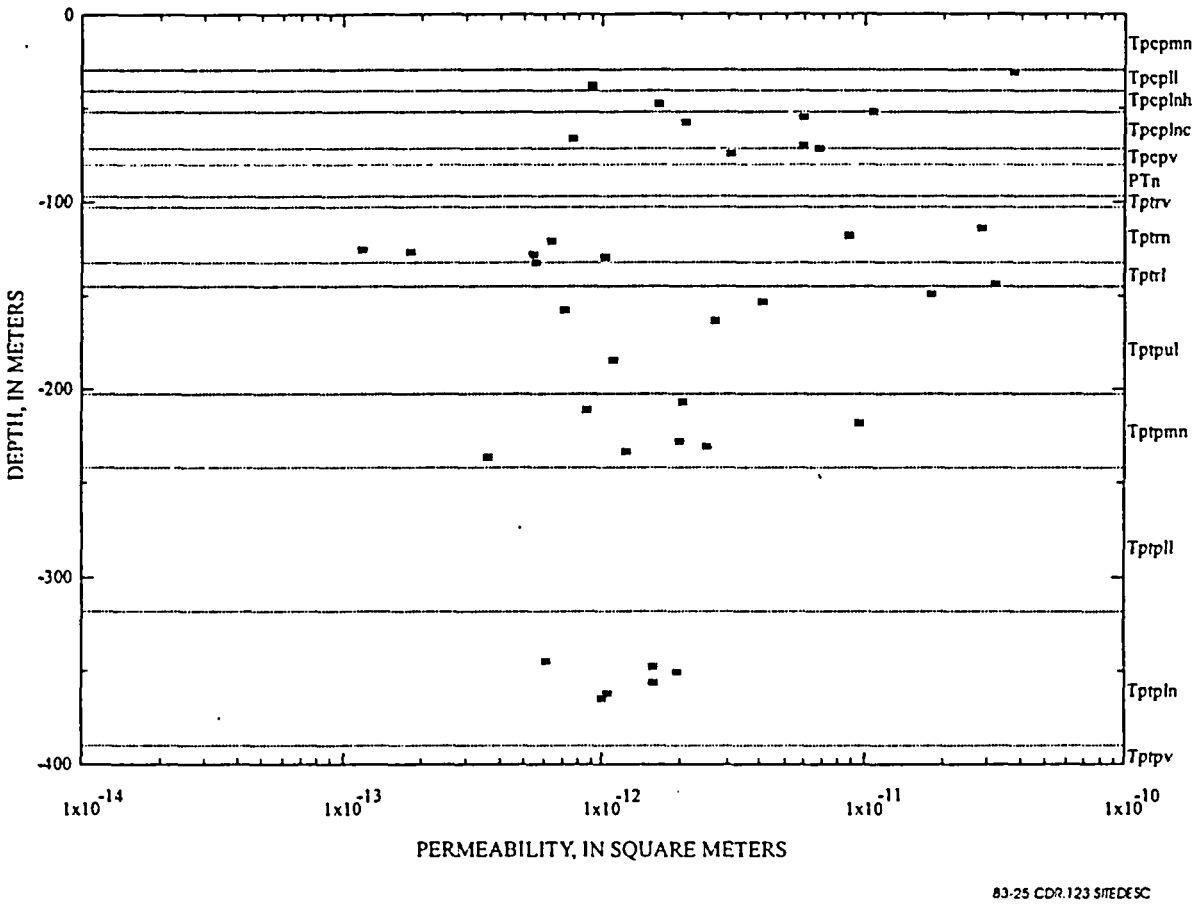

Source: LeCain, G.D. (1997, Figure 8)

Figure 8.3-25. Relation of Air-Injection Permeability Values to Depth and Lithostratigraphic Units Penetrated in Borehole SD-12

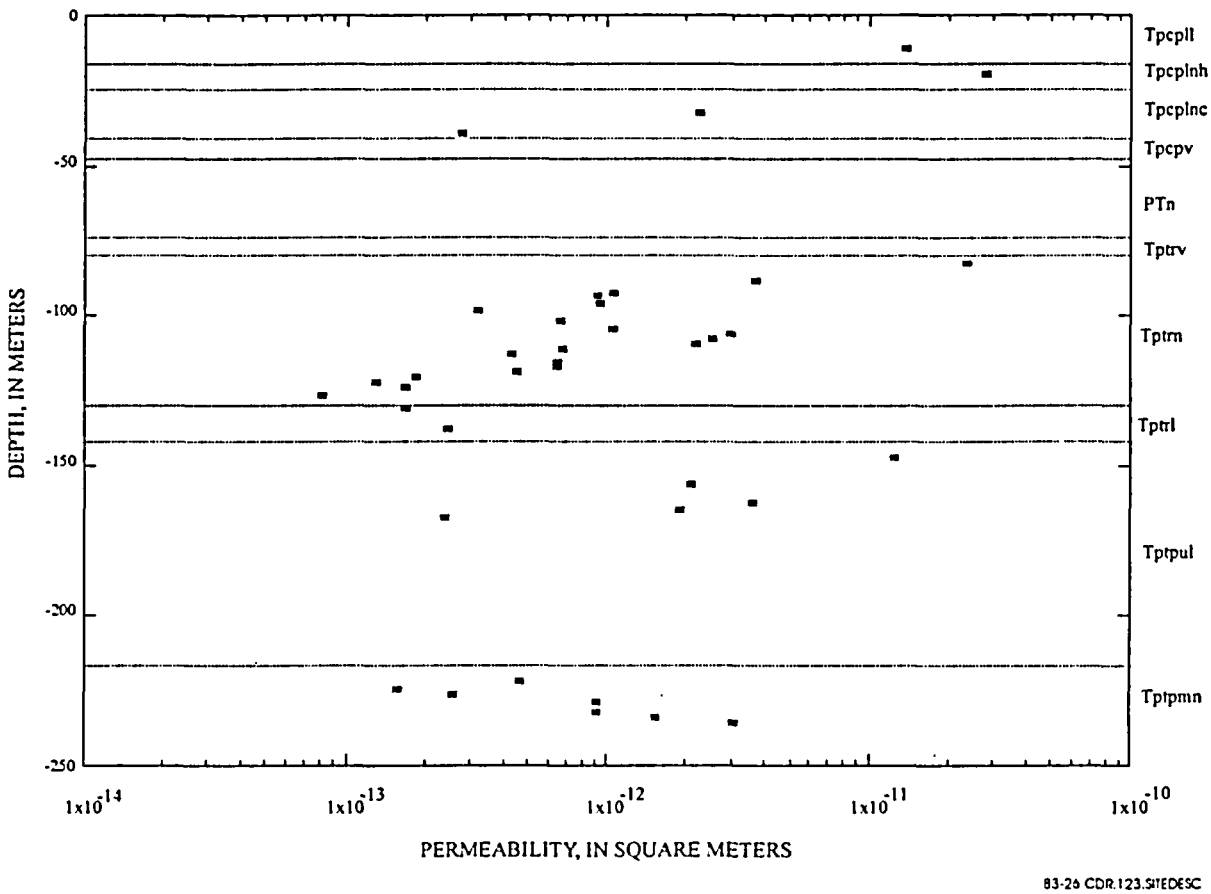

Source: LeCain, G.D. (1997, Figure 9)

Figure 8.3-26. Relation of Air-Injection Permeability Values to Depth and Lithostratigraphic Units Penetrated in Borehole NRG-6

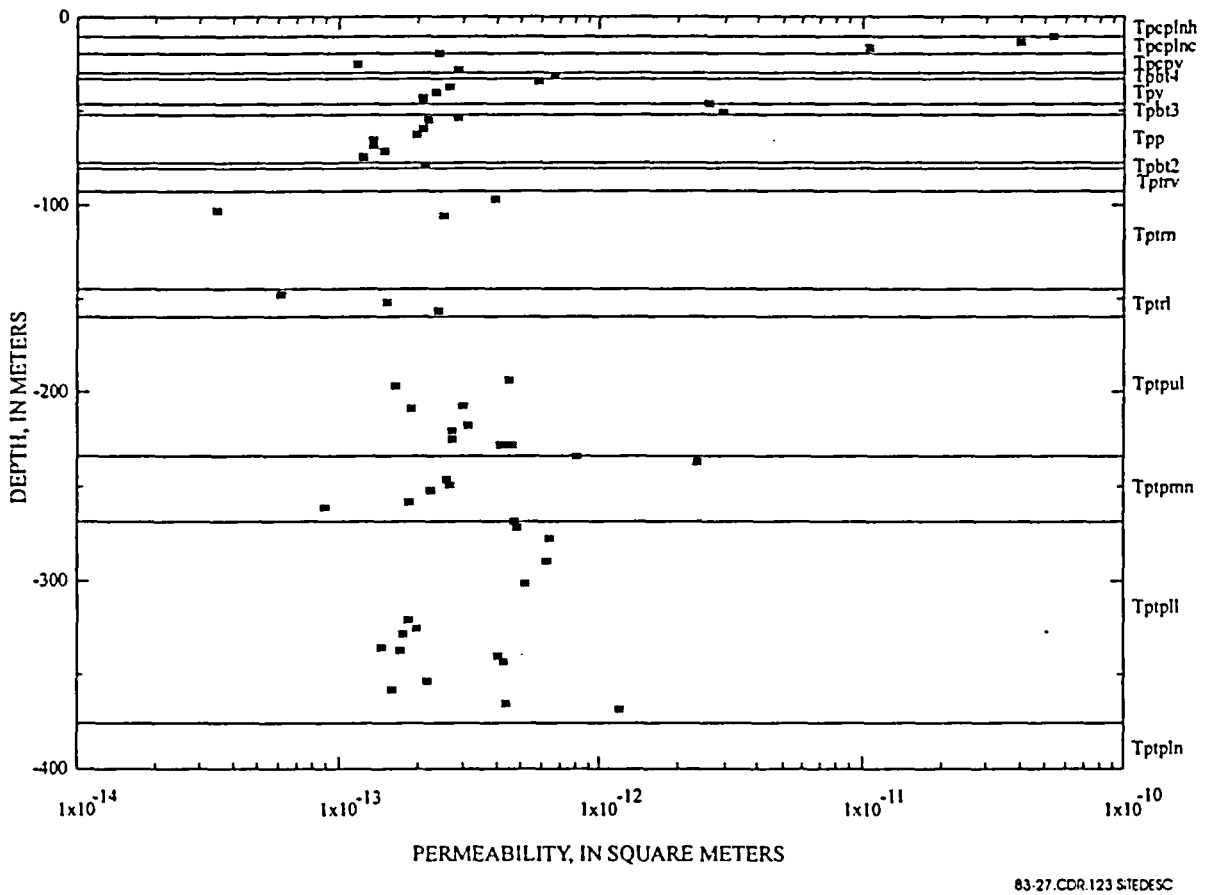

Source: LeCain, G.D. (1997, Figure 10)

Figure 8.3-27. Relation of Air-Injection Permeability Values to Depth and Lithostratigraphic Units Penetrated in Borehole NRG-7a

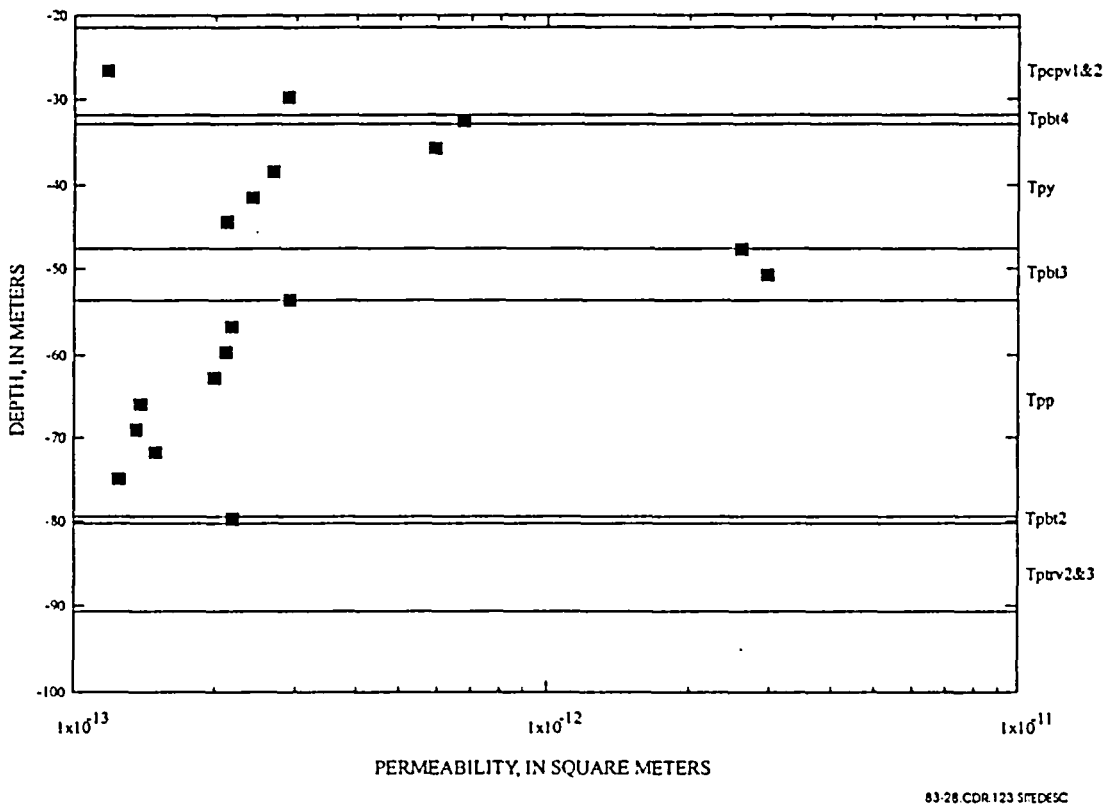

Source: LeCain, G.D. (1997, Figure 14)

Figure 8.3-28. Air-Injection Permeability Values in the Paintbrush Nonwelded Hydrogeologic Unit with Depth in Borehole NRG-7a

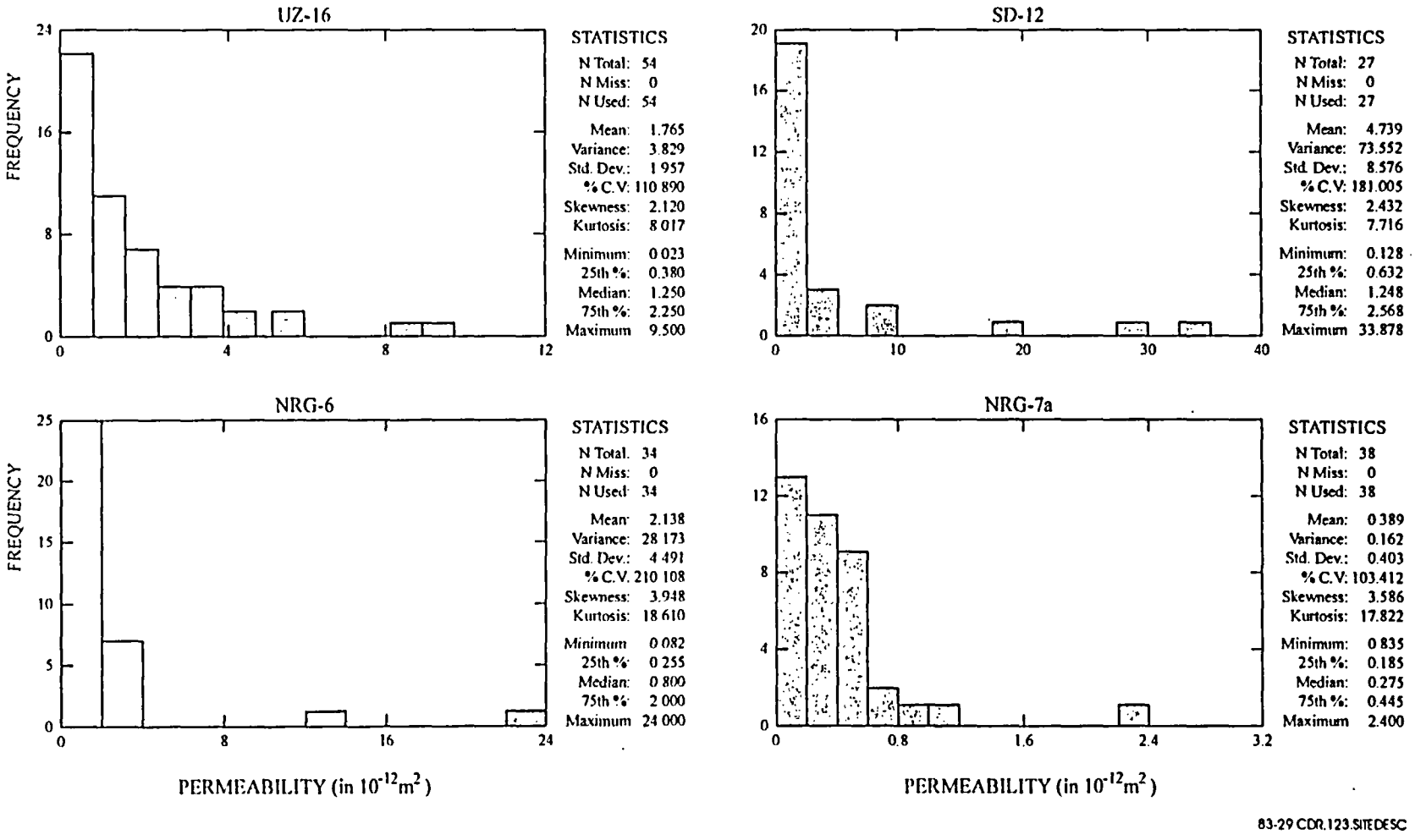

Source: LeCain, G.D. (1997, Figure 17)

Figure 8.3-29. Histograms of Air-Injection Permeability Values and Basic Statistics by Borehole for the Topopah Spring Tuff

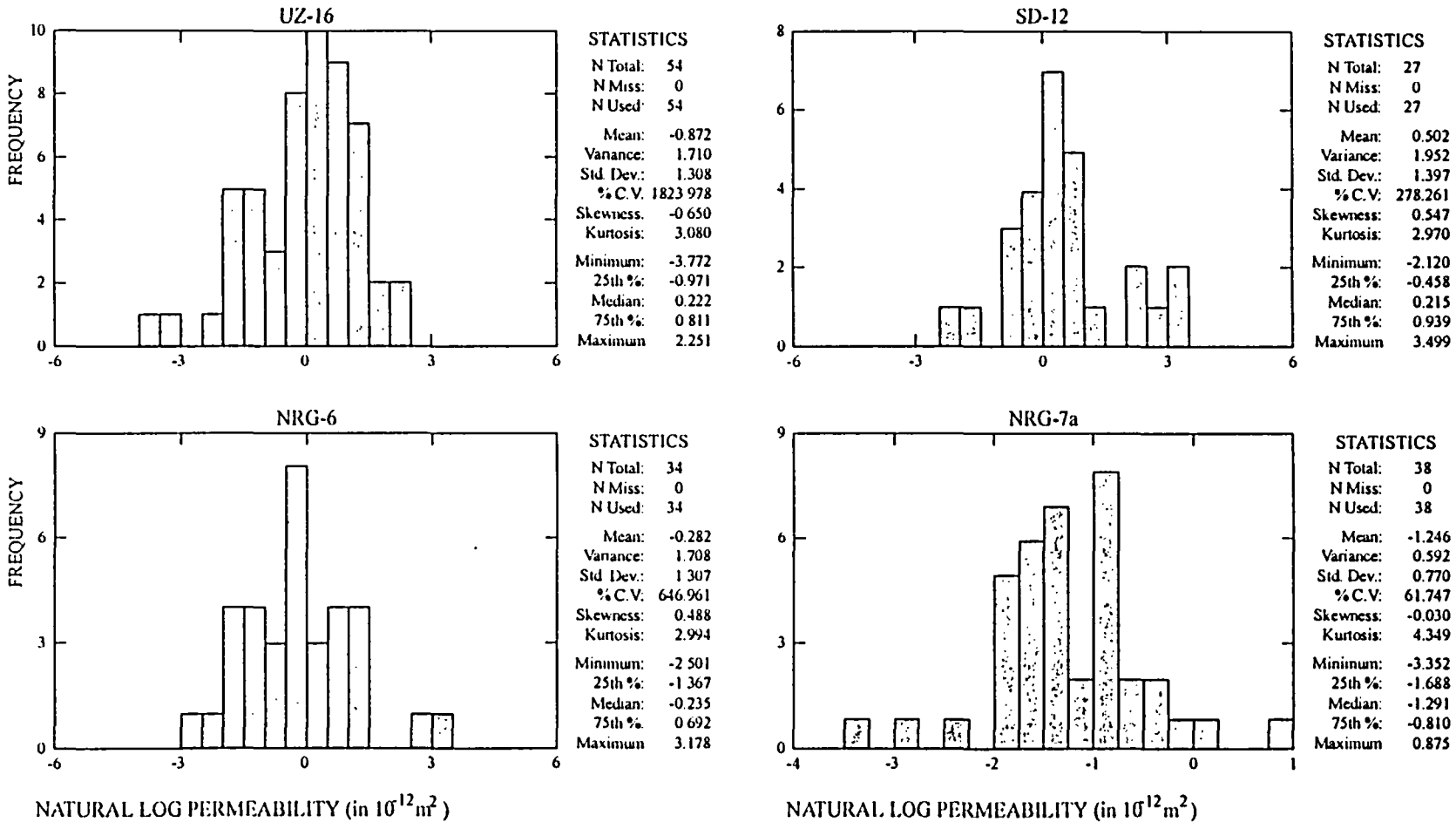

Source: LeCain, G.D. (1997, Figure 18)

Figure 8.3-30. Histograms of Natural Log Air-Injection Permeability Values and Basic Statistics by Borehole for the Topopah Spring Tuff

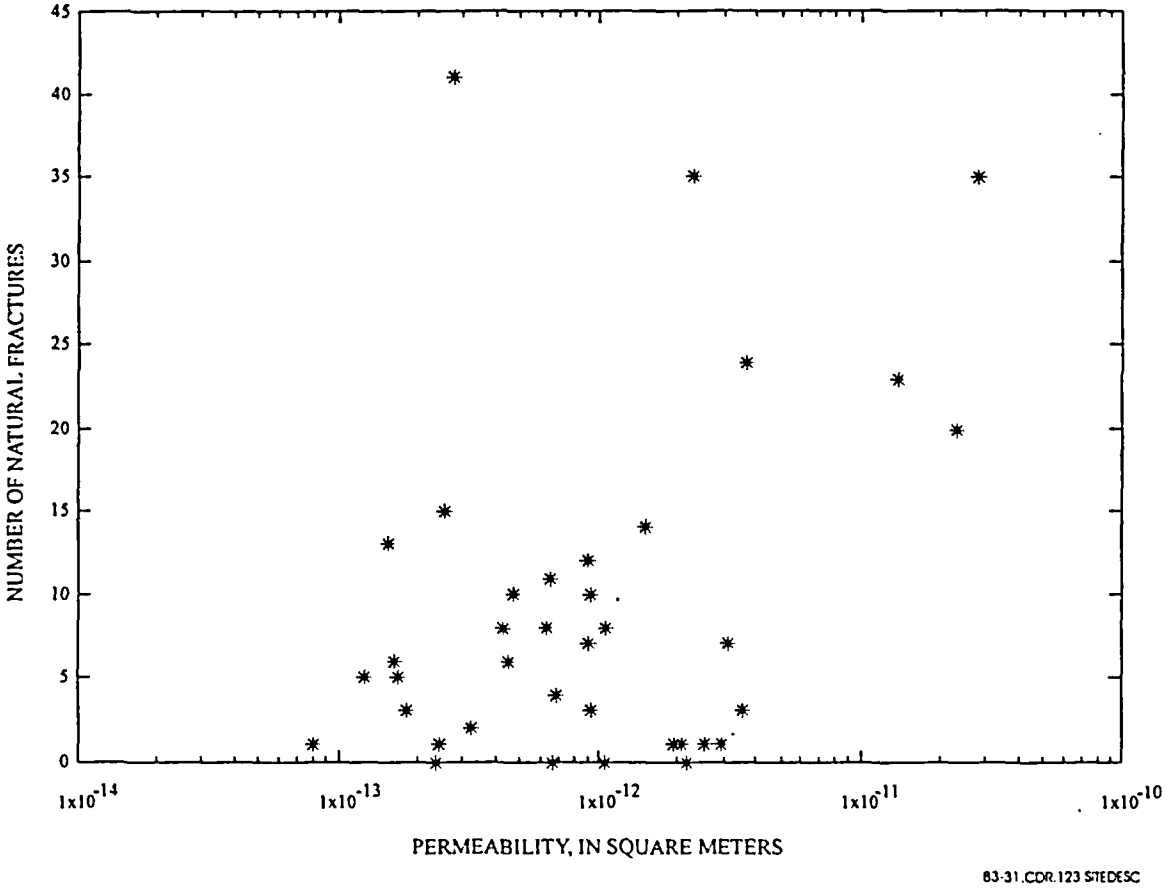

Source: LeCain, G.D. (1997, Figure 20)

Figure 8.3-31. Relation between Air-Injection Permeability Values and Number of Natural Fractures per Test Interval, Borehole NRG-6

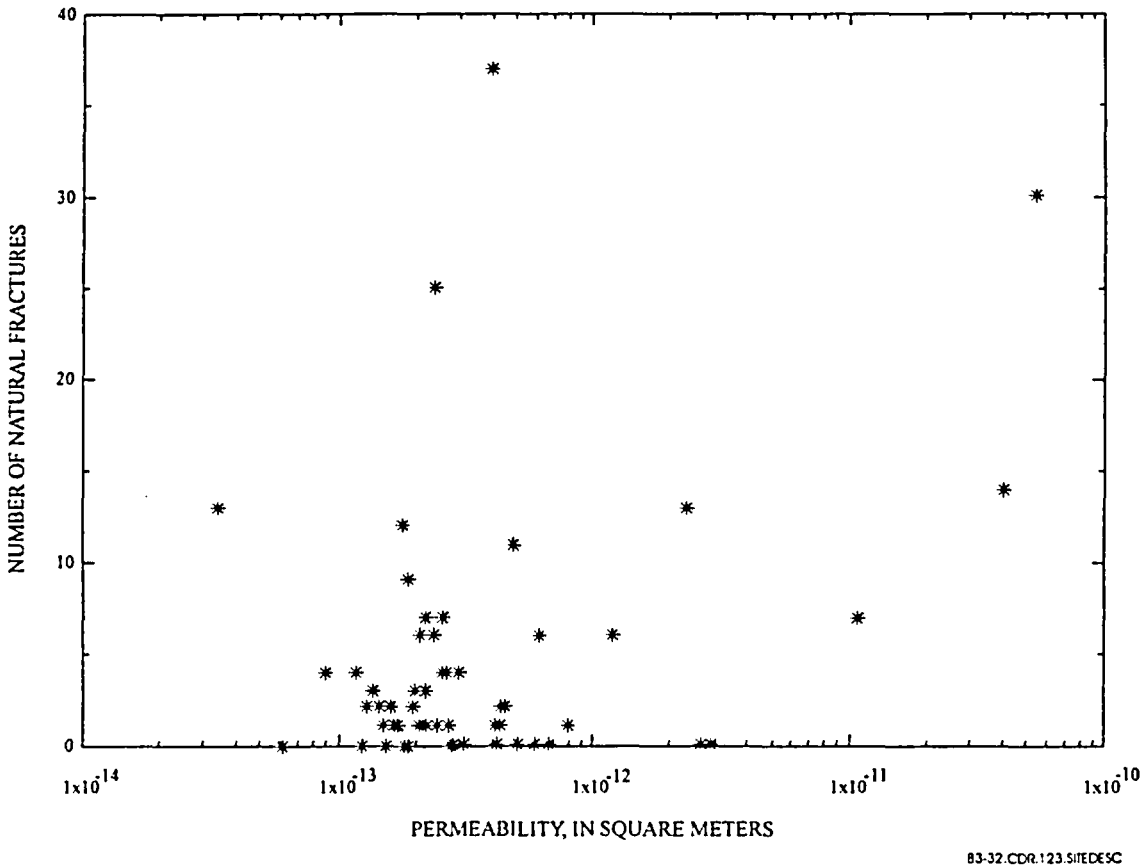

Source: LeCain, G.D. (1997, Figure 21)

Figure 8.3-32. Relation between Air-Injection Permeability Values and Number of Natural Fractures per Test Interval, Borehole NRG-7a

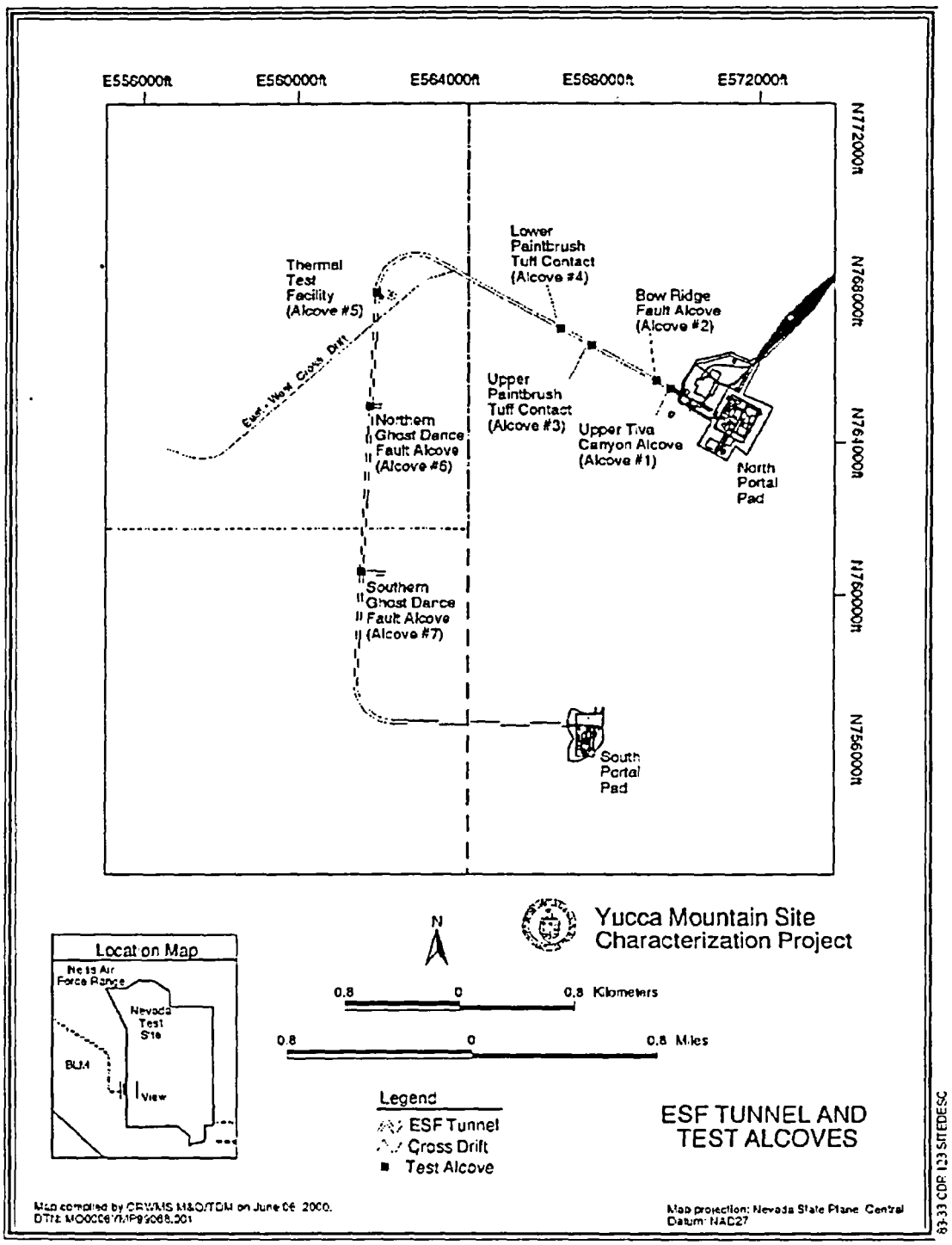

Figure 8.3-33. Map of Exploratory Studies Facility Showing Locations of Test Alcoves

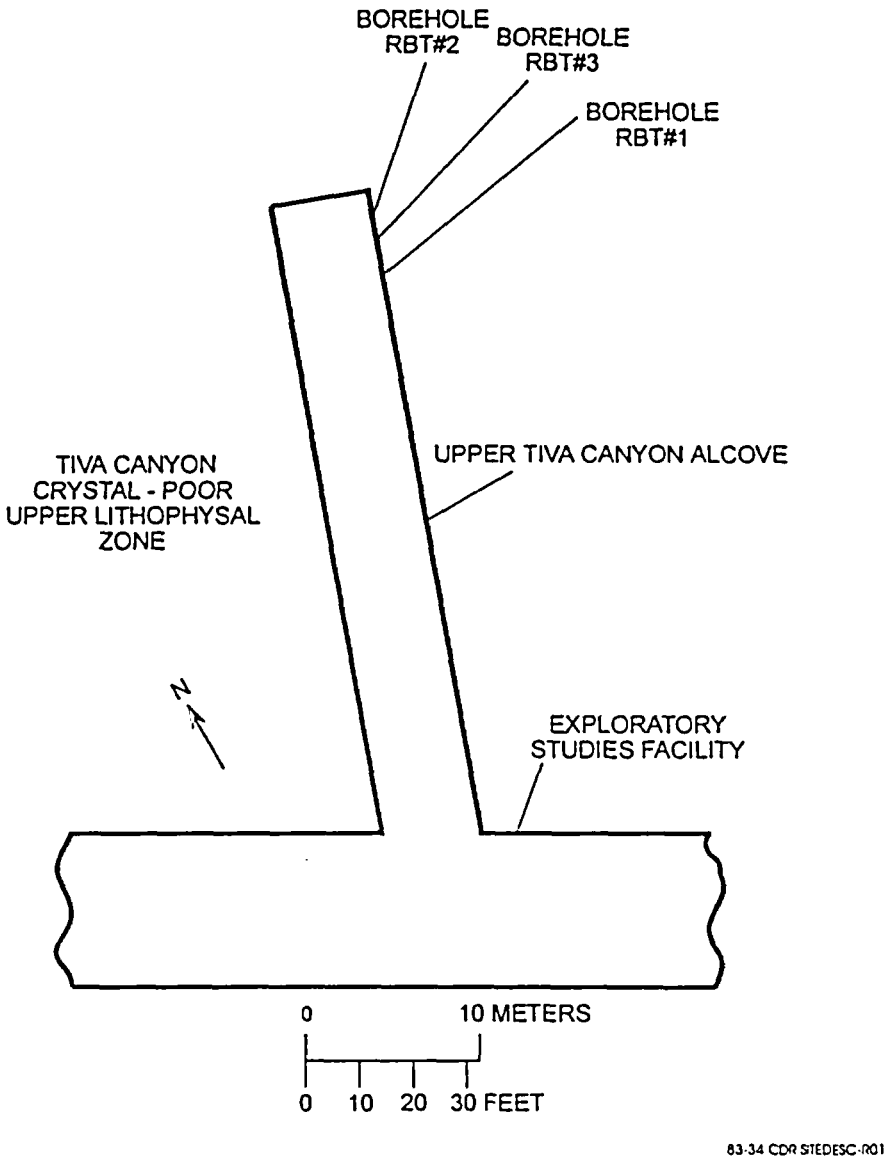

Source: LeCain, G.D. (1998, Figure 9)

Figure 8.3-34. Plan View Schematic Diagram of the Upper Tiva Canyon Alcove and Location of Boreholes RBT#1, RBT#2, and RBT#3

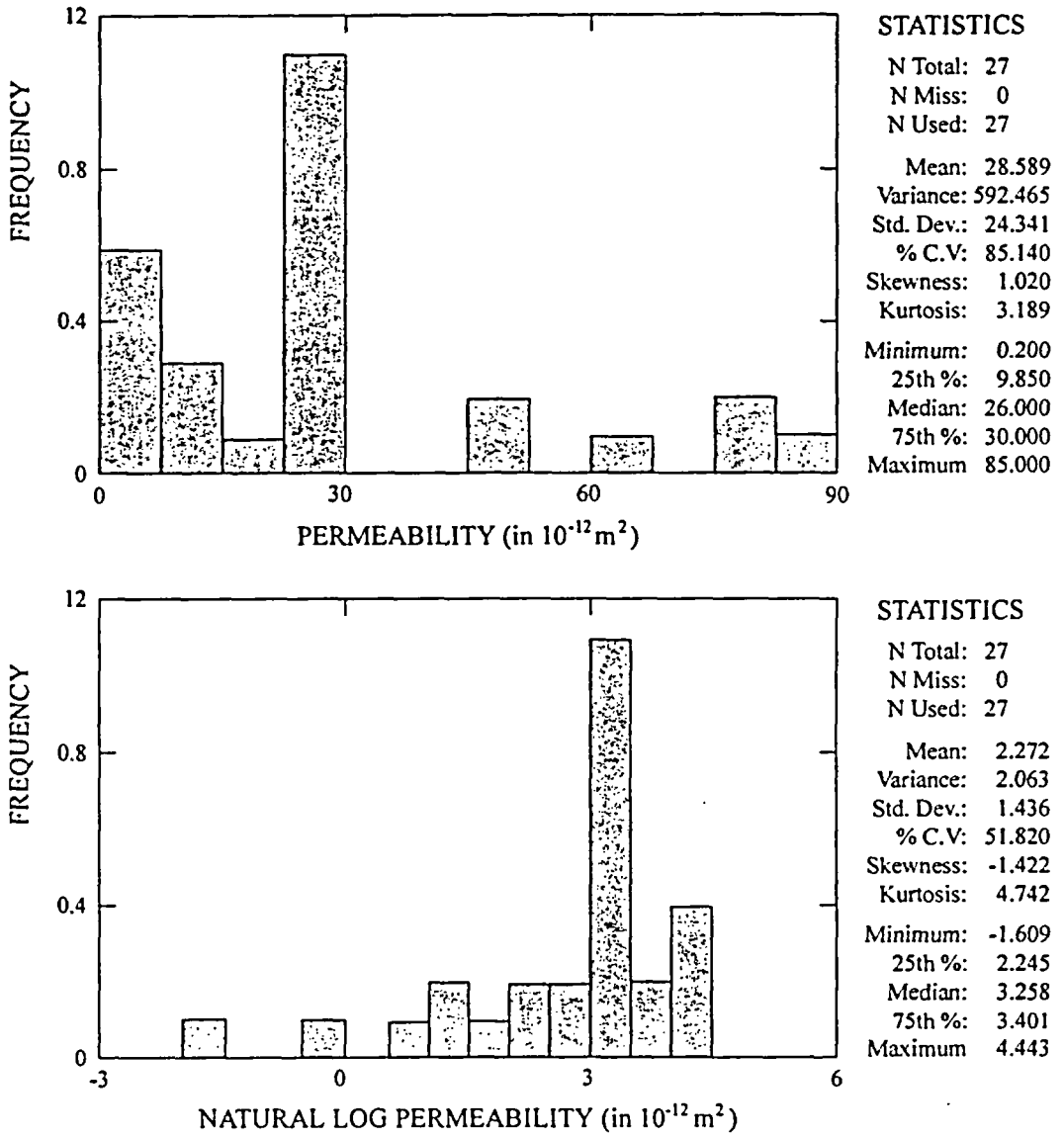

Source: LeCain, G.D. (1998, Figure 10)

Figure 8.3-35. Composite Histograms and Statistics for Air-Permeability Values from the Upper Tiva Canyon Alcove Radial Boreholes RBT#1, RBT#2, and RBT#3

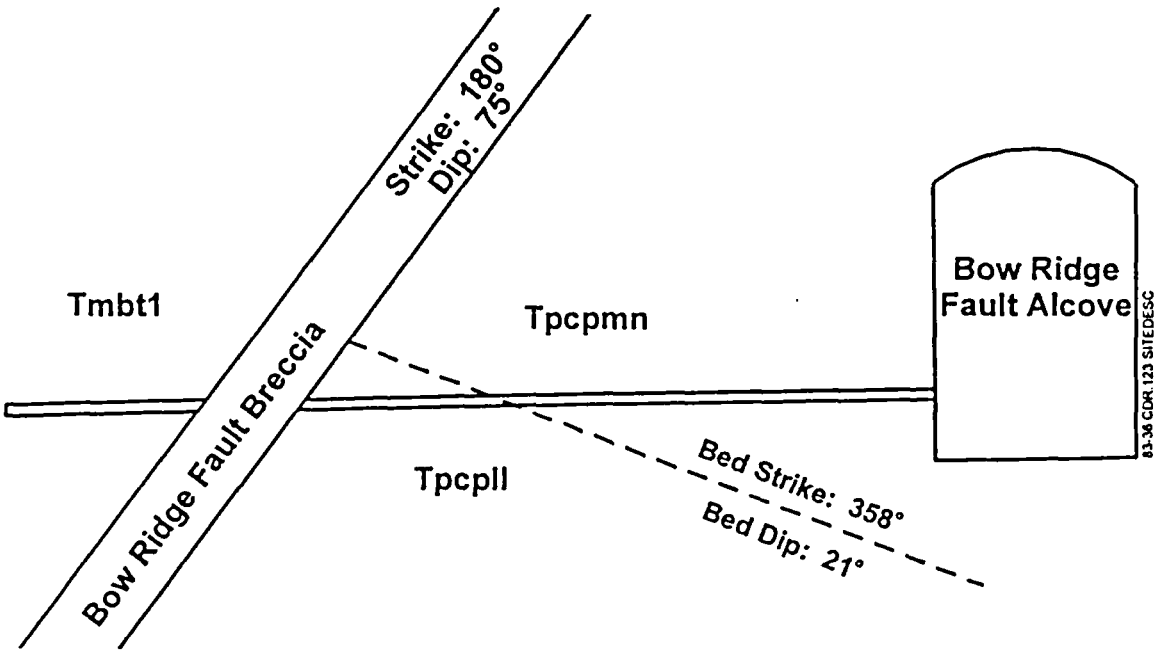

Source: Modified from LeCain, G.D. (1998, Figure 12)

Figure 8.3-36. Cross Section of the Bow Ridge Fault, the Bow Ridge Fault Alcove, and Borehole HPF#1

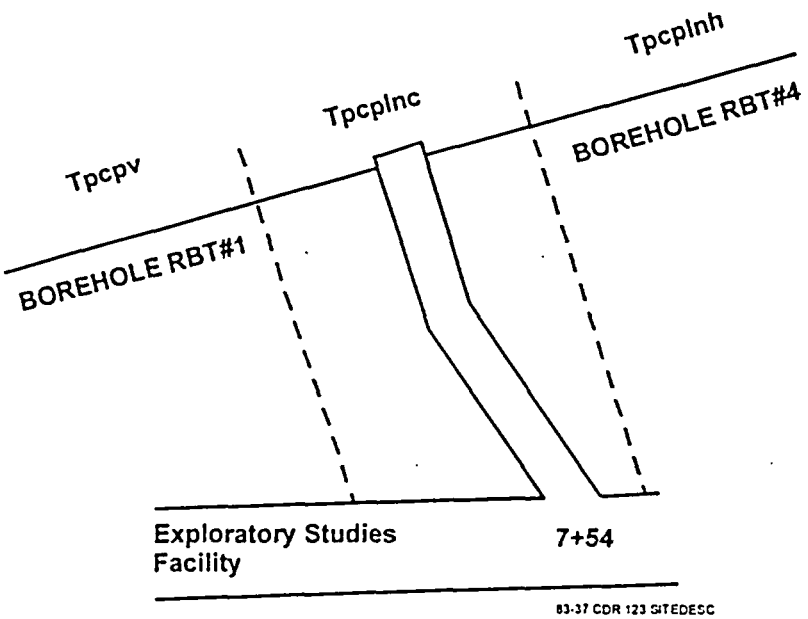

Source: Modified from LeCain, G.D. (1998, Figure 13)

Figure 8.3-37. Plan View Schematic Diagram of the Upper Paintbrush Contact Alcove and Boreholes RBT#1 and RBT#4

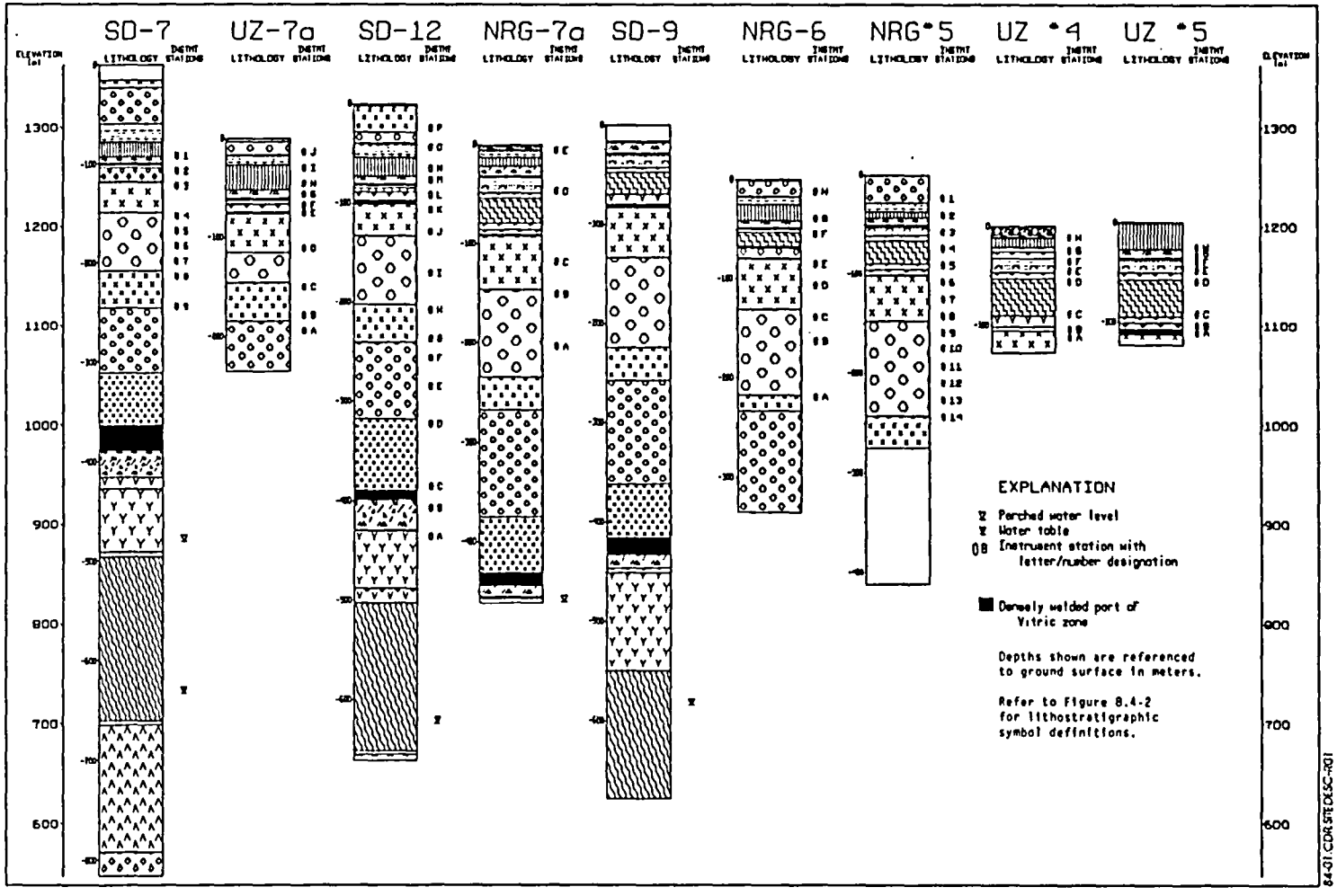

Sources: Rousseau et al. (1999, Figure 41); Rousseau et al. (1997, Figure 3.0-1); Patterson et al. (1996, Figure 4)

Figure 8.4-1. Location of Instrument Stations and Lithostratigraphy for Instrumented Boreholes

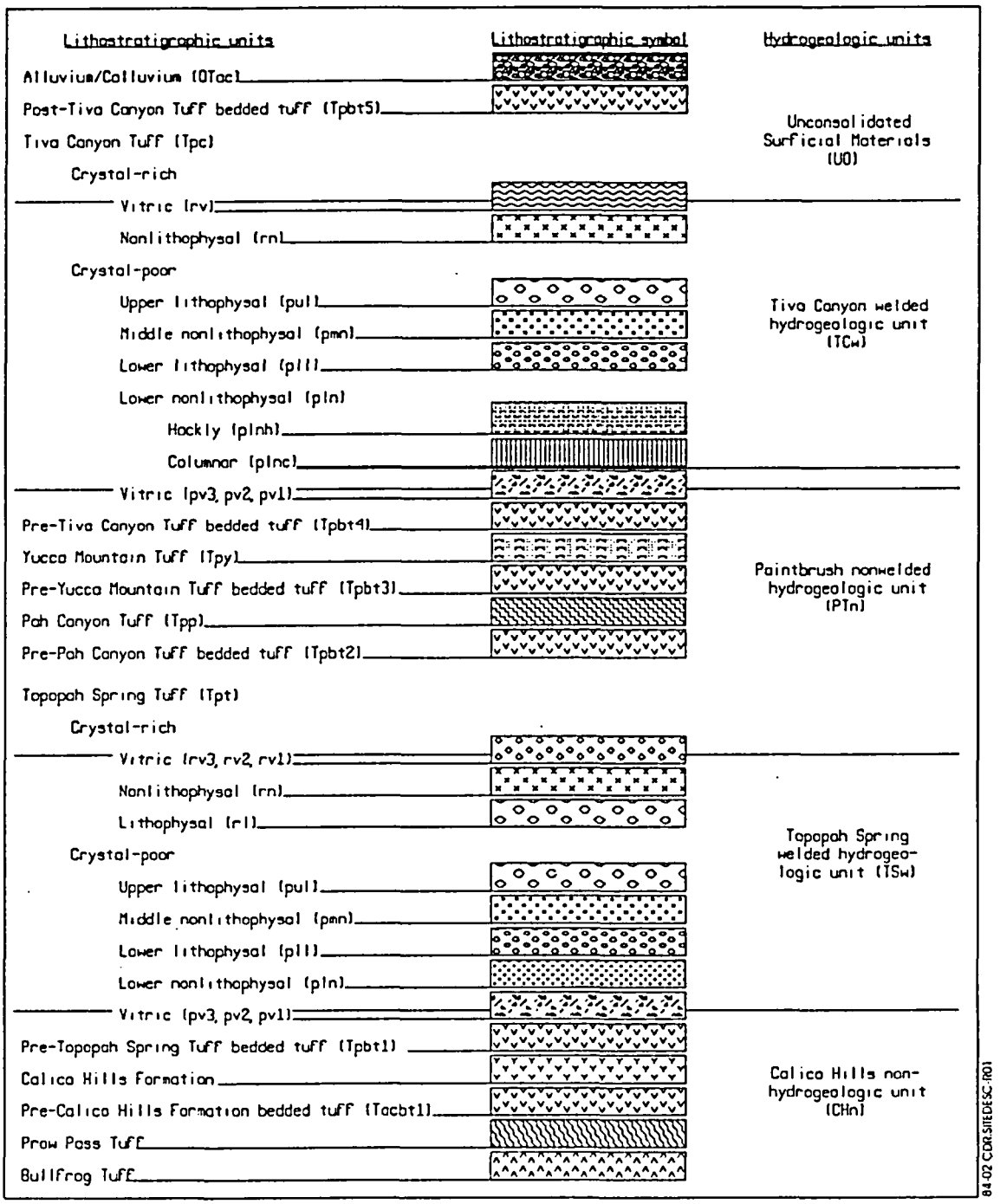

Source: Rousseau et al. (1999, Figure 23)

Figure 8.4-2. Lithostratigraphic and Hydrogeologic Units in the Yucca Mountain Area

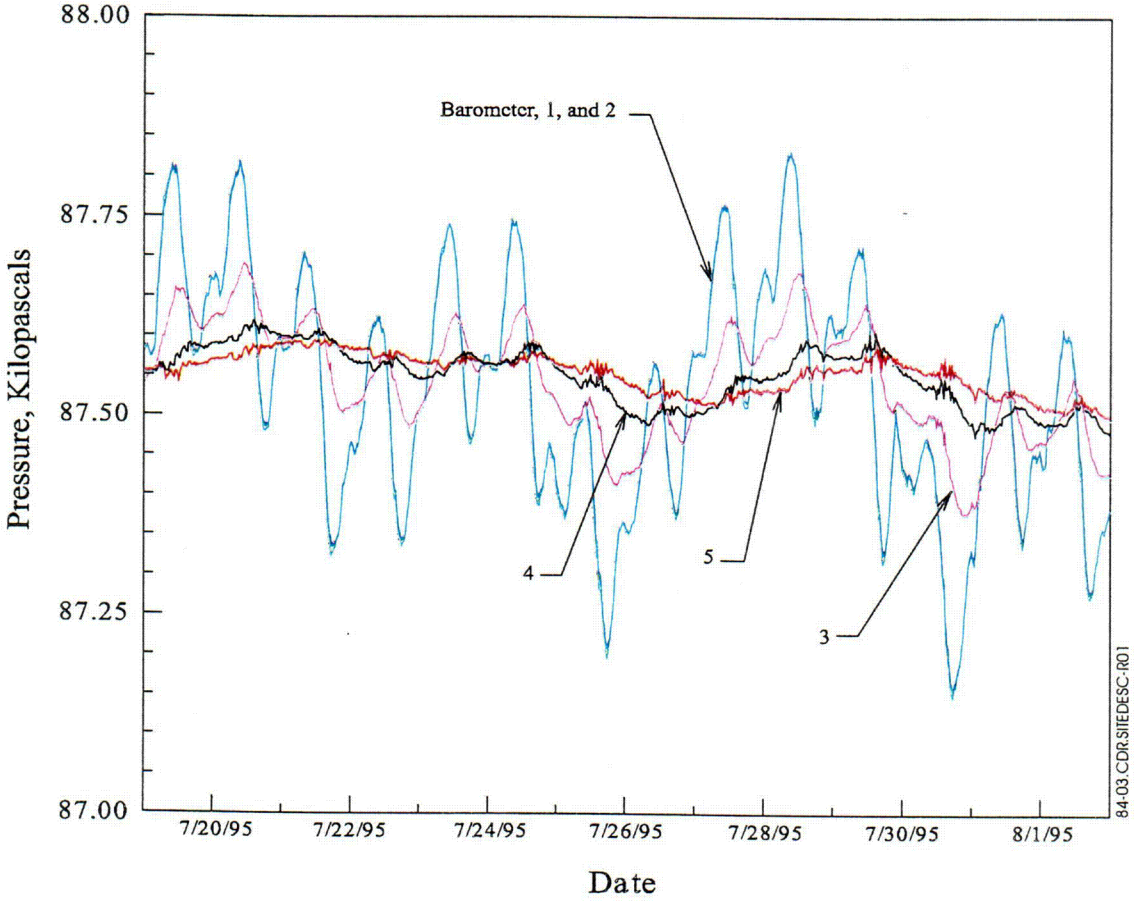

Instrument Station	Depth (meters)	Lithology	Residual Amplitude (percent)	Phase Lag (hours)
1	23.2	Tiva Canyon Upper Lithophysal	99	0.3
2	40.5	Tiva Canyon Columnar	99	0.3
3	57.0	Yucca Mountain Tuff	61	12.2
4	74.1	Pah Canyon Tuff	38	31.6
5	90.8	Pre-Pah Canyon Tuff bedded tuff	31	46.8

Source: Patterson et al. (1996, Figure 5a)

Figure 8.4-3. Pneumatic Pressure Record and Results of Cross-Spectral Analysis for Instrument Stations 1 through 5 in Borehole NRG#5 Prior to the Exploratory Studies Facility Excavation

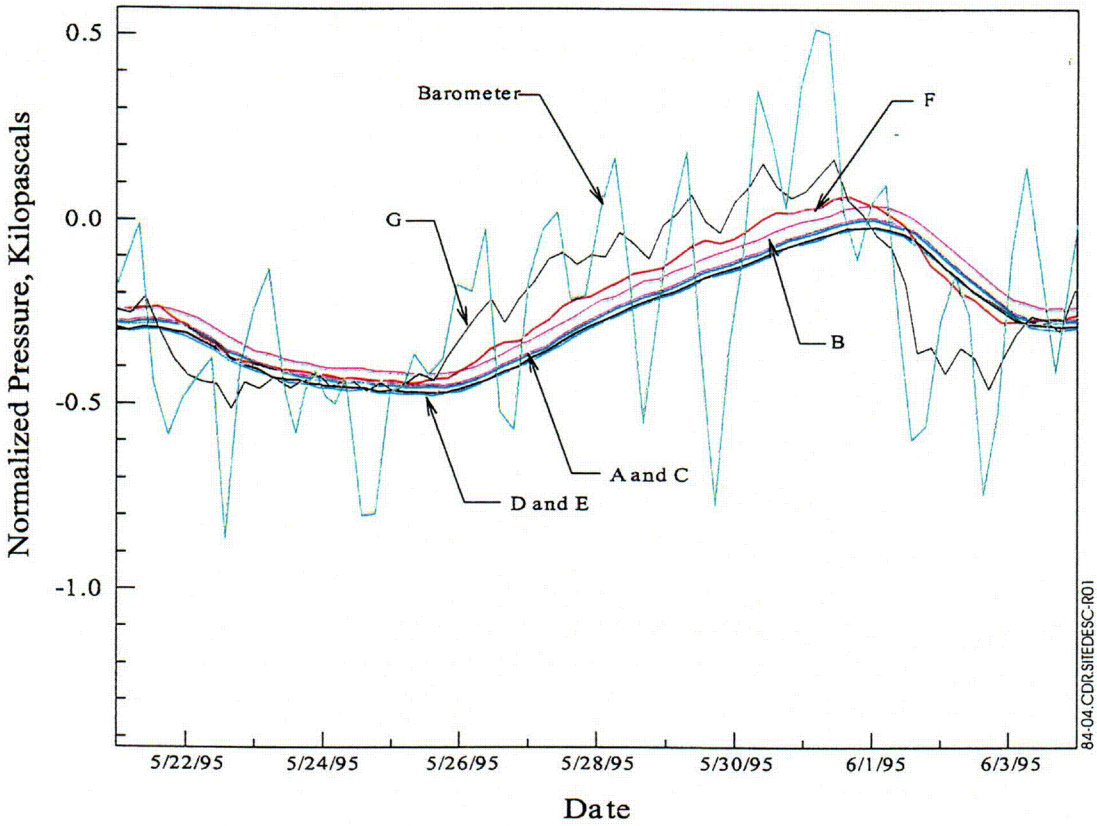

Instrument Station	Depth (meters)	Lithology	Residual Amplitude (percent)	Phase Lag (hours)
G	39.6	Tiva Canyon Columnar	56	1.8
F	54.9	Pah Canyon Tuff	36	31.5
E	85.3	Topopah Spring Crystal-Rich Nonlithophysal	29	42.7
D	106.8	Topopah Spring Crystal-Rich Nonlithophysal	29	42.3
C	138.8	Topopah Spring Upper Lithophysal	30	42.8
B	163.1	Topopah Spring Upper Lithophysal	30	43.1
A	219.4	Topopah Spring Middle Nonlithophysal	30	43.5

Source: Patterson et al. (1996, Figure 6)

Figure 8.4-4. Pneumatic Pressure Record and Results of Cross-Spectral Analysis for Borehole NRG-6 Prior to the Exploratory Studies Facility Excavation

C048

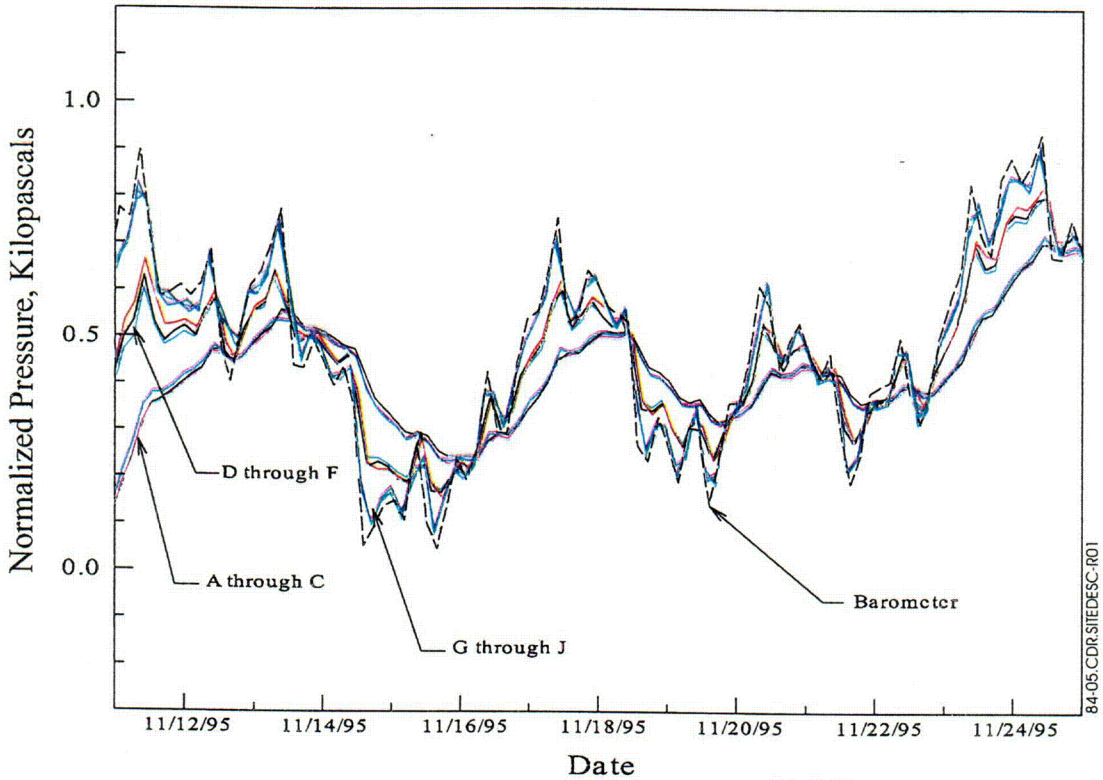

Instrument Station	Depth (meters)	Lithology	Residual Amplitude (percent)	Phase Lag (hours)
J	13.5	Tiva Canyon Lower Lithophysal	100	0.5
I	29.9	Tiva Canyon Columnar	96	0.9
H	45.6	Tiva Canyon Columnar	96	0.9
G	56.3	Tiva Canyon Crystal-Poor Vitric	97	2.5
F	67.1	Pre-Pah Canyon Tuff bedded tuff	79	5.3
E	75.1	Topopah Spring Crystal-Rich Vitric	75	5.2
D	111.0	Topopah Spring Crystal-Rich Nonlithophysal	73	6.0
C	149.8	Topopah Spring Upper Lithophysal	57	14.5
B	178.3	Topopah Spring Middle Nonlithophysal	54	15.1
A	194.0	Topopah Spring Lower Lithophysal	56	16.0

Source: Patterson et al. (1996, Figure 11)

Figure 8.4-5. Pneumatic Pressure Record and the Results of Cross-Spectral Analysis for Borehole UZ-7a Prior to the Exploratory Studies Facility Excavation

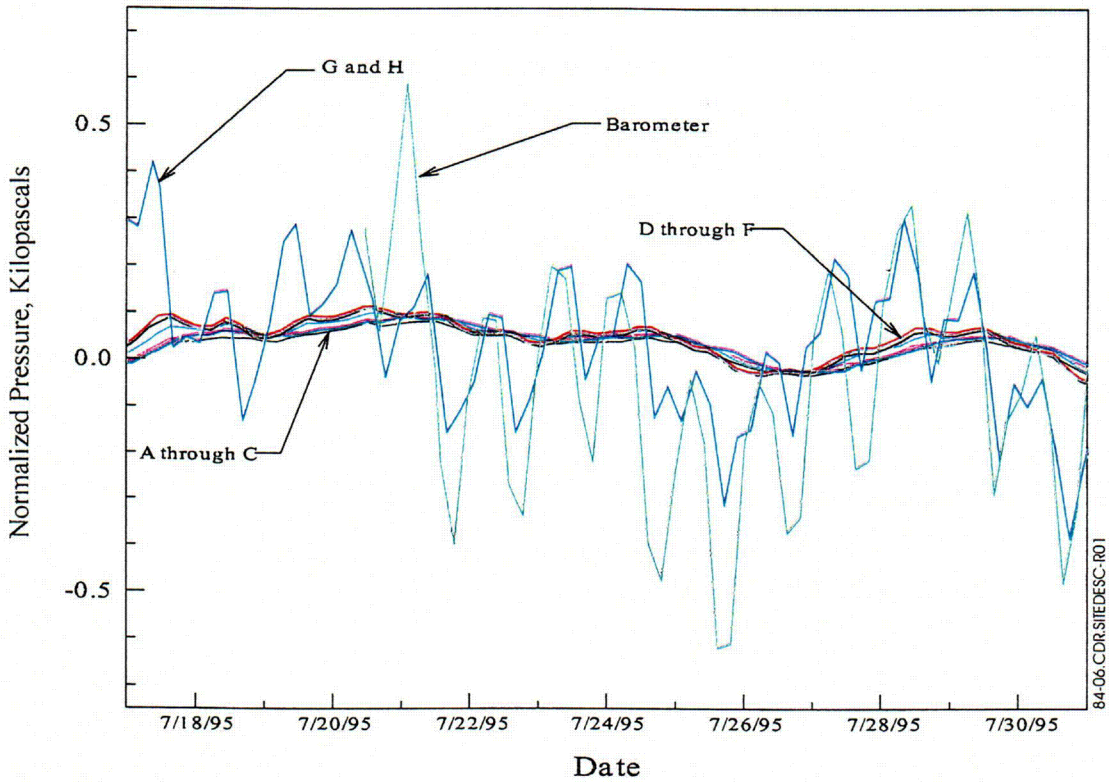

Instrument Station	Depth (meters)	Lithology	Residual Amplitude (percent)	Phase Lag (hours)
H	11.1	Alluvium/Colluvium	N/A	N/A
G	24.5	Tiva Canyon Crystal-Poor Vitric	N/A	N/A
F	35.2	Yucca Mountain Tuff	21	15.9
E	45.0	Yucca Mountain Tuff	21	16.5
D	55.9	Pah Canyon Tuff	21	20.3
C	88.2	Pah Canyon Tuff	16	26.5
B	104.1	Topopah Spring Crystal-Rich Vitric	15	23.7
A	112.0	Topopah Spring Crystal-Rich Nonlithophysal	16	22.9

N/A = Not analyzed

Source: Patterson et al. (1996, Figure 8)

Figure 8.4-6. Pneumatic Pressure Record and the Results of Cross-Spectral Analysis for Borehole UZ#4 Prior to the Exploratory Studies Facility Excavation

C050

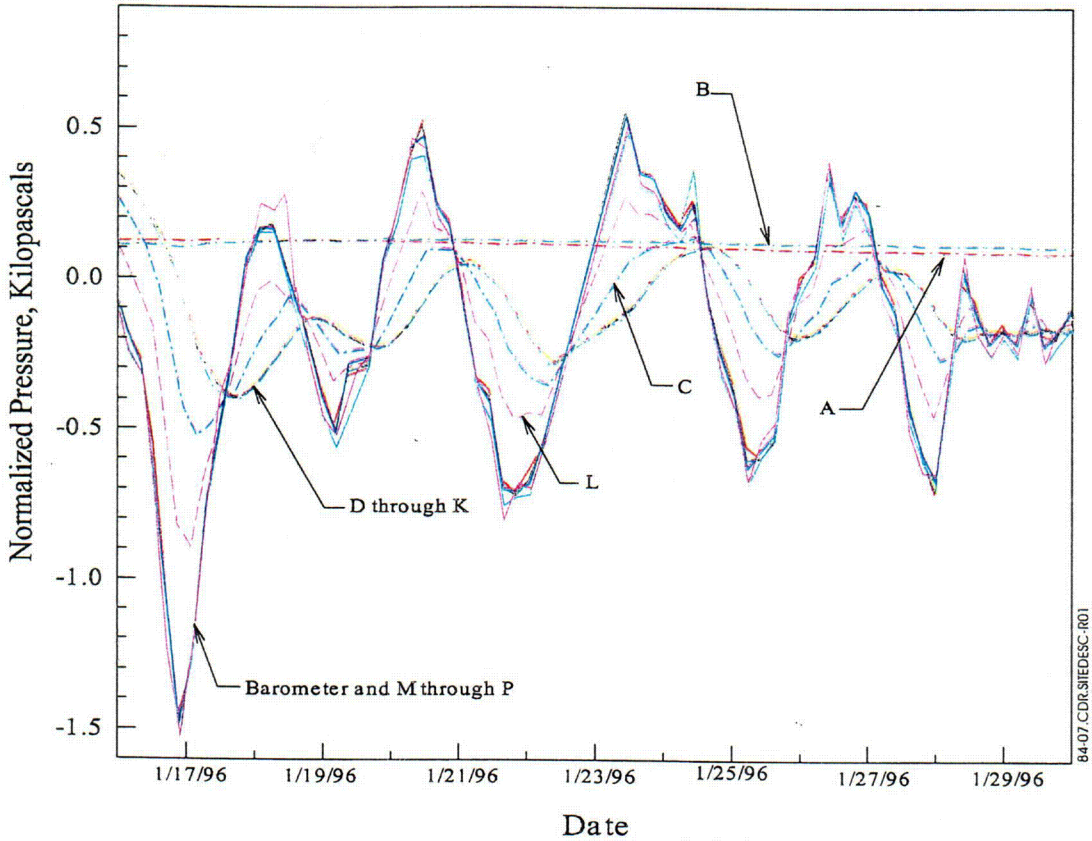

Instrument Station	Depth (meters)	Lithology	Residual Amplitude (percent)	Phase Lag (hours)
M-P	24.6-76.7	Tiva Canyon Tuff	100	N/A
L	91.8	Pre-Pah Canyon Tuff bedded tuff	69	7.4
K	106.8	Topopah Spring Crystal-Rich Nonlithophysal	50	28.0
J	128.9	Topopah Spring Crystal-Rich Nonlithophysal	50	27.9
I	170.8	Topopah Spring Upper Lithophysal	50	28.1
H	208.1	Topopah Spring Middle Nonlithophysal	51	28.1
G	236.8	Topopah Spring Middle Nonlithophysal	51	28.0
F	256.5	Topopah Spring Lower Lithophysal	51	28.8
E	285.1	Topopah Spring Lower Lithophysal	52	29.6
D	322.6	Topopah Spring Lower Nonlithophysal	52	29.7
C	385.7	Topopah Spring Lower Nonlithophysal	57	18.8

N/A = Not analyzed

Source: Patterson et al. (1996, Figure 10)

Figure 8.4-7. Pneumatic Pressure Record and the Results of Cross-Spectral Analysis for Borehole SD-12 Prior to the Exploratory Studies Facility Excavation

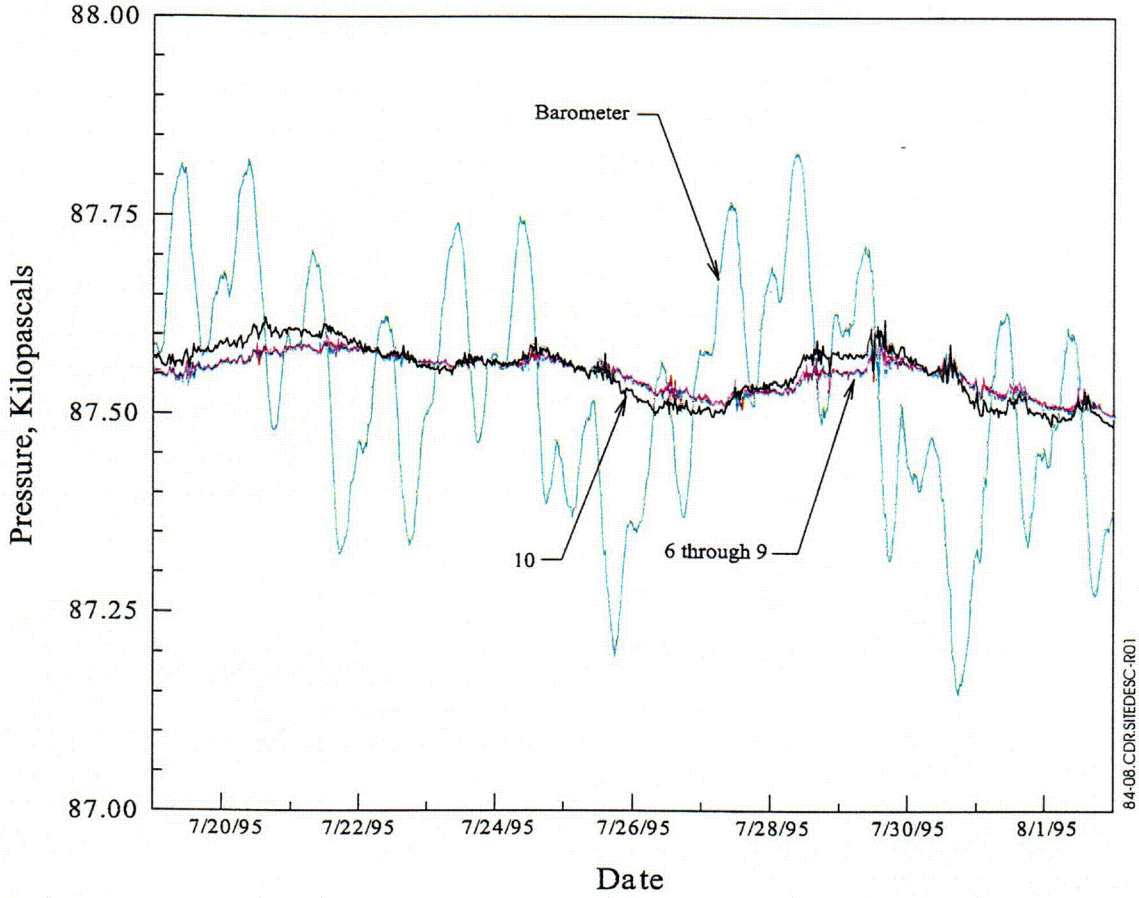

Instrument Station	Depth (meters)	Lithology	Residual Amplitude (percent)	Phase Lag (hours)
6	107.9	Topopah Spring Crystal-Rich Nonlithophysal	30	47.9
7	125.0	Topopah Spring Crystal-Rich Nonlithophysal	29	47.8
8	158.8	Topopah Spring Upper Lithophysal	29	47.9
9	192.9	Topopah Spring Upper Lithophysal	29	48.3
10	226 8	Topopah Spring Upper Lithophysal	39	37 7

Source: Patterson et al. (1996, Figure 5b)

Figure 8.4-8. Pneumatic Pressure Record and Results of Cross-Spectral Analysis for Instrument Stations 6 through 10 in Borehole NRG#5 Prior to the Exploratory Studies Facility Excavation

C052

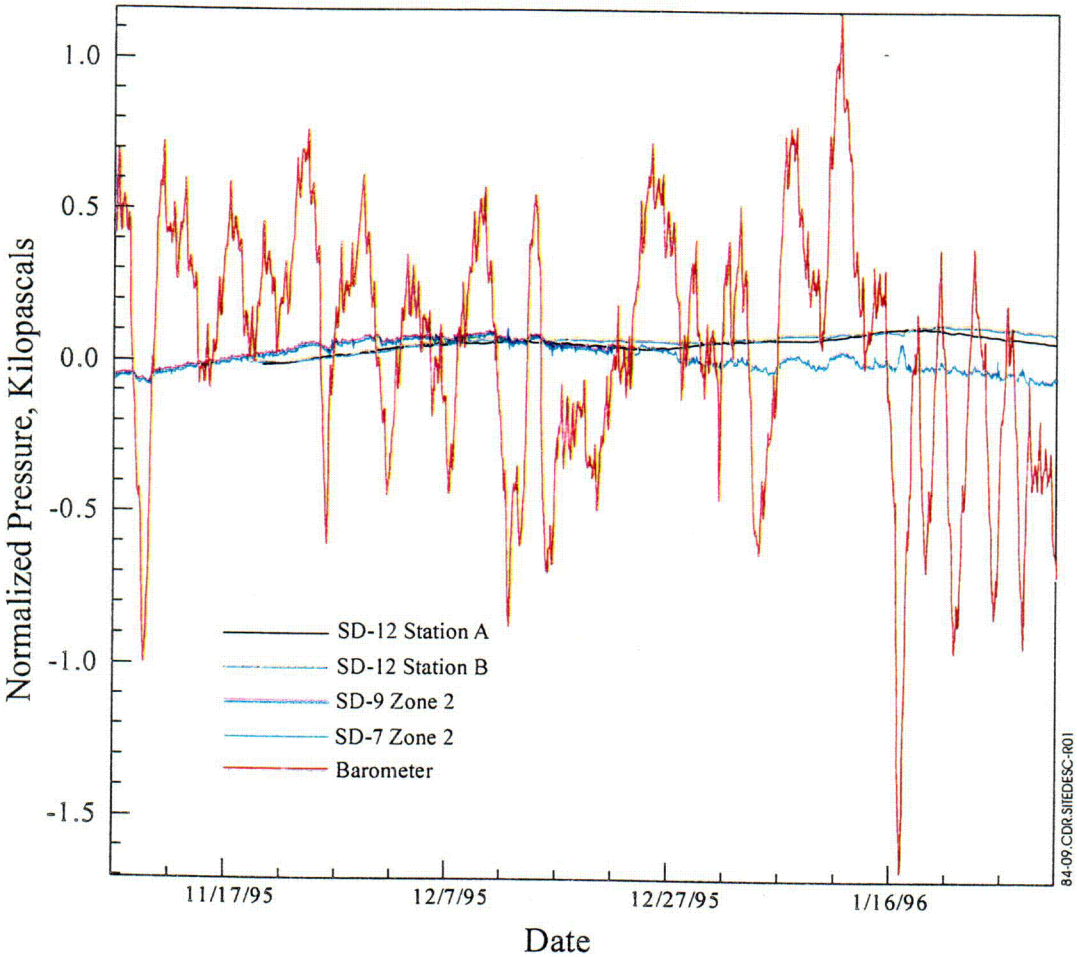

Source: Patterson et al. (1996, Figure 14)

Figure 8.4-9. Pneumatic Pressure Records from Monitoring Locations below Perched-Water Zones in Boreholes SD-7, SD-9, and SD-12

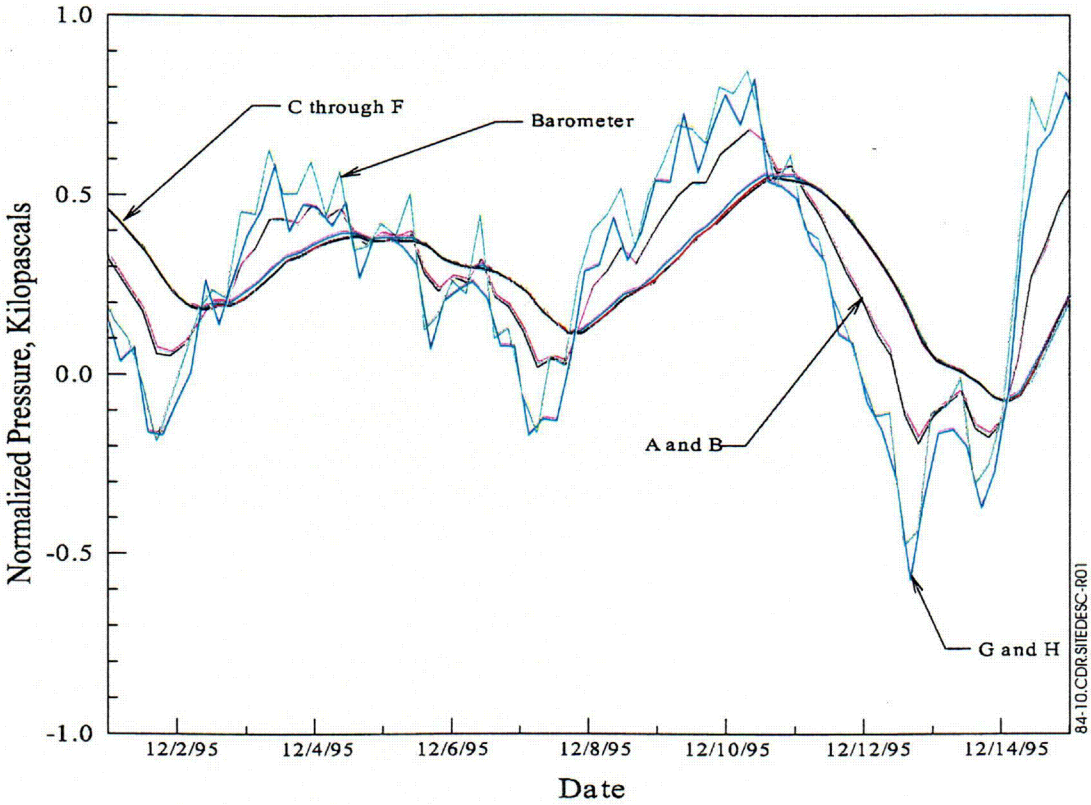

Instrument Station	Depth (meters)	Lithology	Residual Amplitude (percent)	Phase Lag (hours)
H	11.1	Alluvium/Colluvium	100	1.5
G	24.5	Tiva Canyon Crystal-Poor Vitric	100	1.9
F	35.2	Yucca Mountain Tuff	62	26.2
E	45.0	Yucca Mountain Tuff	62	26.7
D	55.9	Pah Canyon Tuff	62	27.0
C	88.2	Pah Canyon Tuff	62	25.6
B	104.1	Topopah Spring Crystal-Rich Vitric	76	10.8
A	112.0	Topopah Spring Crystal-Rich Nonlithophysal	77	10.2

Source: Patterson et al. (1996, Figure 17)

Figure 8.4-10. Pneumatic Pressure Record and Results of Cross-Spectral Analysis for Borehole UZ#4 after the Exploratory Studies Facility Excavation

C054

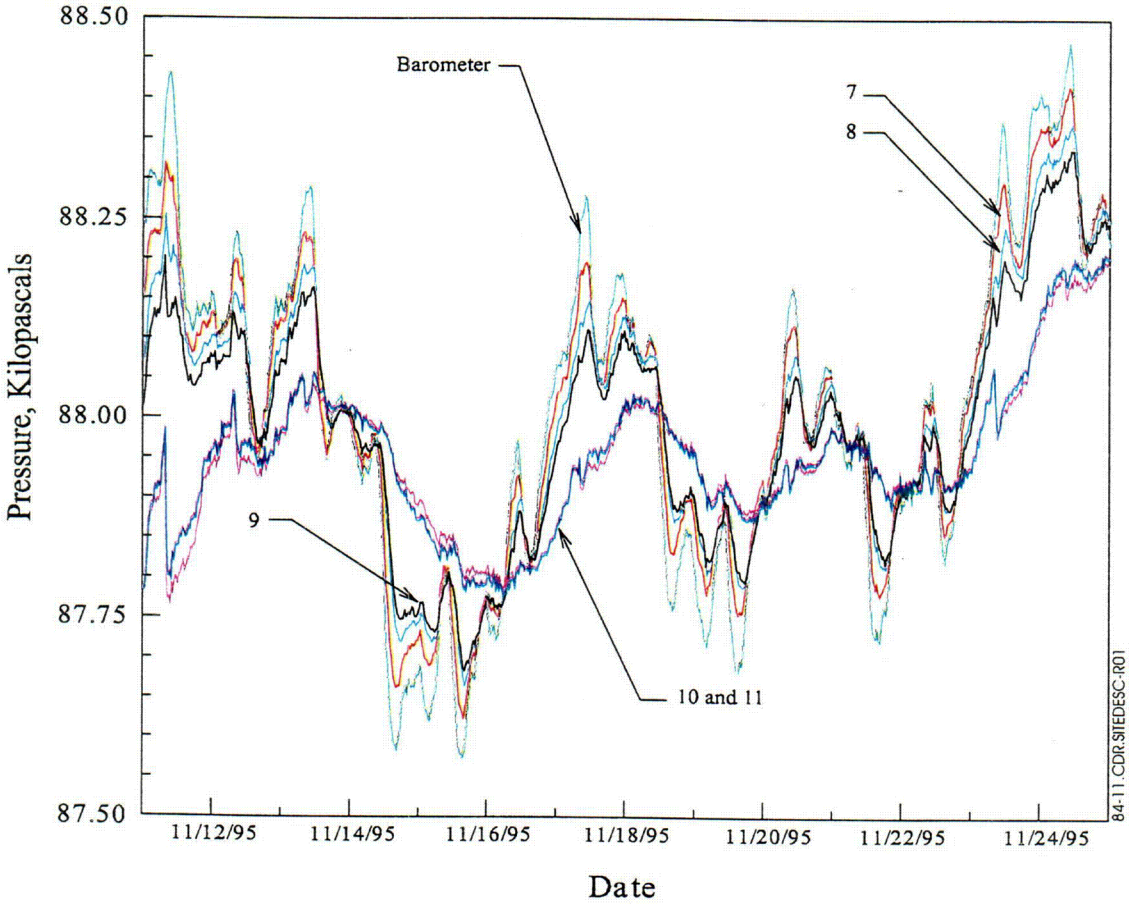

Instrument Station	Depth (meters)	Lithology	Residual Amplitude (percent)	Phase Lag (hours)
7	125.0	Topopah Spring Crystal-Rich Nonlithophysal	86	2.5
8	158.8	Topopah Spring Upper Lithophysal	79	4.6
9	192.9	Topopah Spring Upper Lithophysal	73	6.2
10	226.8	Topopah Spring Upper Lithophysal	48	19.0
11	243.5	Topopah Spring Middle Nonlithophysal	51	17.2

Source: Patterson et al. (1996, Figure 20b)

Figure 8.4-11. Pneumatic Pressure Record and Results of Cross-Spectral Analysis for Instrument Stations 7 through 11 in Borehole NRG#5 after the Exploratory Studies Facility Excavation

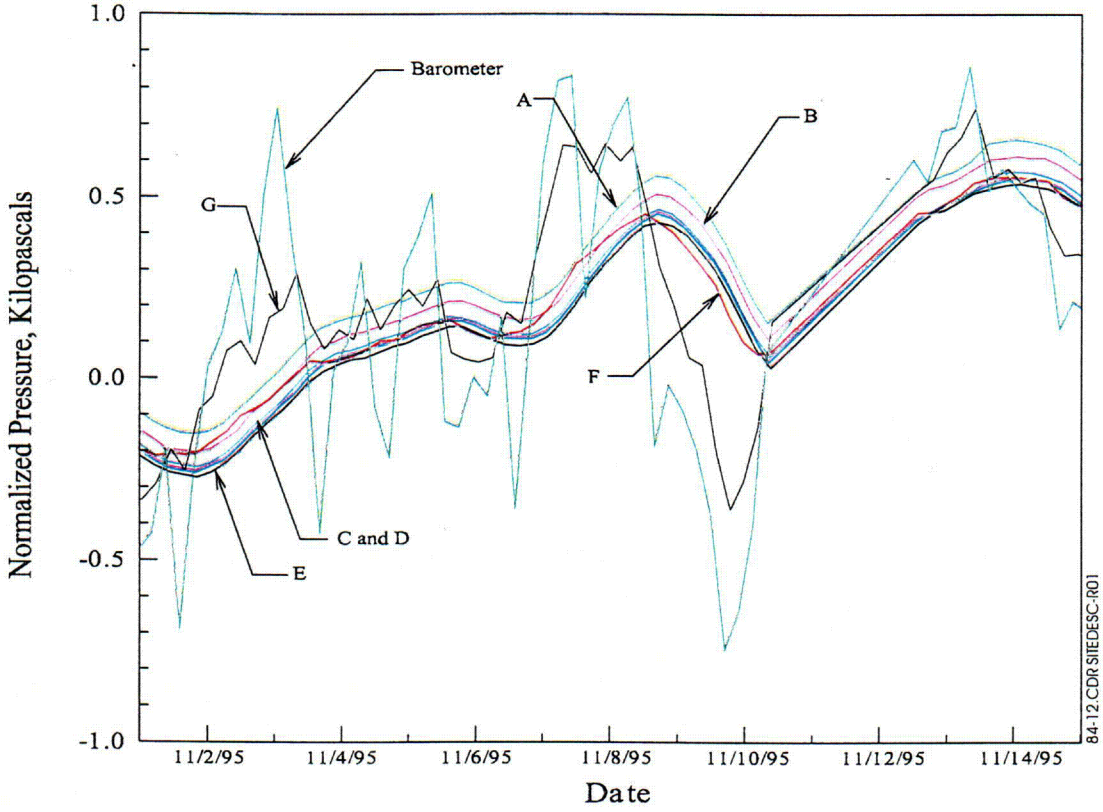

Instrument Station	Depth (meters)	Lithology	Residual Amplitude (percent)	Phase Lag (hours)
G	39.6	Tiva Canyon Columnar	72	5.2
F	54.9	Pah Canyon Tuff	42	29.0
E	85.3	Topopah Spring Crystal-Rich Nonlithophysal	48	33.5
D	106.8	Topopah Spring Crystal-Rich Nonlithophysal	48	33.4
C	138.8	Topopah Spring Upper Lithophysal	48	33.6
B	163.1	Topopah Spring Upper Lithophysal	49	33.7
A	219.4	Topopah Spring Middle Nonlithophysal	49	33.8

Source: Patterson et al. (1996, Figure 22)

Figure 8.4-12. Pneumatic Pressure Record and Results of Cross-Spectral Analysis for Borehole NRG-6 after the Exploratory Studies Facility Excavation

C056

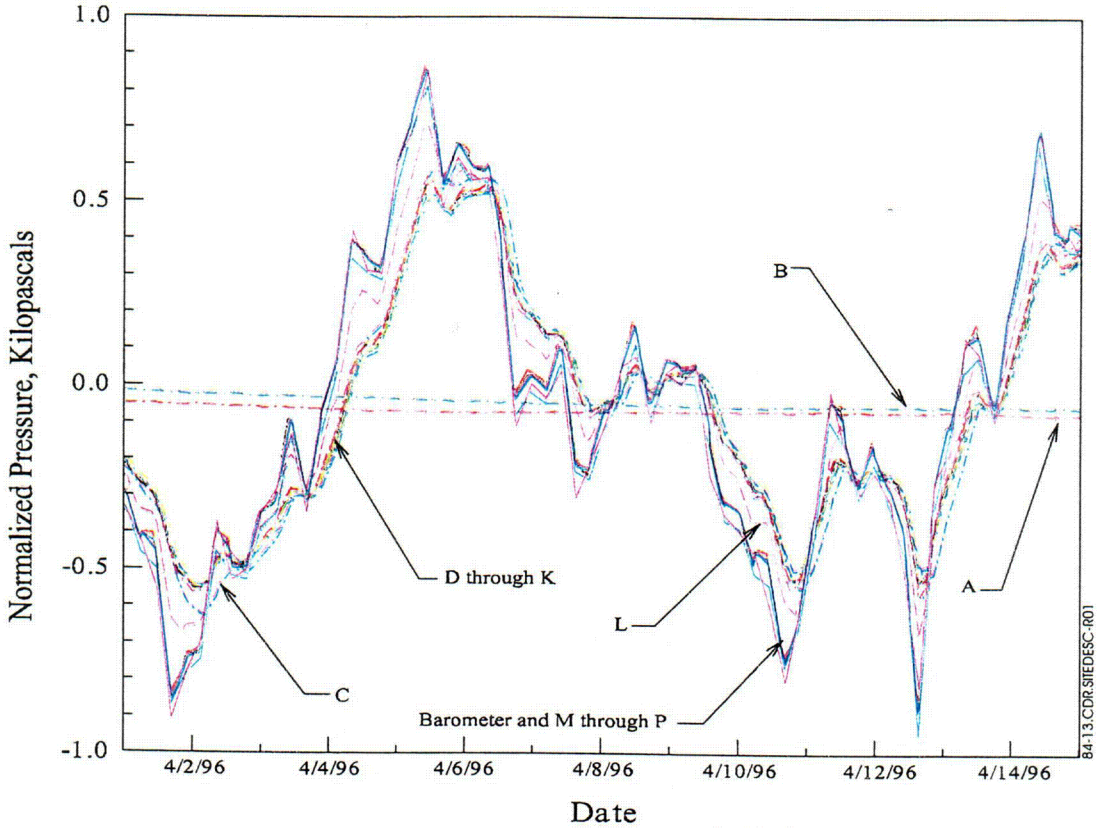

Instrument Station	Depth (meters)	Lithology	Residual Amplitude (percent)	Phase Lag (hours)
N-P	24.6-65.3	Tiva Canyon Tuff	100	0.3
M	76.7	Tiva Canyon Crystal-Poor Vitric	100	0.6
L	91.8	Pre-Pah Canyon Tuff bedded tuff	85	4.4
K	106.8	Topopah Spring Crystal-Rich Nonlithophysal	69	10.3
J	128.9	Topopah Spring Crystal-Rich Nonlithophysal	69	10.4
I	170.8	Topopah Spring Upper Lithophysal	70	10.2
H	208.1	Topopah Spring Middle Nonlithophysal	71	9.3
G	236.8	Topopah Spring Middle Nonlithophysal	72	8.8
F	256.5	Topopah Spring Lower Lithophysal	74	8.2
E	285.1	Topopah Spring Lower Lithophysal	74	8.3
D	322.6	Topopah Spring Lower Nonlithophysal	74	8.6
C	385.7	Topopah Spring Lower Nonlithophysal	80	9.8

Source: Patterson et al. (1996, Figure 26)

Figure 8.4-13. Pneumatic Pressure Record and Results of Cross-Spectral Analysis for Borehole SD-12 after the Exploratory Studies Facility Excavation

INTENTIONALLY LEFT BLANK

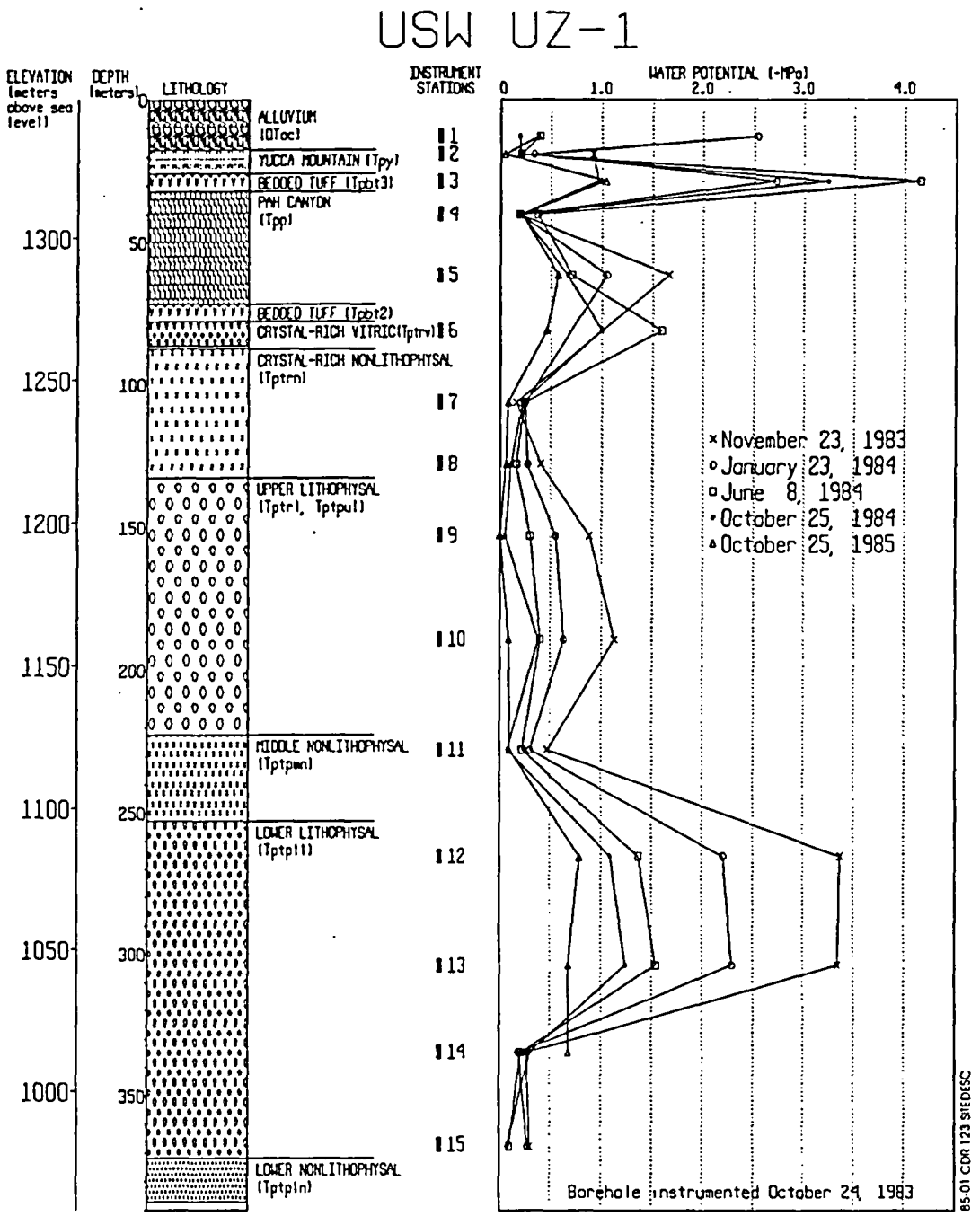

Source: Rousseau et al. (1999, Figure 92)

Figure 8.5-1. Time-Series Water Potential Profiles (November 1983 through October 1995) for Prototype Borehole UZ-1 in Drill Hole Wash

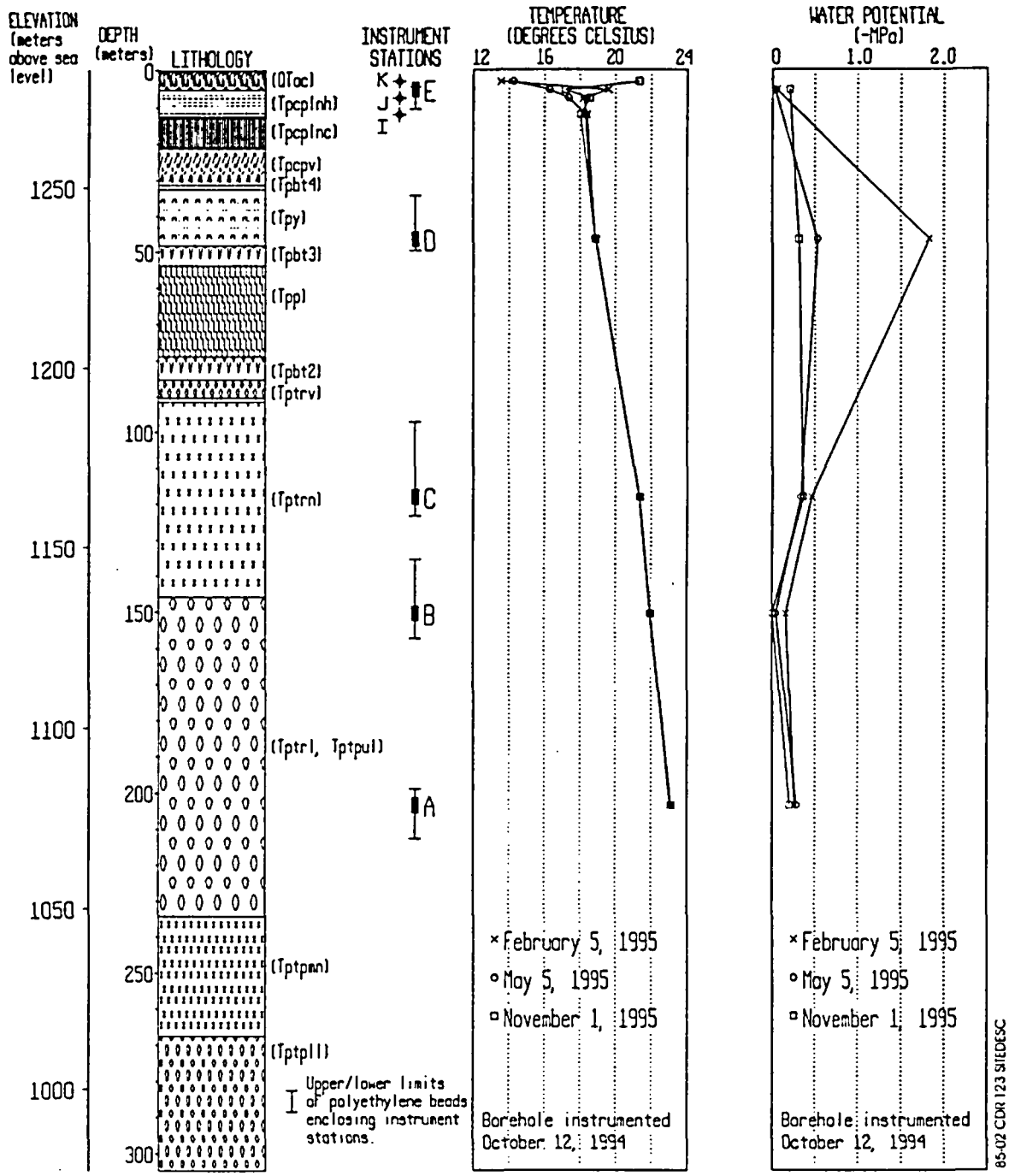

Source: Rousseau et al. (1999, Figure 93)

Figure 8.5-2. Selected Temperature and Water Potential Profiles for Borehole NRG-7a

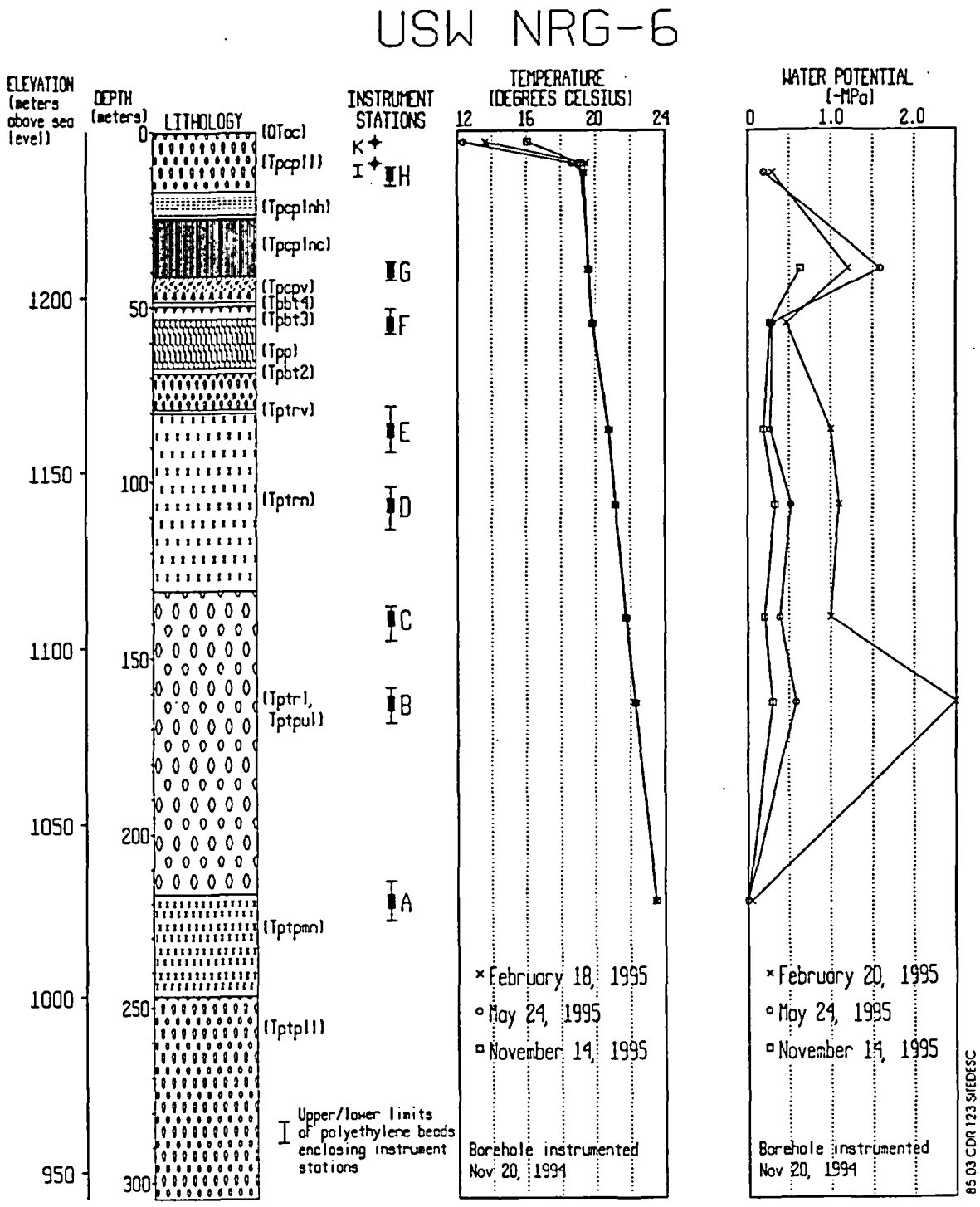

Source: Rousseau et al. (1999, Figure 94)

Figure 8.5-3. Selected Temperature and Water Potential Profiles for Borehole NRG-6

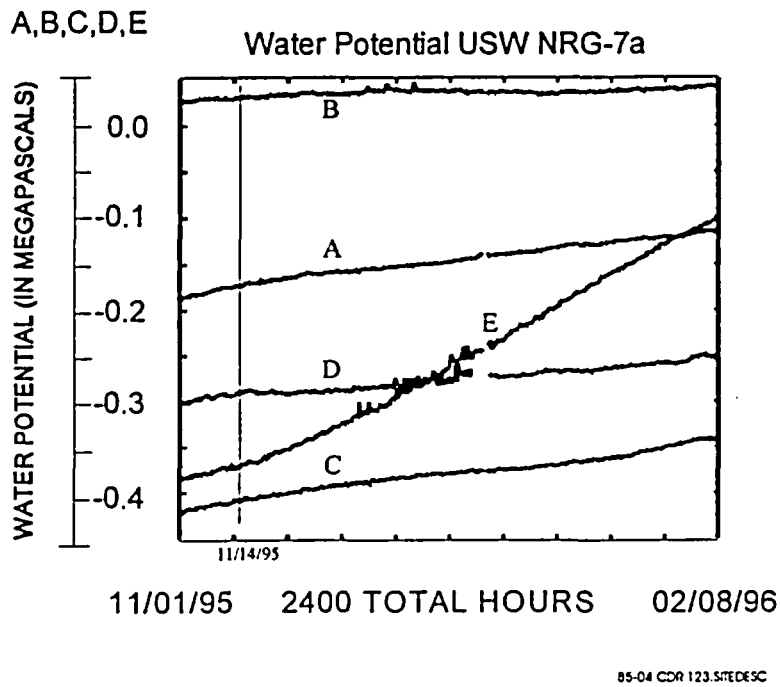

Source: Rousseau et al. (1999, Figure 95)

Figure 8.5-4. Time-Series Water Potential Records for Instrument Stations in Borehole NRG-7a

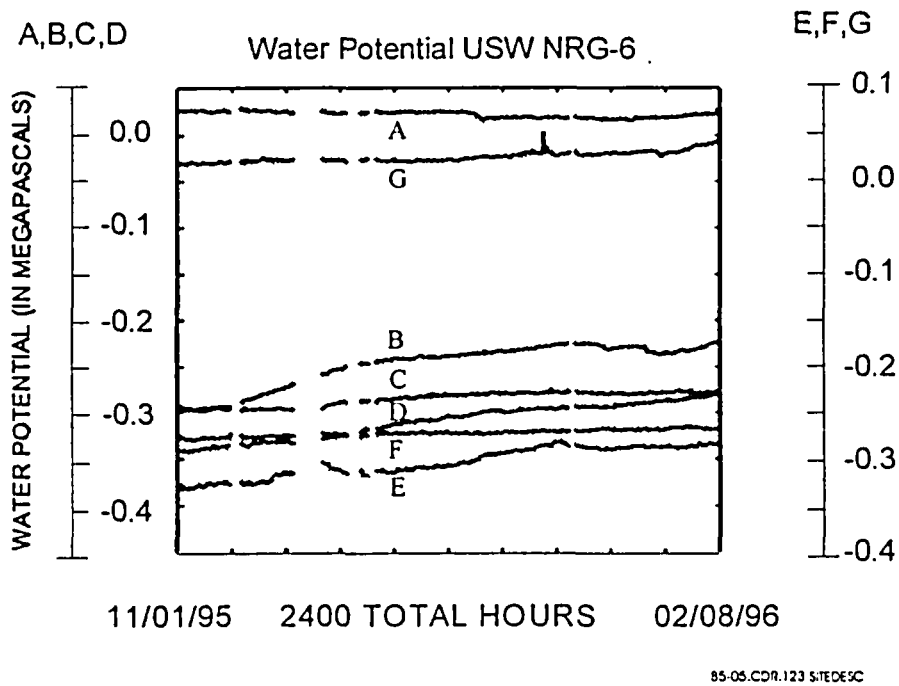

Source: Rousseau et al. (1999, Figure 96)

Figure 8.5-5. Time-Series Water Potential Records for Instrument Stations in Borehole NRG-6

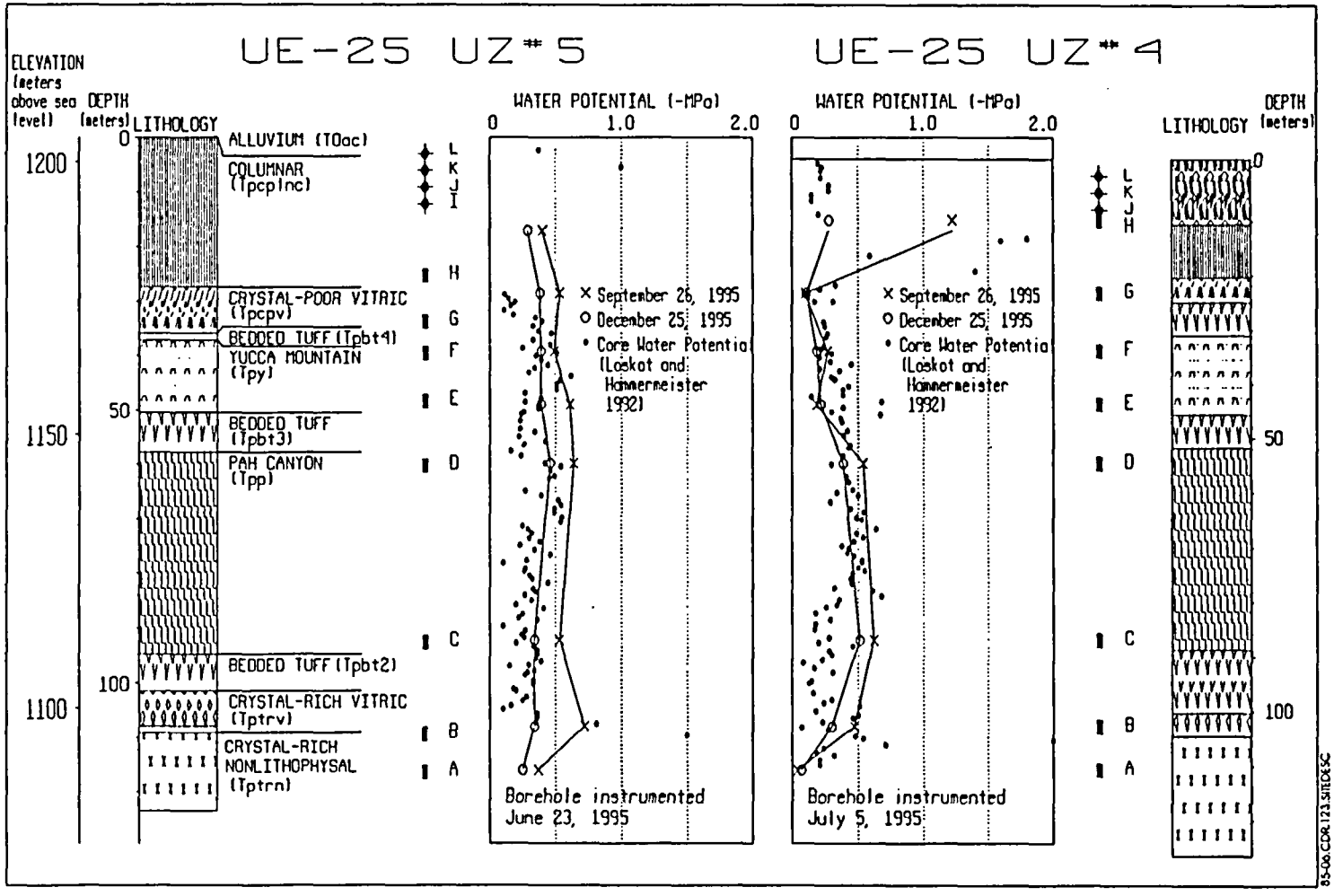

Source: Rousseau et al. (1999, Figure 97)

Figure 8.5-6. In Situ and Core Sample Water Potentials for Boreholes UZ#4 and UZ#5 in Pagany Wash

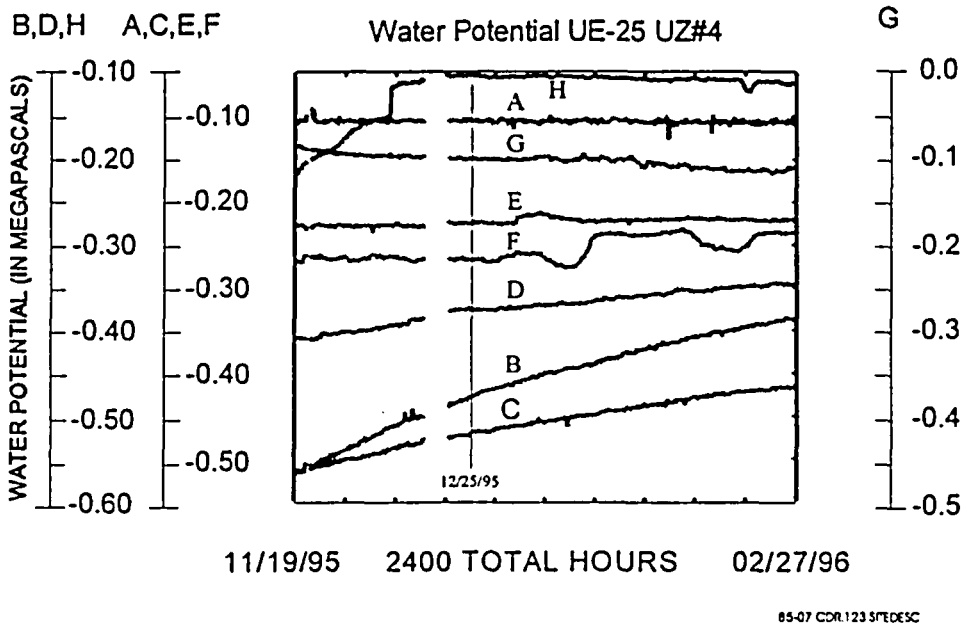

Source: Rousseau et al. (1999, Figure 98)

Figure 8.5-7. Time-Series Water Potential Records for Instrument Stations in Borehole UZ#4

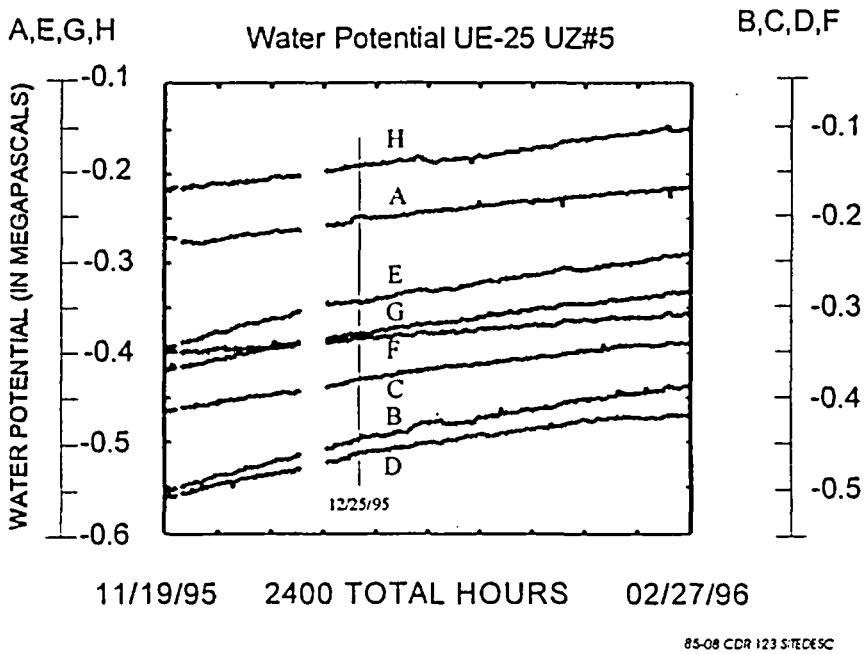

Source: Rousseau et al. (1999, Figure 99)

Figure 8.5-8. Time-Series Water Potential Records for Instrument Stations in Borehole UZ#5

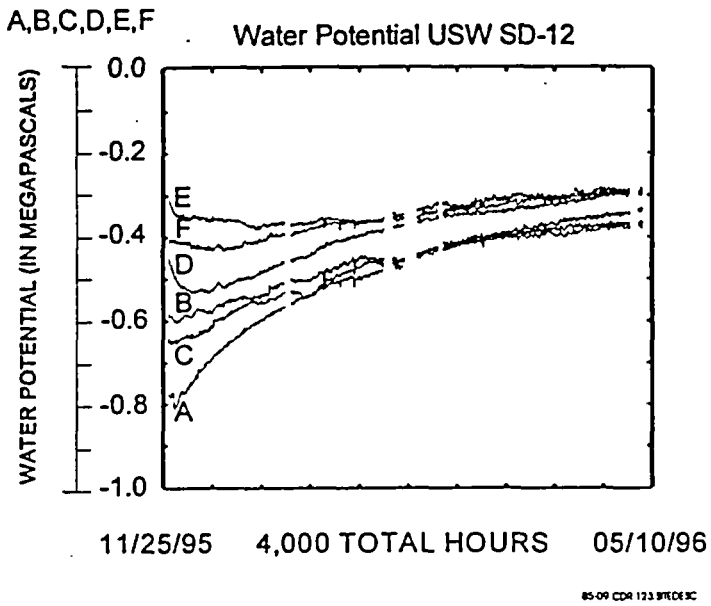

Source: Rousseau et al. (1997, Figure 4.2.1-2)

Figure 8.5-9. Time-Series Water Potential Records for Borehole SD-12 for Instrument Station A in the Calico Hills Nonwelded Unit, Station B in the Topopah Spring Welded Basal Vitrophyre, and Stations C, D, E, and F in the Topopah Spring Welded Crystal-Poor Lower Nonlithophysal and Lower Lithophysal Units

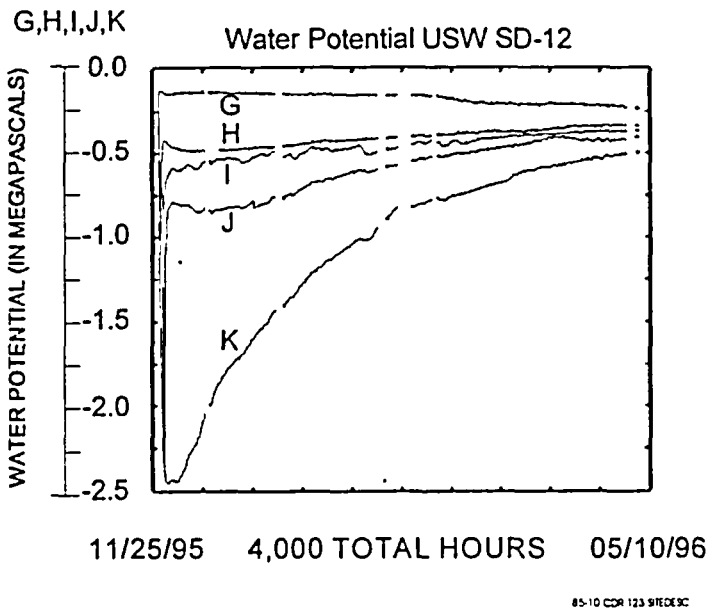

Source: Rousseau et al. (1997, Figure 4.2.1-3)

Figure 8.5-10. Time-Series Water Potential Records for Borehole SD-12 for Instrument Stations G and H in the Topopah Spring Welded Middle Nonlithophysal Unit, Station I in the Topopah Spring Welded Crystal-Poor Upper Lithophysal Unit, and Stations J and K in the Topopah Spring Welded Crystal-Rich Nonlithophysal Unit

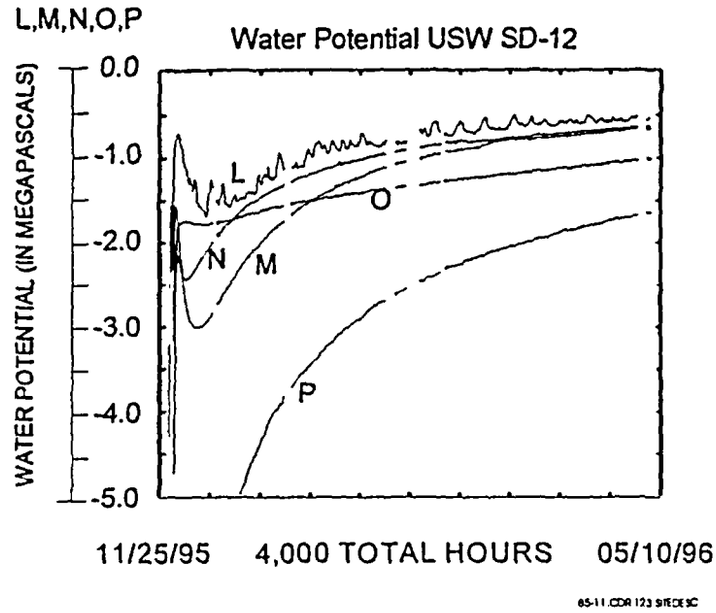

Source: Rousseau et al. (1997, Figure 4.2.1-4)

Figure 8.5-11. Time-Series Water Potential Records for Borehole SD-12 for Instrument Stations L and M in the Paintbrush Nonwelded Unit and Stations N, O, and P in the Tiva Canyon Welded Unit

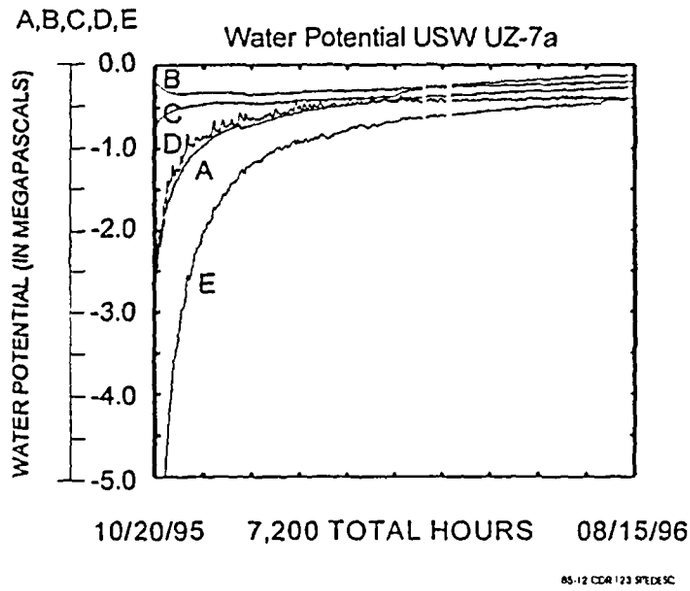

Source: Rousseau et al. (1997, Figure 4.2.1-5)

Figure 8.5-12. Time-Series Water Potential Records for Borehole UZ-7a for Instrument Stations A, B, C, D, and E in the Topopah Spring Welded Hydrogeologic Unit

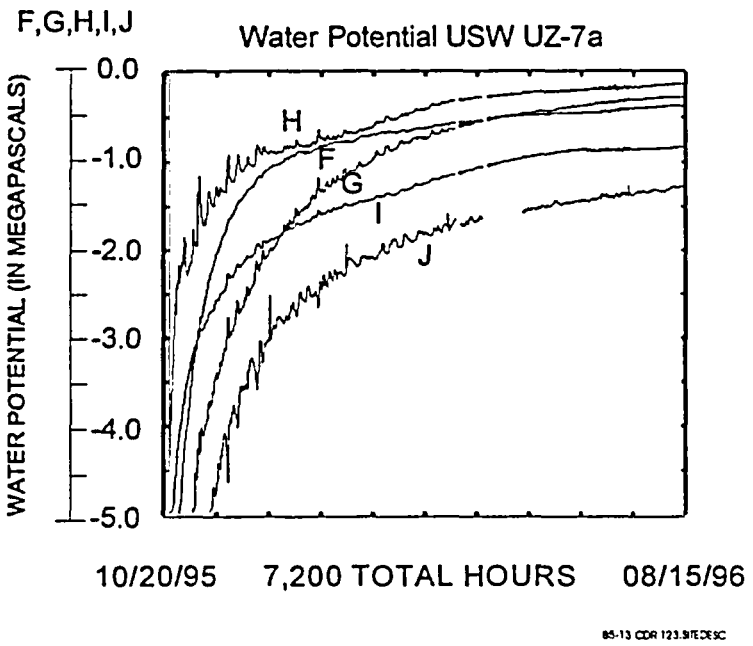

Source: Rousseau et al. (1997, Figure 4.2.1-6)

Figure 8.5-13. Time-Series Water Potential Records for Borehole UZ-7a for Instrument Stations F and G in the Paintbrush Nonwelded Hydrogeologic Unit and Instrument Stations H, I, and J in the Tiva Canyon Welded Hydrogeologic Unit

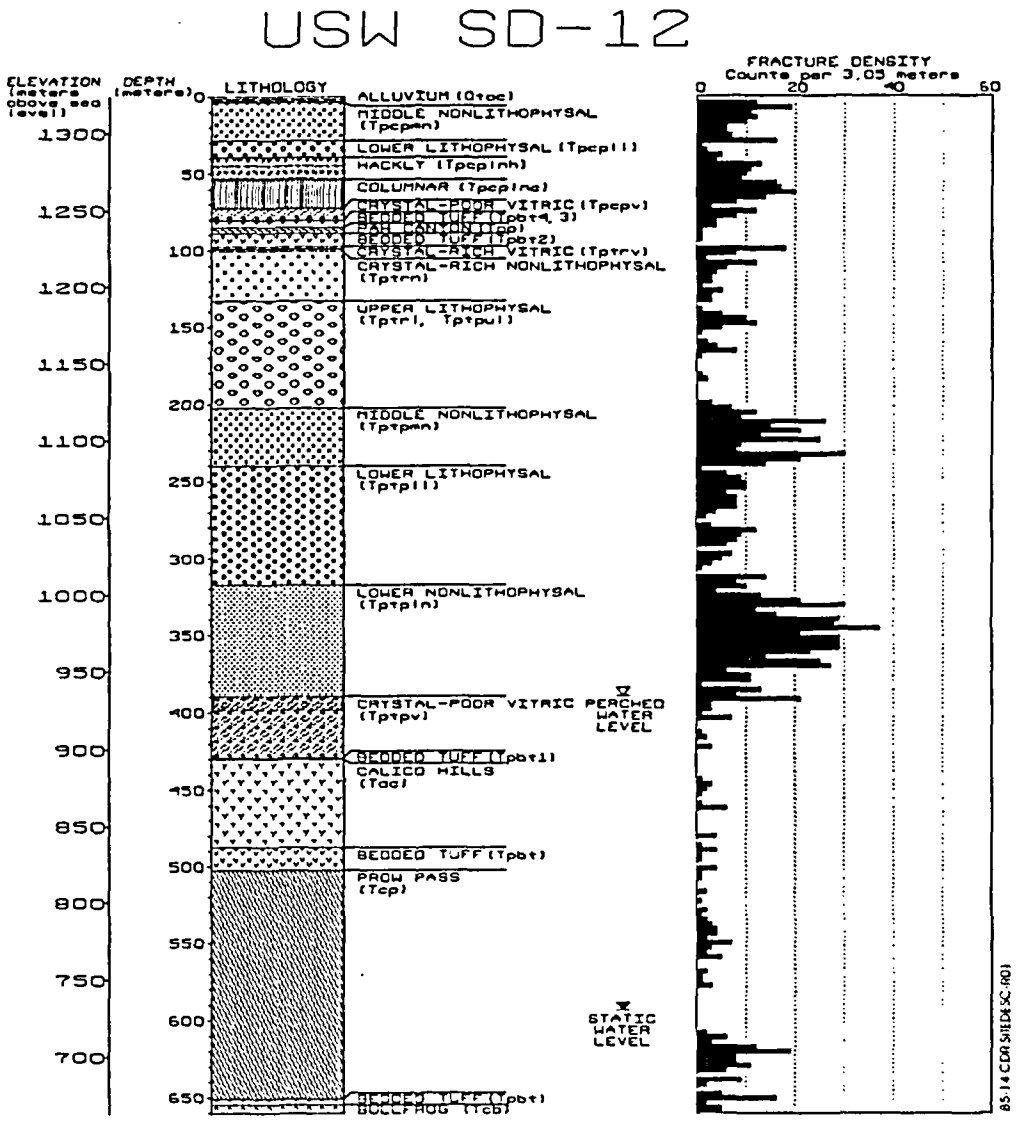

Source: Modified from Rousseau et al. (1997, Figure 3.0-3)

Figure 8.5-14. Lithostratigraphy and Fracture Density for Borehole SD-12

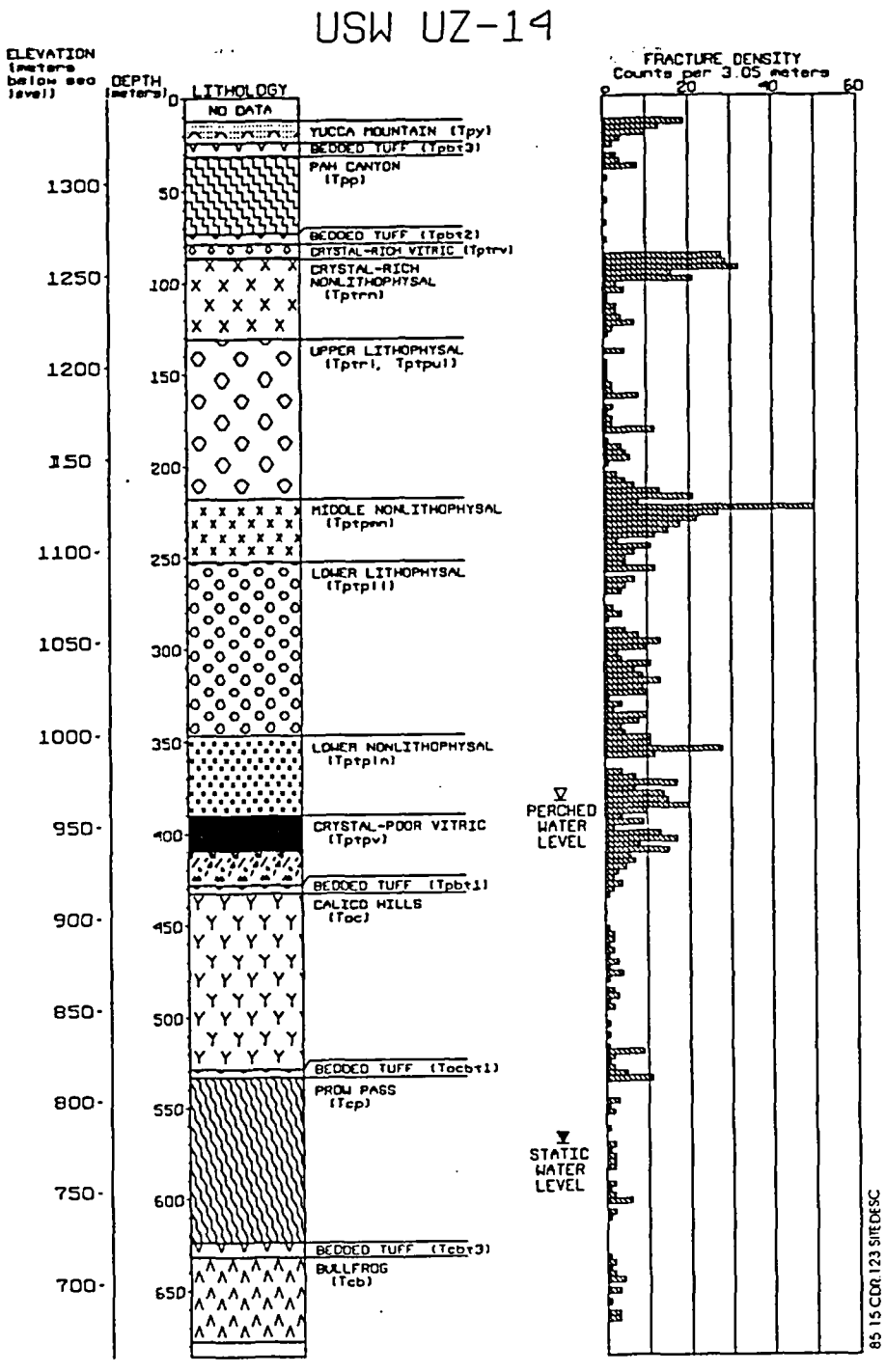

Source: Modified from Rousseau et al. (1999, Figure 24)

Figure 8.5-15. Lithostratigraphy and Fracture Density for Borehole UZ-14

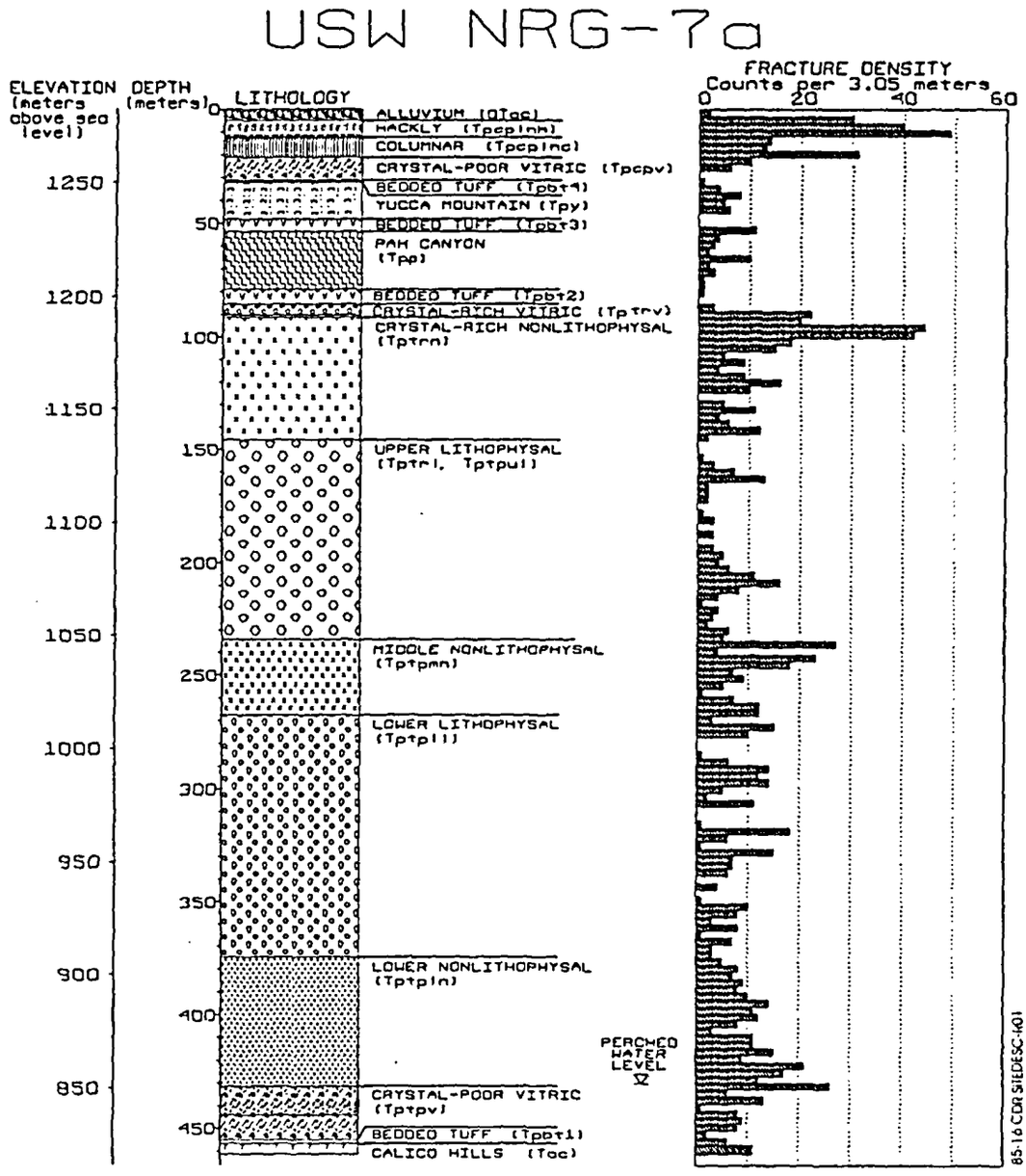

Source: Modified from Rousseau et al. (1999, Figure 25)

Figure 8.5-16. Lithostratigraphy and Fracture Density for Borehole NRG-7a

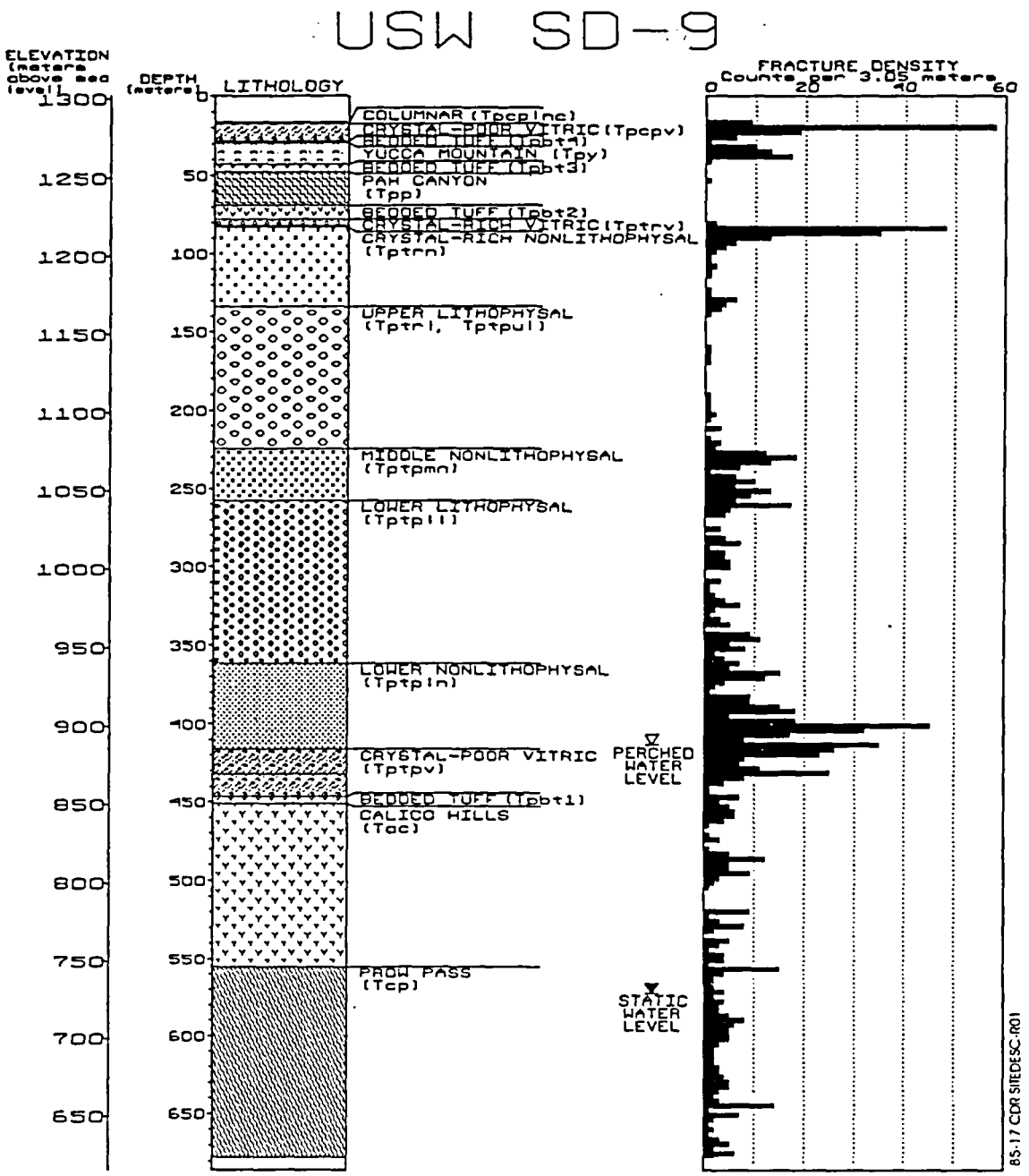

Source: Modified from Rousseau et al. (1999, Figure 24)

Figure 8.5-17. Lithostratigraphy and Fracture Density for Borehole SD-9

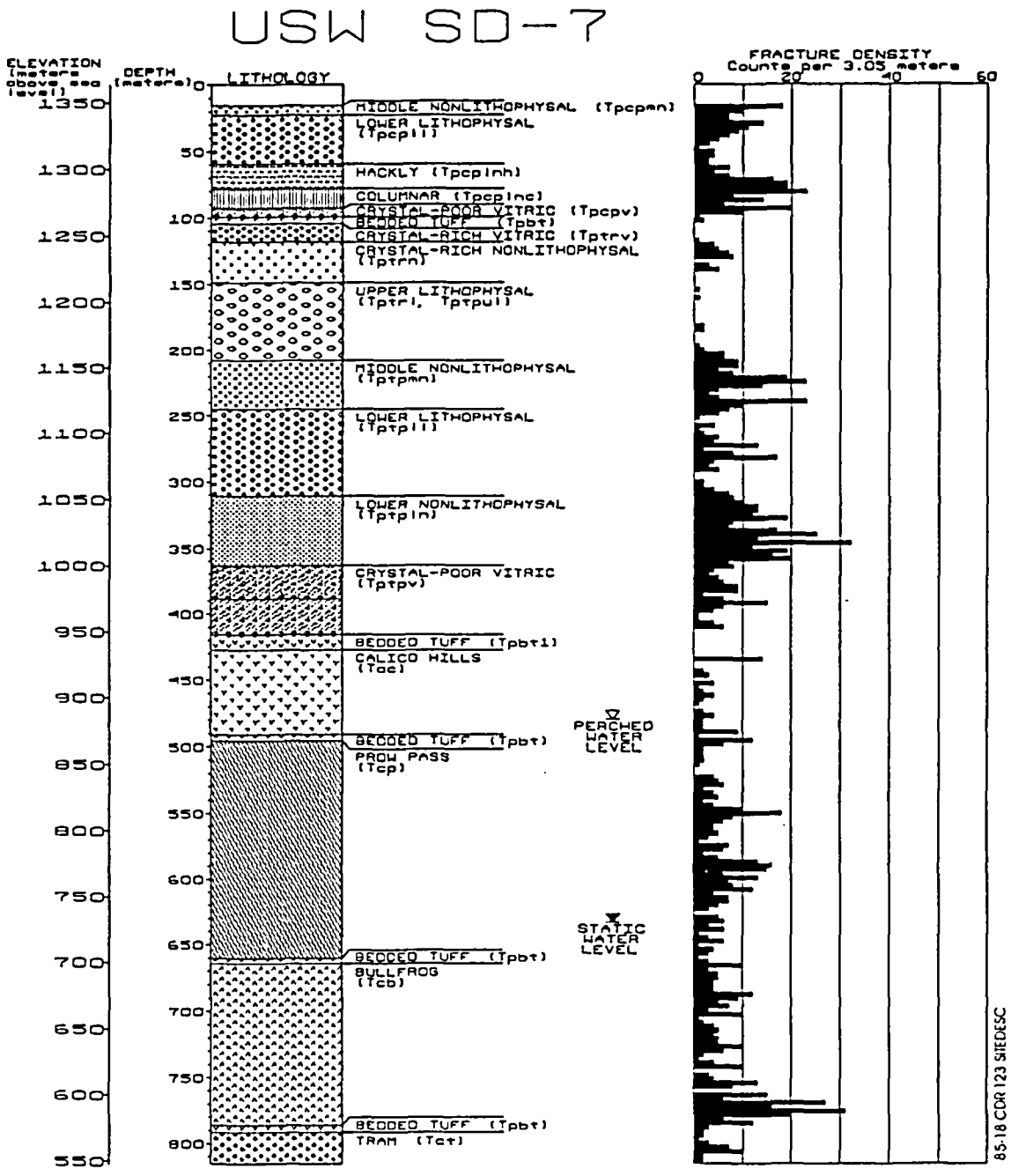

Source: Modified from Rousseau et al. (1997, Figure 3.0-3)

Figure 8.5-18. Lithostratigraphy and Fracture Density for Borehole SD-7

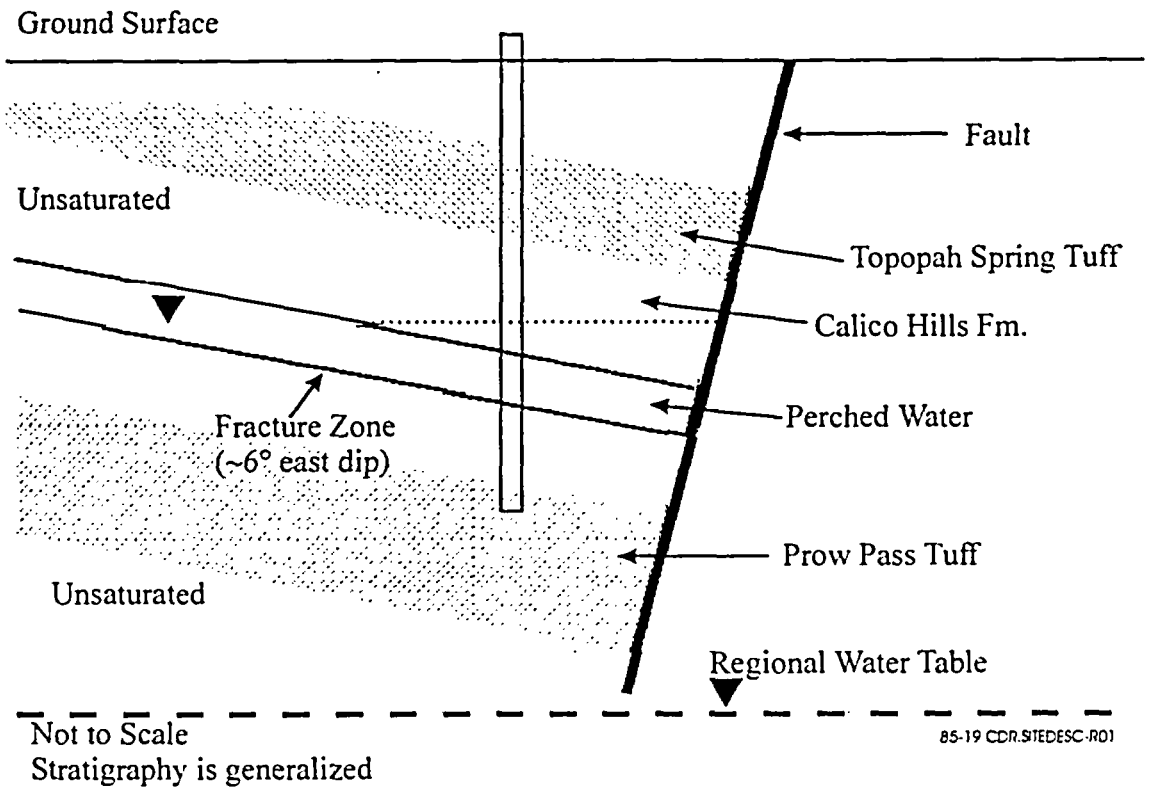

Source: O'Brien (1997, Figure 18)

Figure 8.5-19. Idealized Conceptual Model of the Perched-Water Reservoir at Borehole SD-7

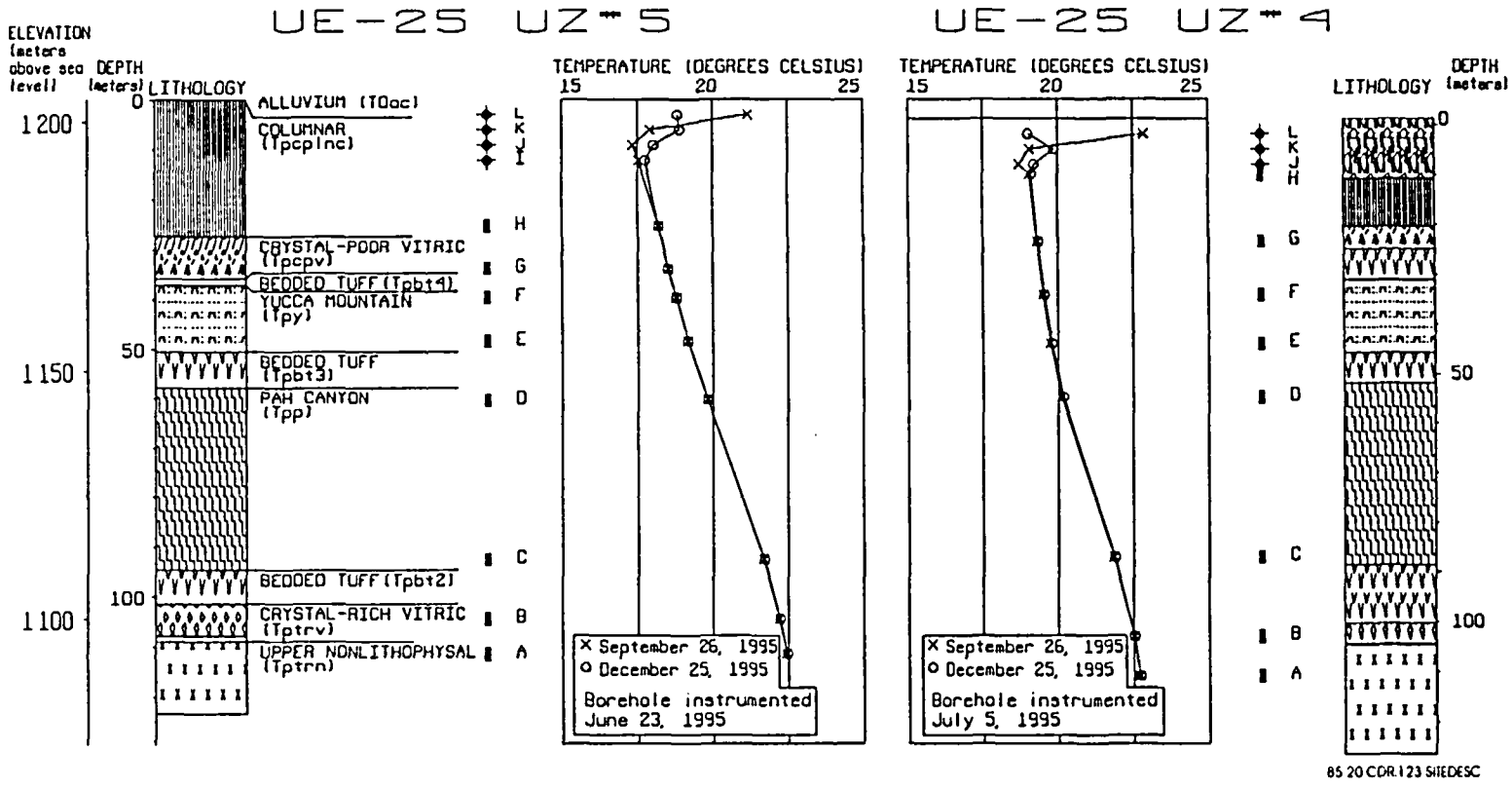

Source: Rousseau, J.P. et al. (1999, Figure 100)

Figure 8.5-20. Selected Temperature Profiles for Boreholes UE-25 UZ#5 and UE-25 UZ#4

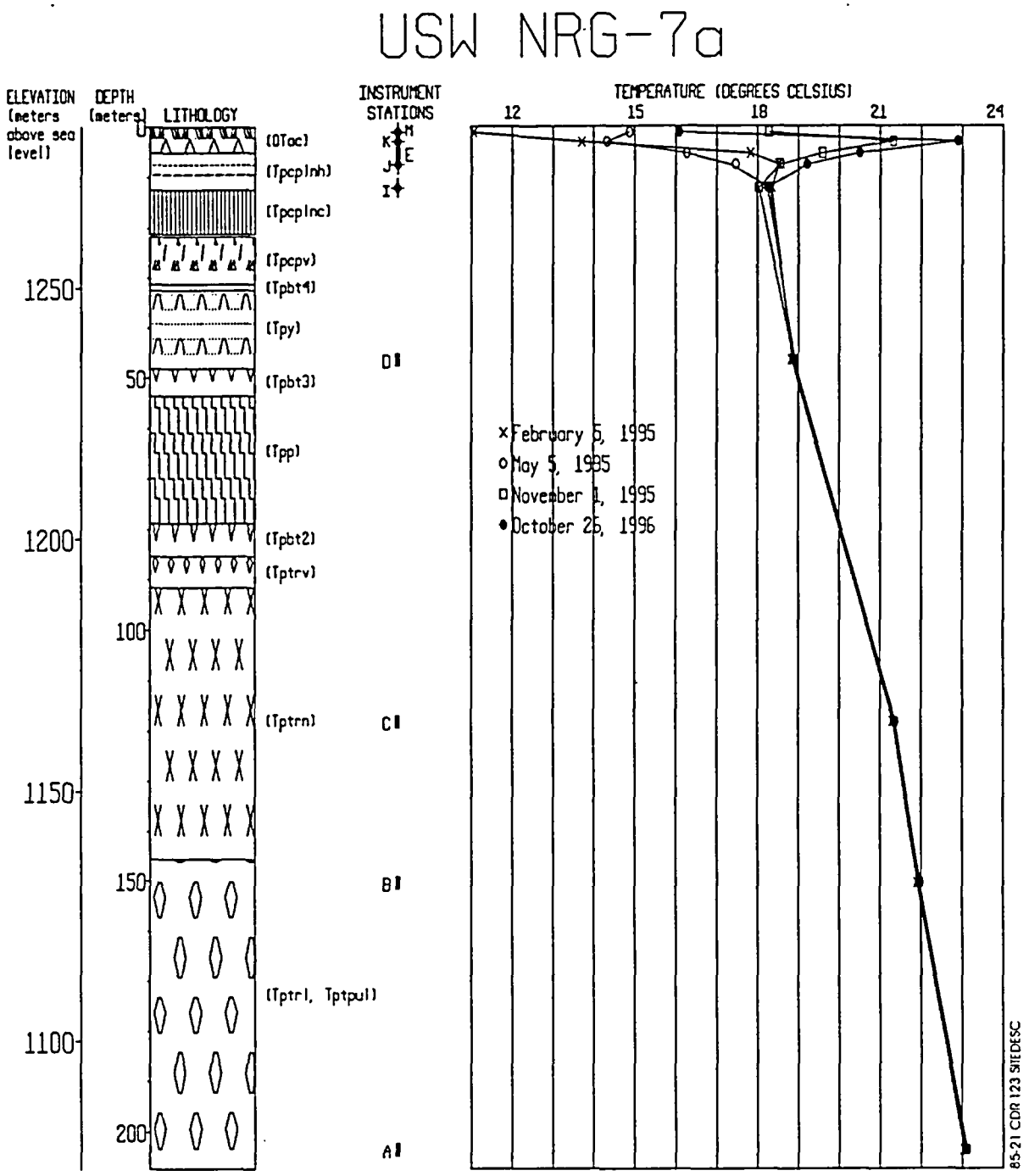

Source: Rousseau, J.P. et al. (1997, Figure 4.3.2-1)

Figure 8.5-21. Time-Lapse Temperature Profiles for Borehole USW NRG-7a

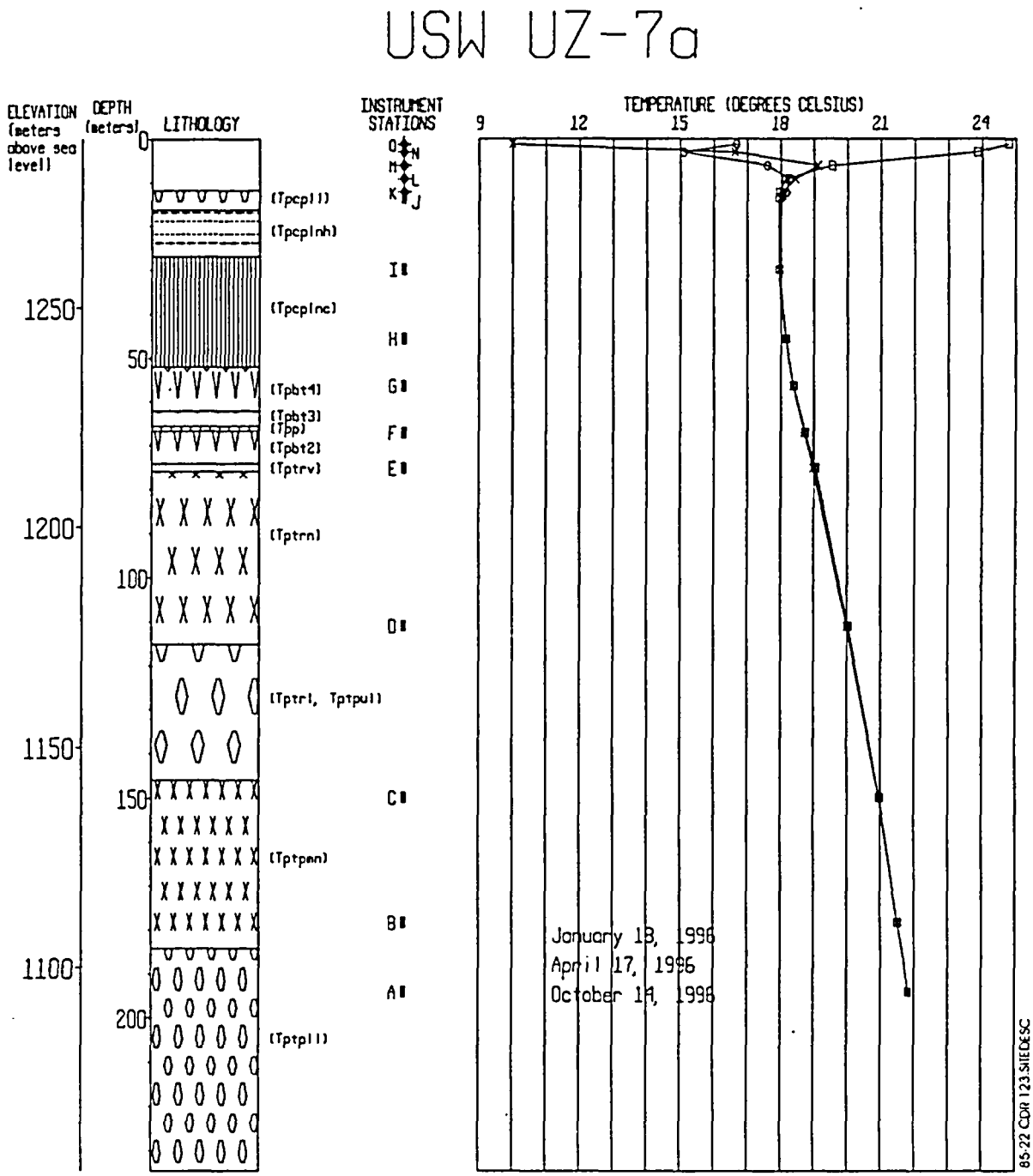

Source: Rousseau, J.P. et al. (1997, Figure 4.3.2-3)

Figure 8.5-22. Time-Lapse Temperature Profiles for Borehole USW UZ-7a

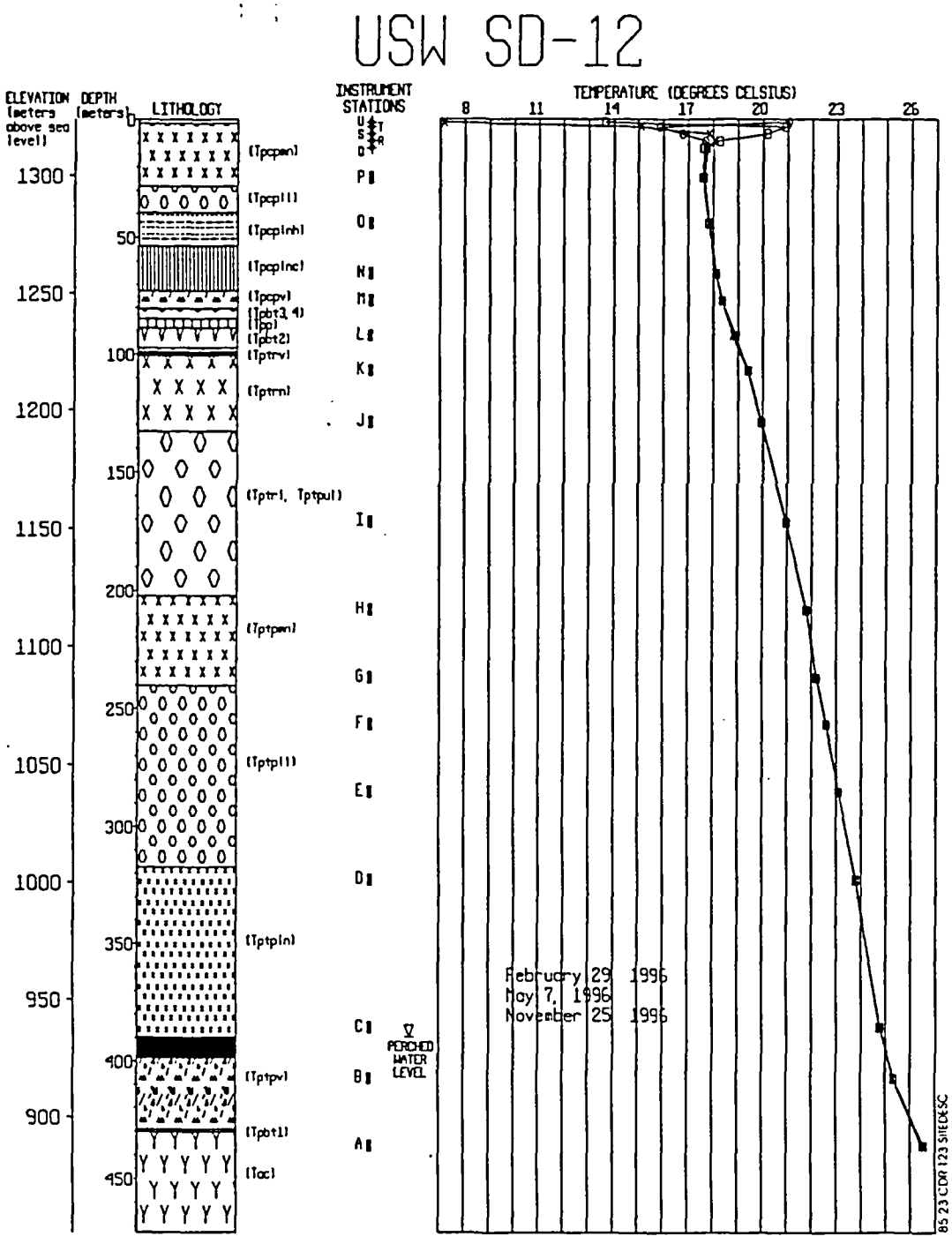

Source: Rousseau, J.P. et al. (1997, Figure 4.3.2-2)

Figure 8.5-23. Time-Lapse Temperature Profiles for Borehole USW SD-12

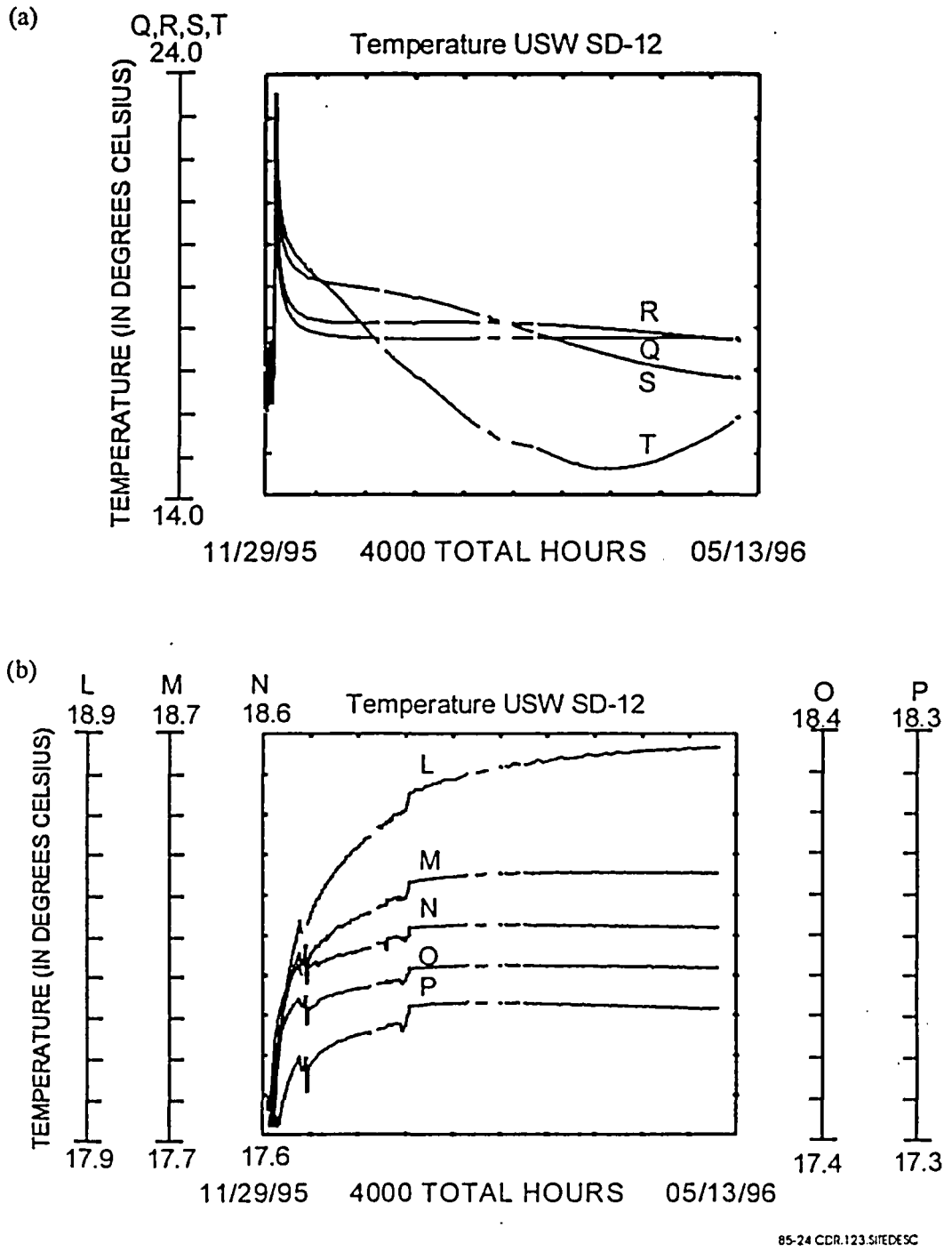

Sources: (a) Rousseau, J.P. et al. (1997, Figure 4.3.1-5); (b) Rousseau, J.P. et al. (1997, Figure 4.3.1-4)

NOTE: (a) Instrument Stations Q to T in the Tiva Canyon welded hydrogeologic unit within the zone of influence of seasonal, surface temperature changes; (b) Instrument Stations L and M in the Paintbrush nonwelded hydrogeologic unit and Instrument Stations N, O, and P in the Tiva Canyon welded hydrogeologic unit

Figure 8.5-24. Time-Series Temperature Records for Instrument Stations L through T in Borehole SD-12

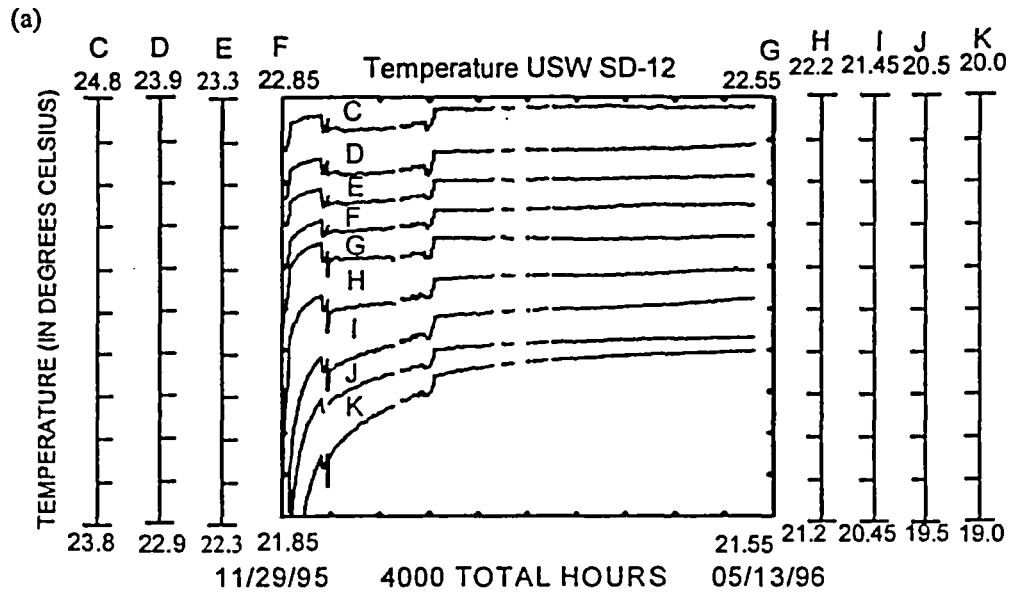

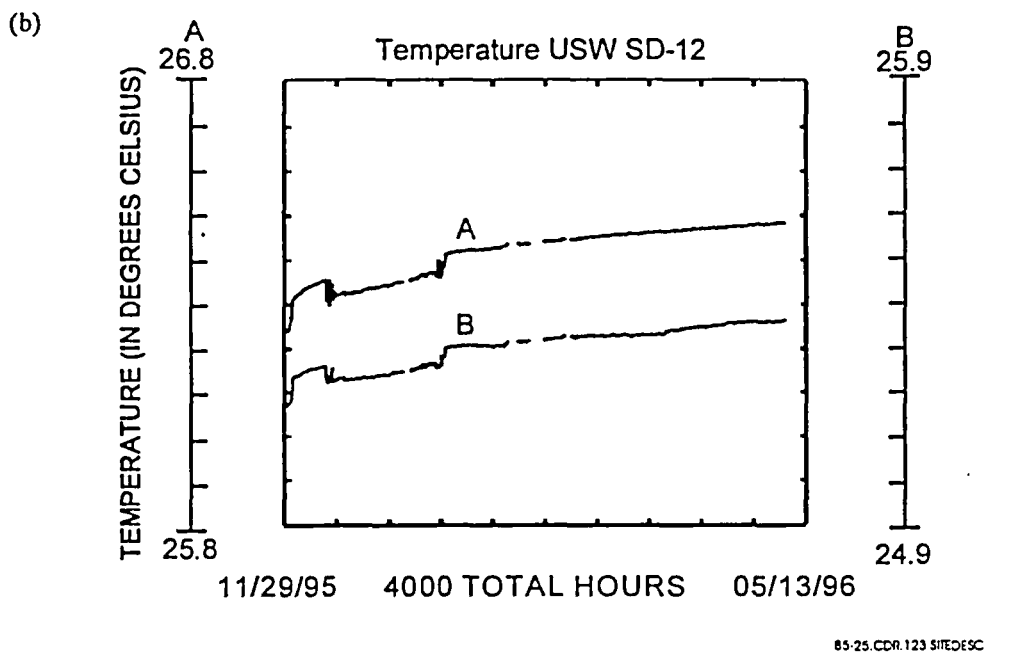

Sources: (a) Rousseau, J.P. et al. (1997, Figure 4.3.1-3); (b) Rousseau, J.P. et al. (1997, Figure 4.3.1-2)

NOTE: (a) Instrument Stations C to K in the Topopah Spring welded hydrogeologic unit; (b) Instrument Station A in the Calico Hills nonwelded hydrogeologic unit and Instrument Station B in the crystal-poor vitric unit of the Topopah Spring welded hydrogeologic unit

Figure 8.5-25. Time-Series Temperature Records for Instrument Stations A through K in Borehole SD-12

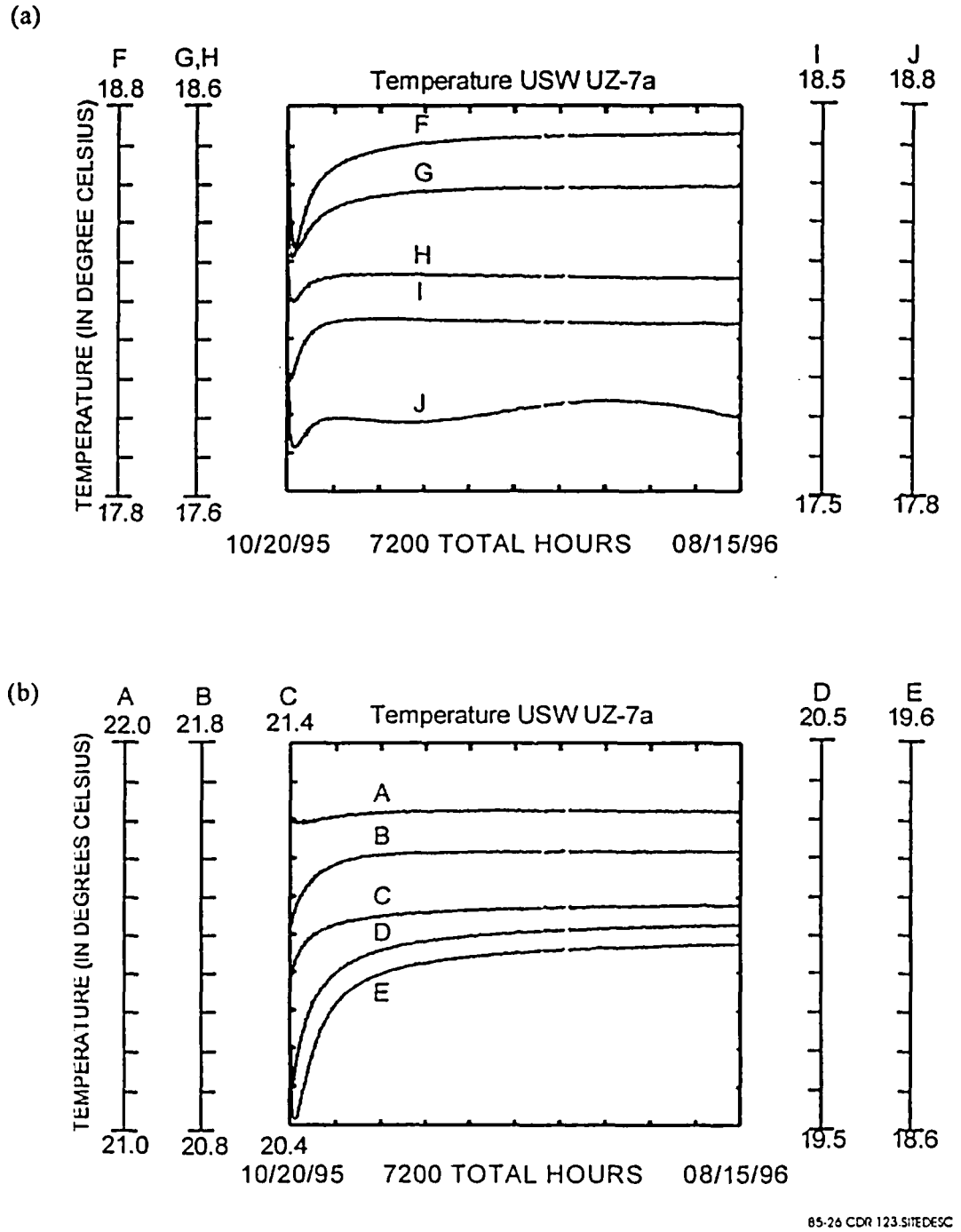

Sources: (a) Rousseau, J.P. et al. (1997, Figure 4.3.1-7); (b) Rousseau, J.P. et al. (1997, Figure 4.3.1-6)

NOTE: (a) Instrument Stations F to G in the Paintbrush nonwelded hydrogeologic unit and Instrument Stations H to J in the Tiva Canyon welded hydrogeologic unit; (b) Instrument Stations A to E in the Topopah Spring welded hydrogeologic unit

Figure 8.5-26. Time-Series Temperature Records for Instrument Stations A through K in Borehole UZ-7a

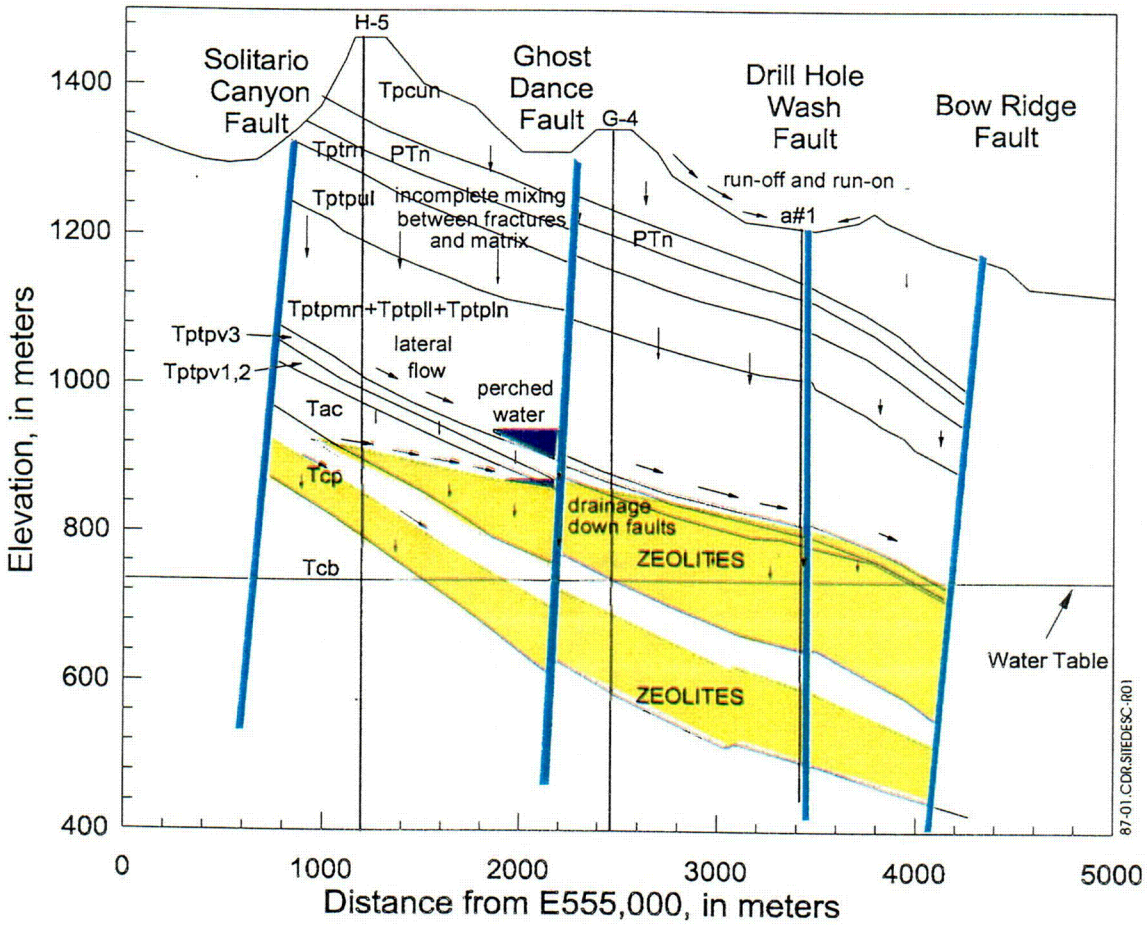

Figure 8.7-1. Aspects of Flow in the Unsaturated Zone at Yucca Mountain That Will Cause Departures from the Assumptions of the Chloride Mass-Balance Method

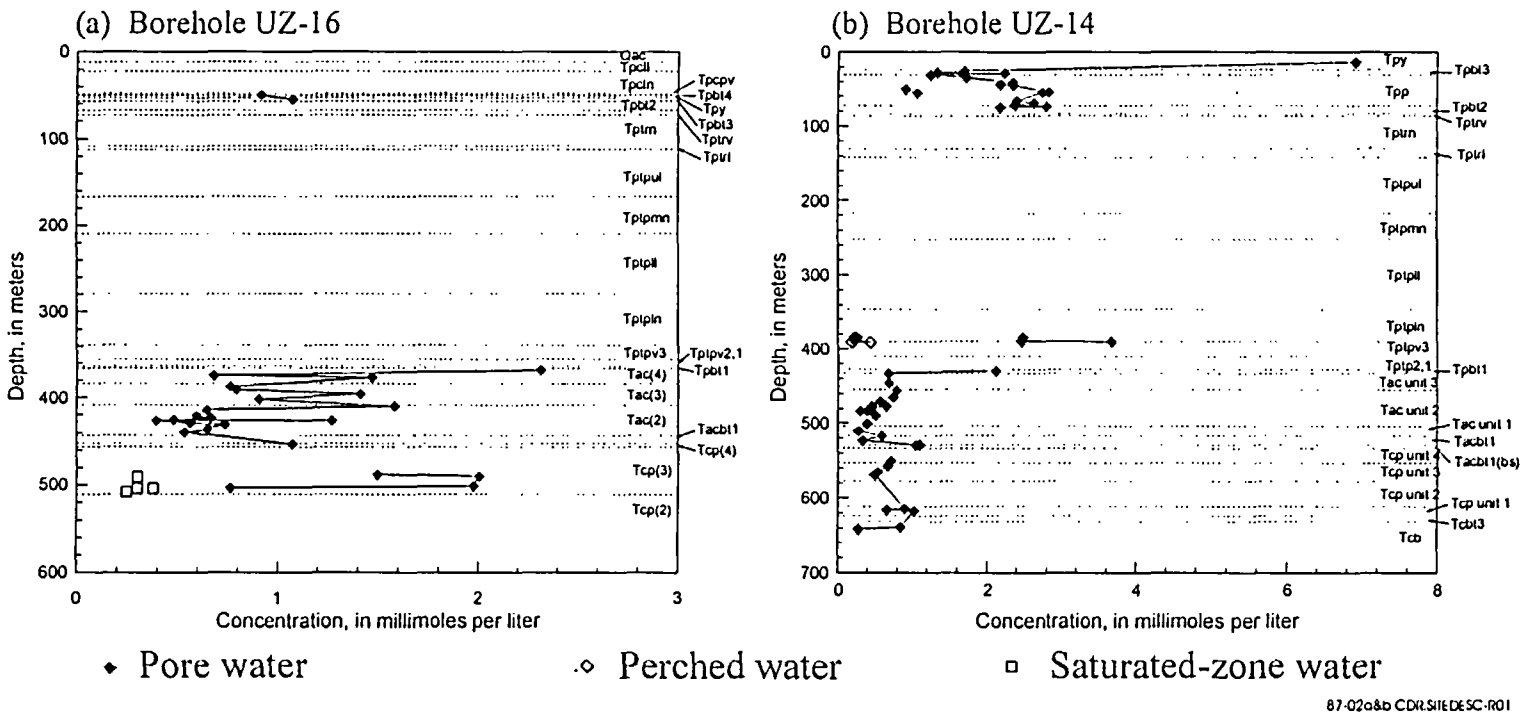

Sources: Yang et al. (1996, Tables 2, 3, 4, 5, and 6); Yang et al. (1998, Tables 2, 3, and 4)

NOTE: Solid diamonds are pore-water samples; open diamonds are perched water samples; open squares are saturated zone water samples.

Figure 8.7-2. Chloride Concentration as a Function of Depth at Various Boreholes

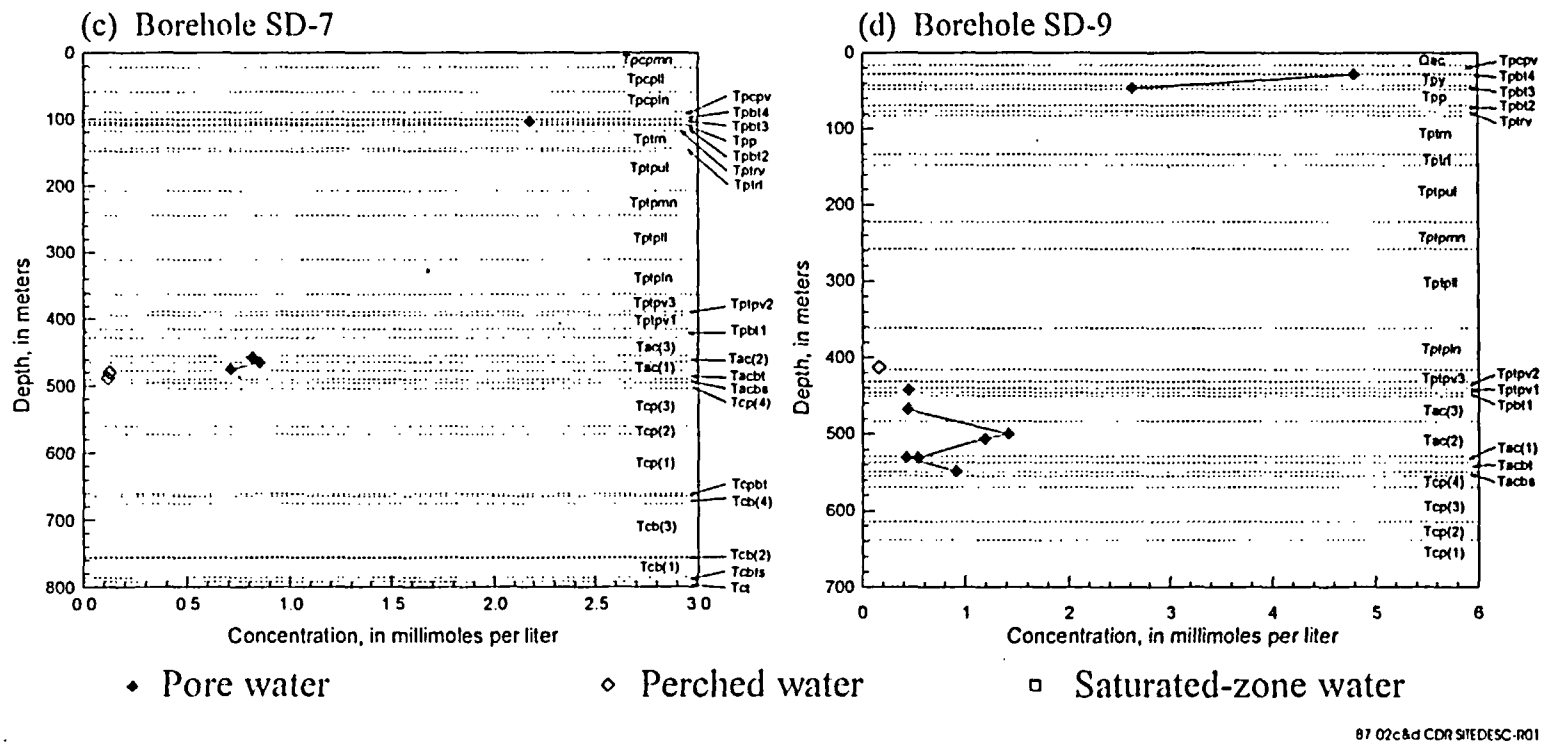

Sources: Yang et al. (1996, Tables 2, 3, 4, 5, and 6); Yang et al. (1998, Tables 2, 3, and 4)

NOTE: Solid diamonds are pore-water samples; open diamonds are perched water samples; open squares are saturated zone water samples.

Figure 8.7-2. Chloride Concentration as a Function of Depth at Various Boreholes (Continued)

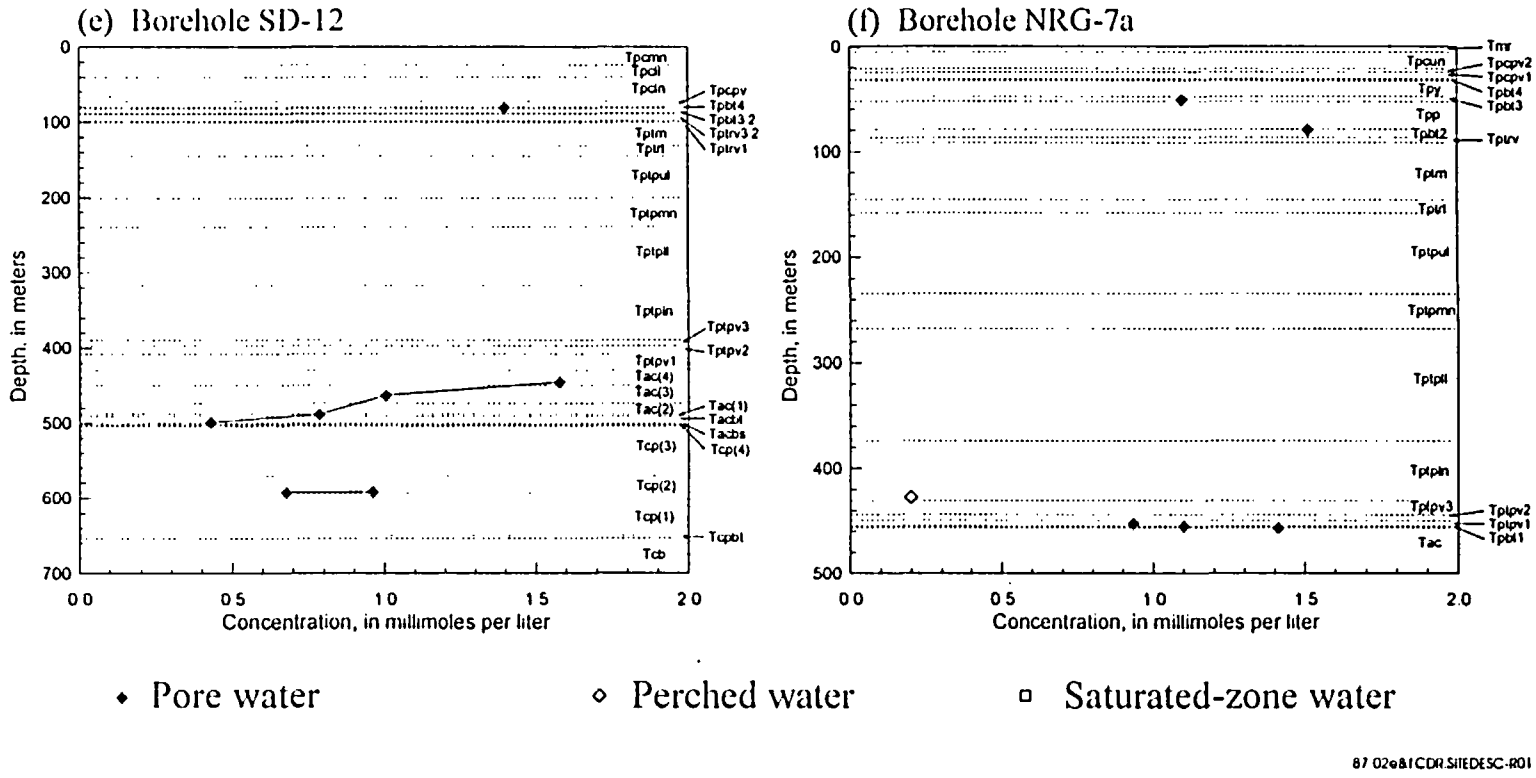

Sources: Yang et al. (1996, Tables 2, 3, 4, 5, and 6); Yang et al. (1998, Tables 2, 3, and 4)

NOTE: Solid diamonds are pore-water samples; open diamonds are perched water samples; open squares are saturated zone water samples.

Figure 8.7-2. Chloride Concentration as a Function of Depth at Various Boreholes (Continued)

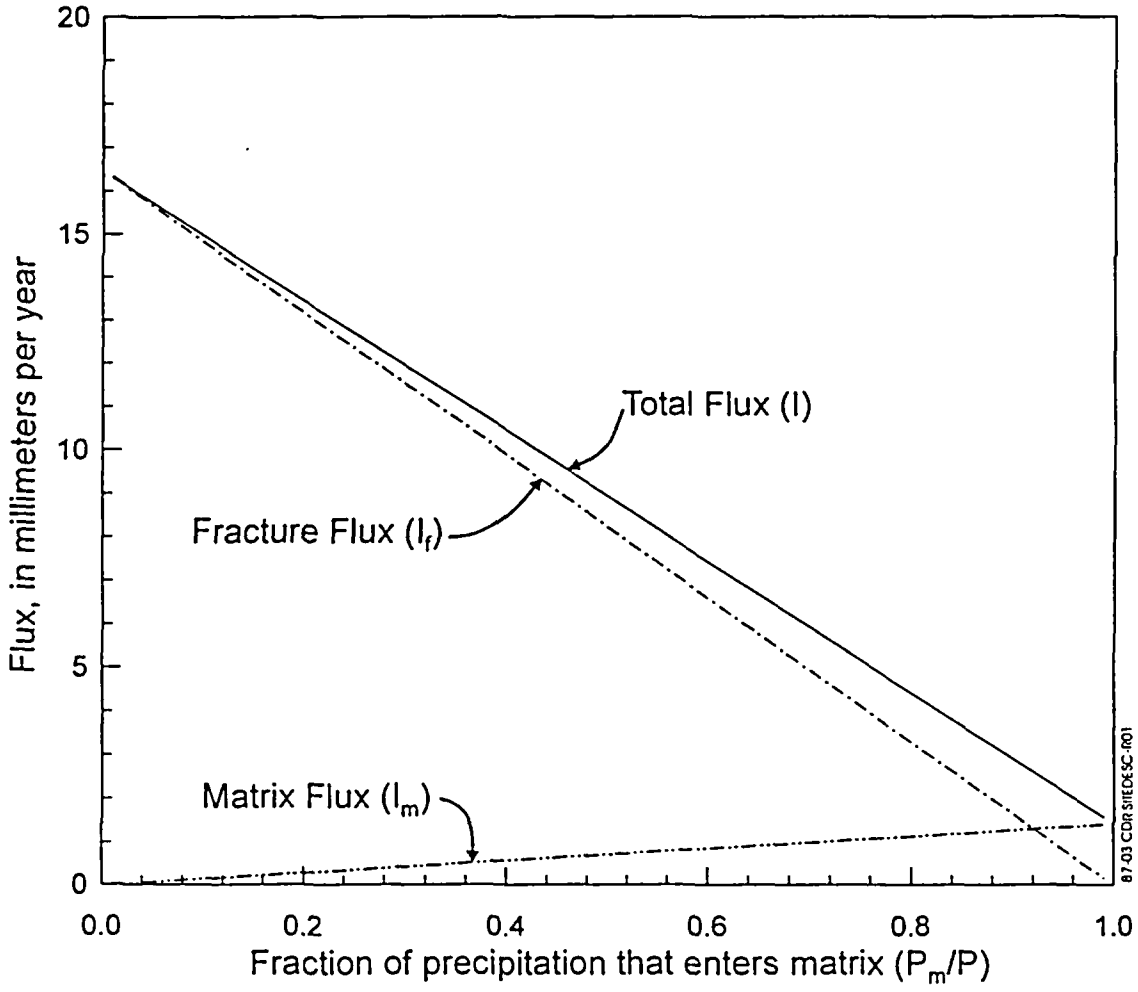

NOTE: Assumed values for C_m and C_f are 74.8 and 6.4 mg/L. This plot is based on Equation 8.7-3, as explained in the text.

Figure 8.7-3. Effects of Partitioning Precipitation between Matrix and Fractures on Total Flux, Fracture Flux, and Matrix Flux in a Poorly Mixed Fracture-Matrix System

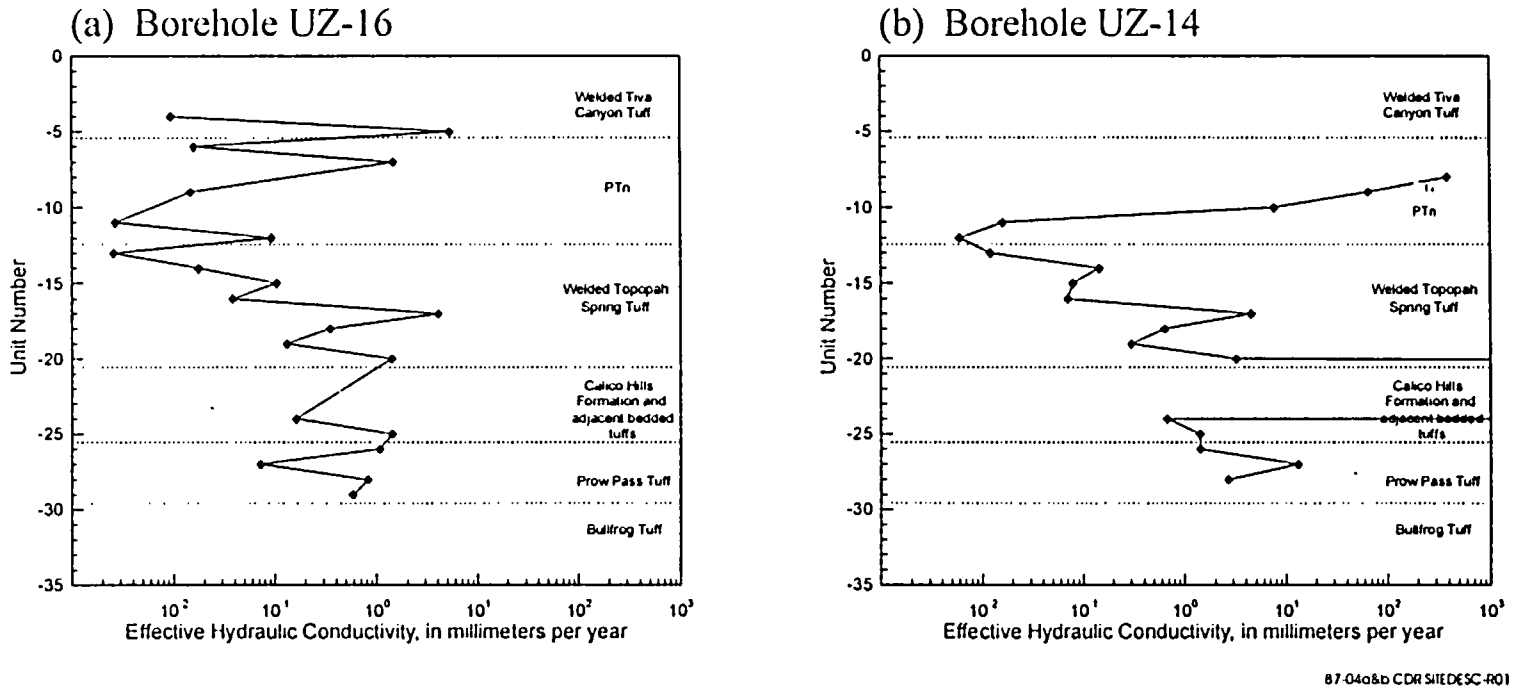

DTN: GS960908312231.004

Figure 8.7-4. Effective Hydraulic Conductivities Estimated for the Hydrogeologic Units of L.E. Flint (1998) from Measured Water Saturation Data and Parameters of the van Genuchten Moisture Characteristic Function

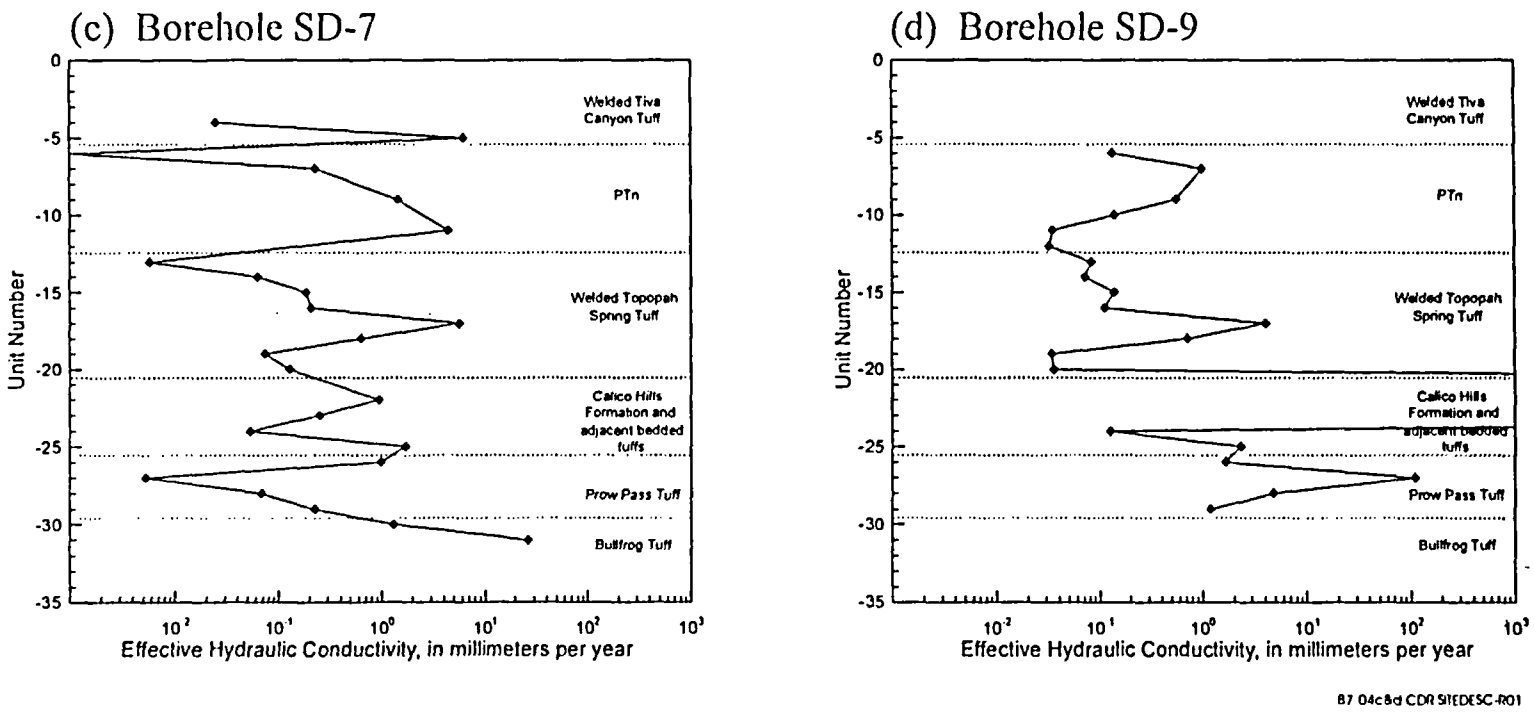

DTN: GS960908312231.004

Figure 8.7-4. Effective Hydraulic Conductivities Estimated for the Hydrogeologic Units of L.E. Flint (1998) from Measured Water Saturation Data and Parameters of the van Genuchten Moisture Characteristic Function (Continued)

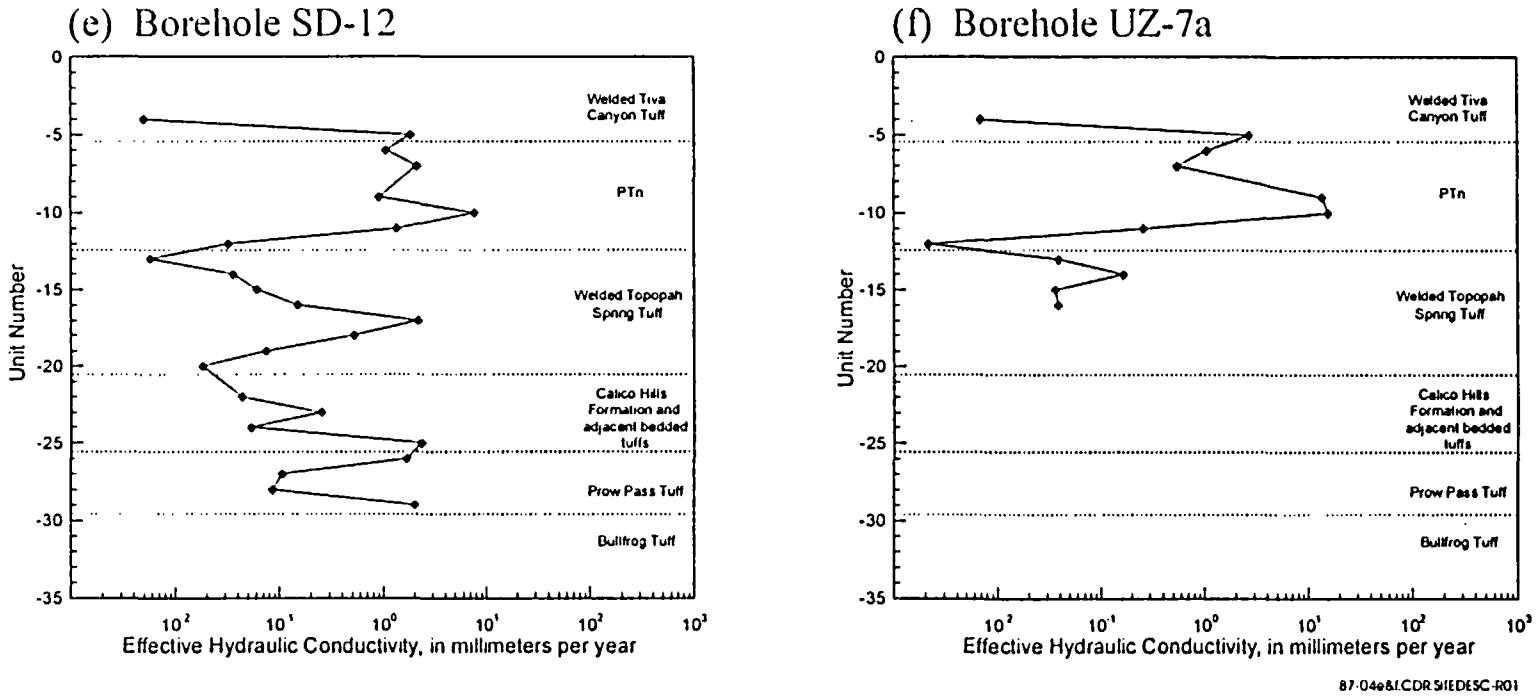

DTN: GS960908312231.004

Figure 8.7-4. Effective Hydraulic Conductivities Estimated for the Hydrogeologic Units of L.E. Flint (1998) from Measured Water Saturation Data and Parameters of the van Genuchten Moisture Characteristic Function (Continued)

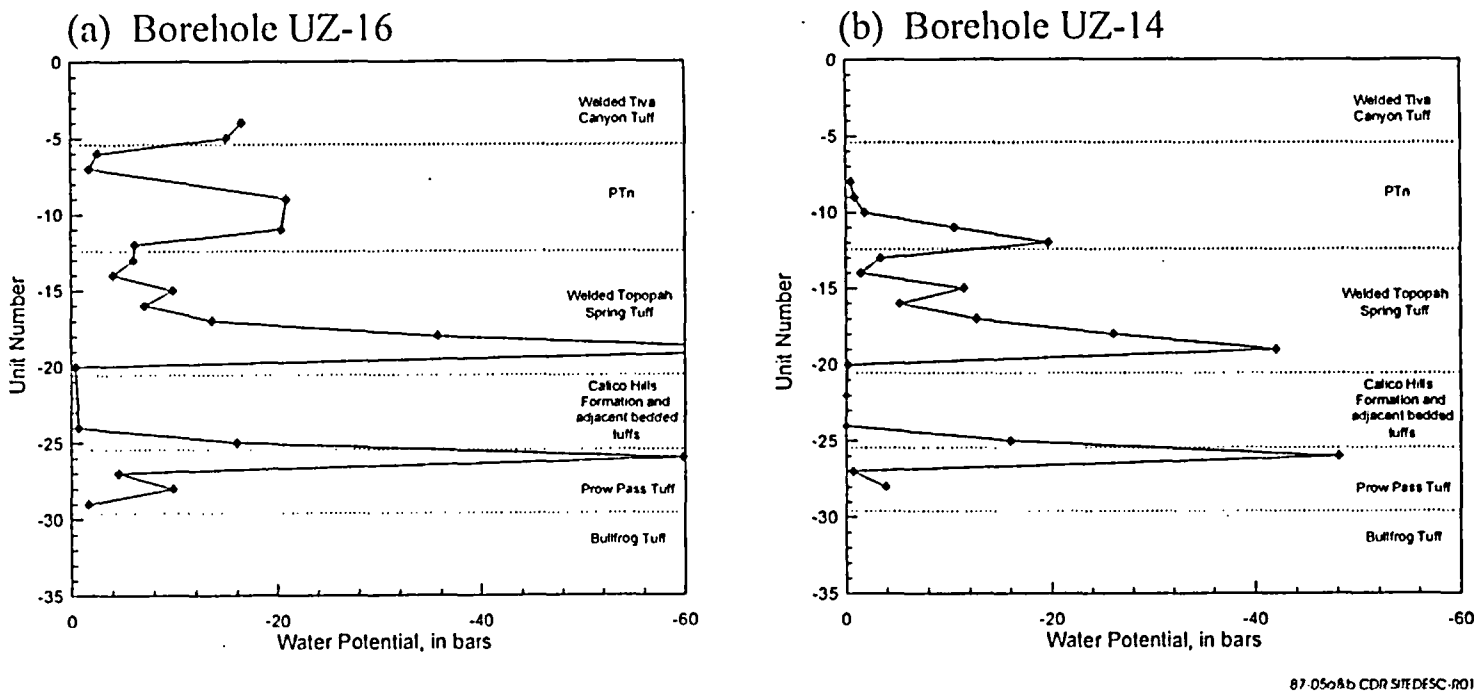

DTN: GS960908312231.004

Figure 8.7-5. Water Potentials Estimated for the Hydrogeologic Units of L.E. Flint (1998) from Measured Water Saturation Data and Parameters of the van Genuchten Moisture Characteristic Function

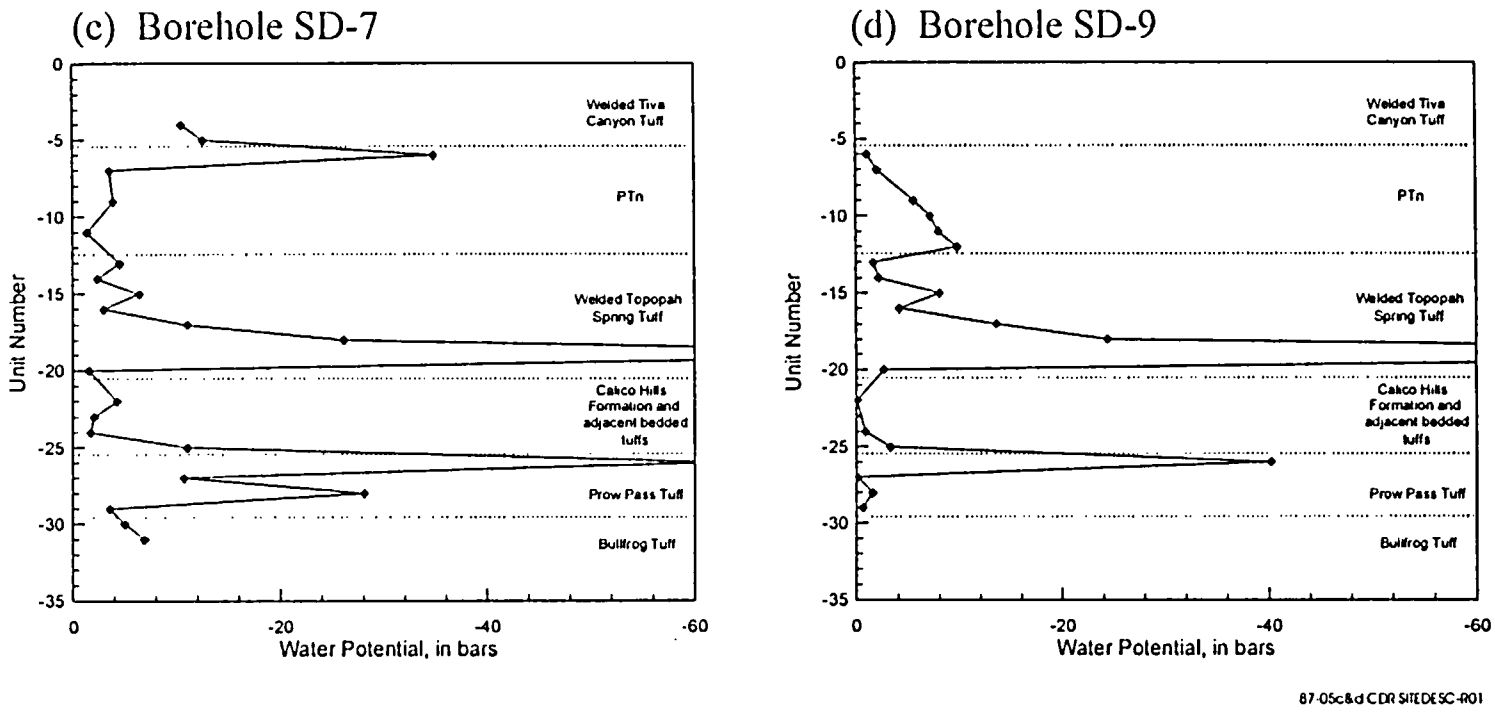

DTN: GS960908312231.004

Figure 8.7-5. Water Potentials Estimated for the Hydrogeologic Units of L.E. Flint (1998) from Measured Water Saturation Data and Parameters of the van Genuchten Moisture Characteristic Function (Continued)

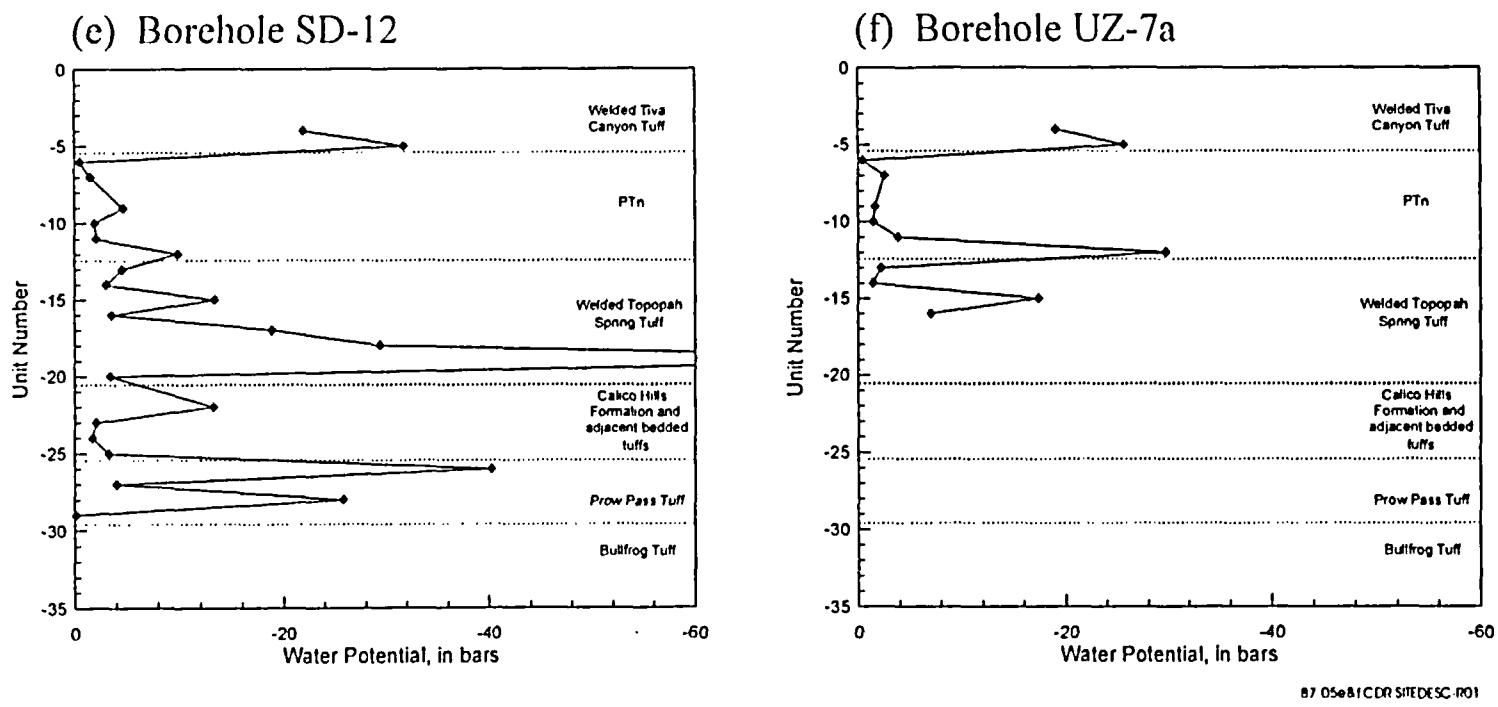

DTN: GS960908312231.004

Figure 8.7-5. Water Potentials Estimated for the Hydrogeologic Units of L.E. Flint (1998) from Measured Water Saturation Data and Parameters of the van Genuchten Moisture Characteristic Function (Continued)

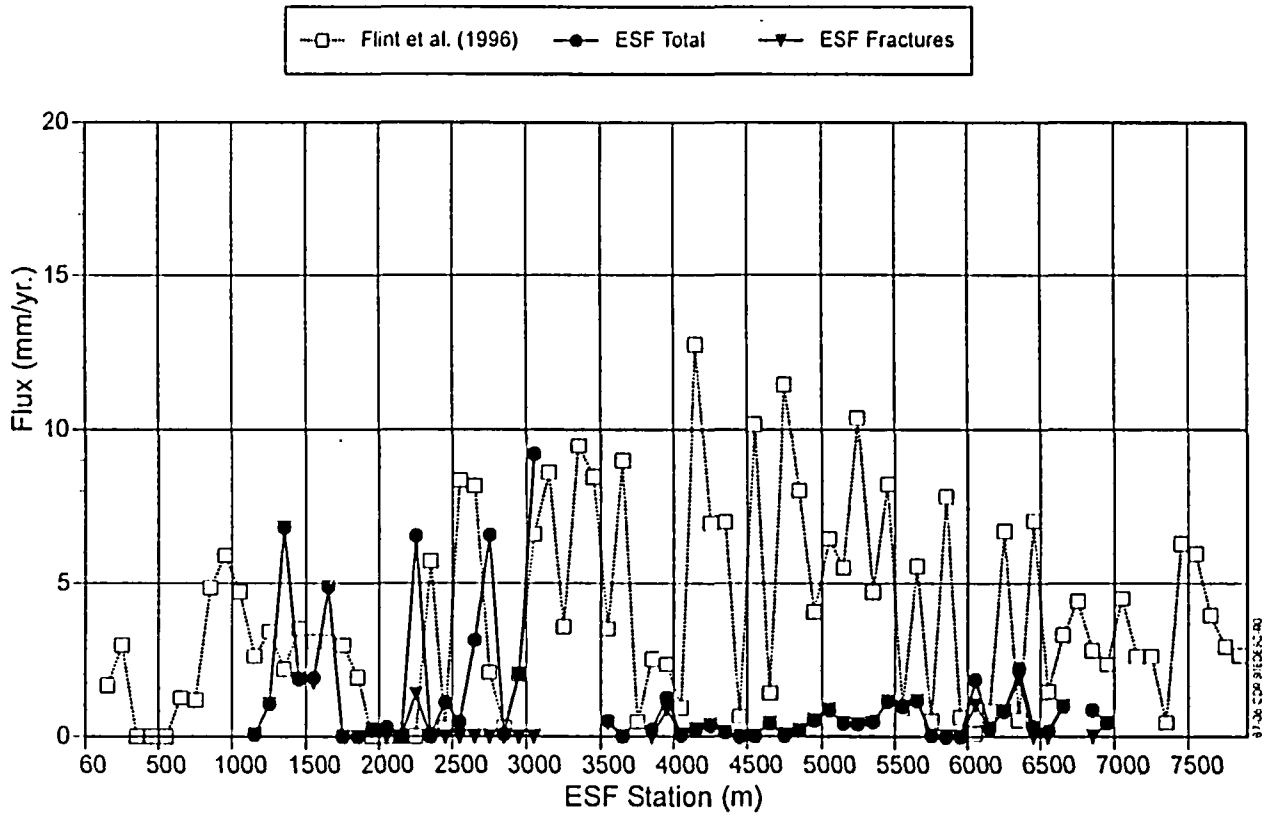

Source: Modified from Paces, Marshall et al. (1997, Figure F1)

Figure 8.7-6. Flux Estimates from Secondary Mineral Abundances (Both Total and from Fractures Only) as Compared to Infiltration Flux Estimates from Flint et al. (1996)

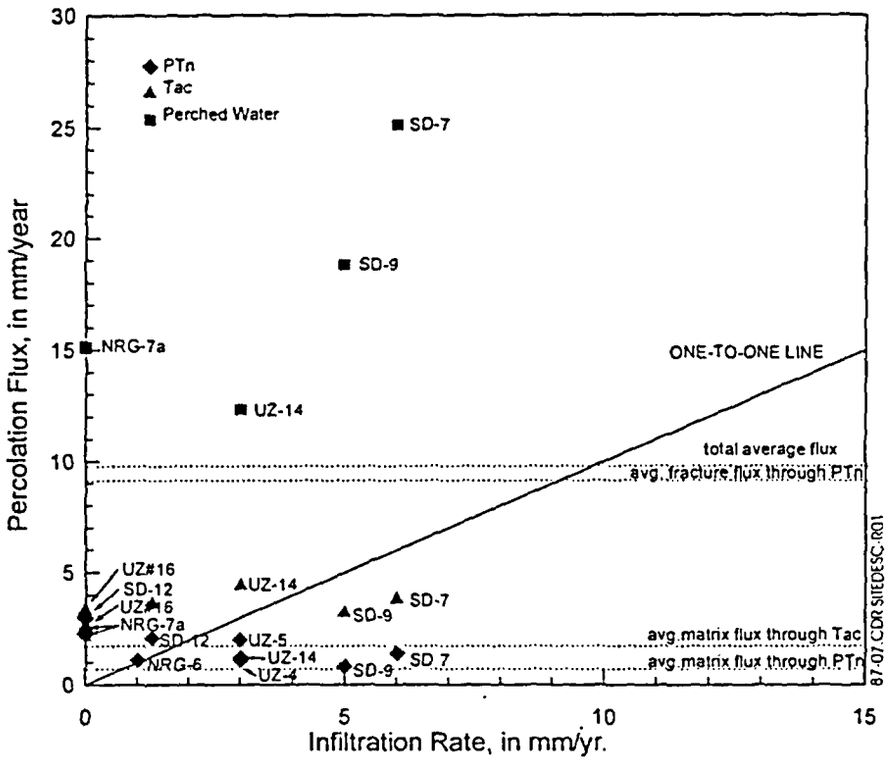

Source: Data from Table 8.7-7

Figure 8.7-7. Comparison of Percolation Flux Rates Estimated through Analyses of Borehole Chloride Data with Net Infiltration Rates from the Infiltration Model of Flint et al. (1996) for 90-Meter by 90-Meter Areas around Borehole Locations

INTENTIONALLY LEFT BLANK

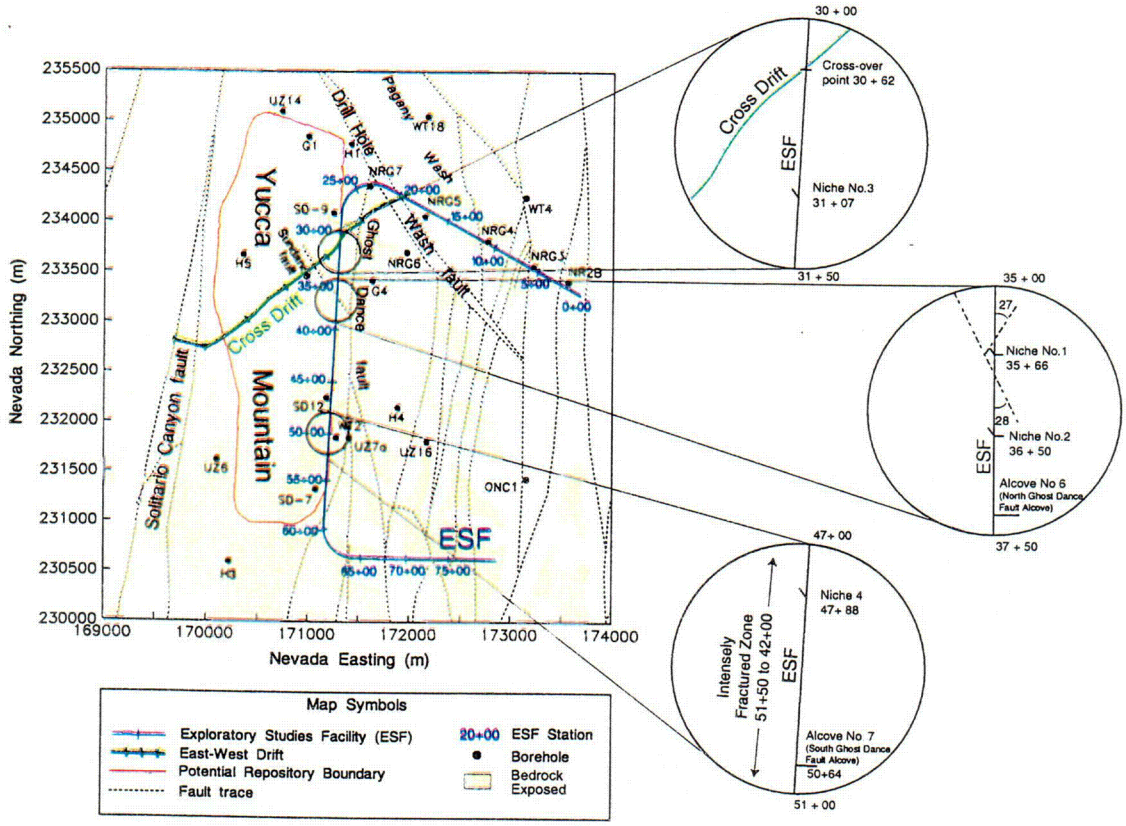

Source: CRWMS M&O (2000a, Figure 6)

Figure 8.8-1. Schematic Diagram of the Exploratory Studies Facility Showing the Locations of the Enhanced Characterization of the Repository Block Cross Drift and the Main Drift Niches

C059

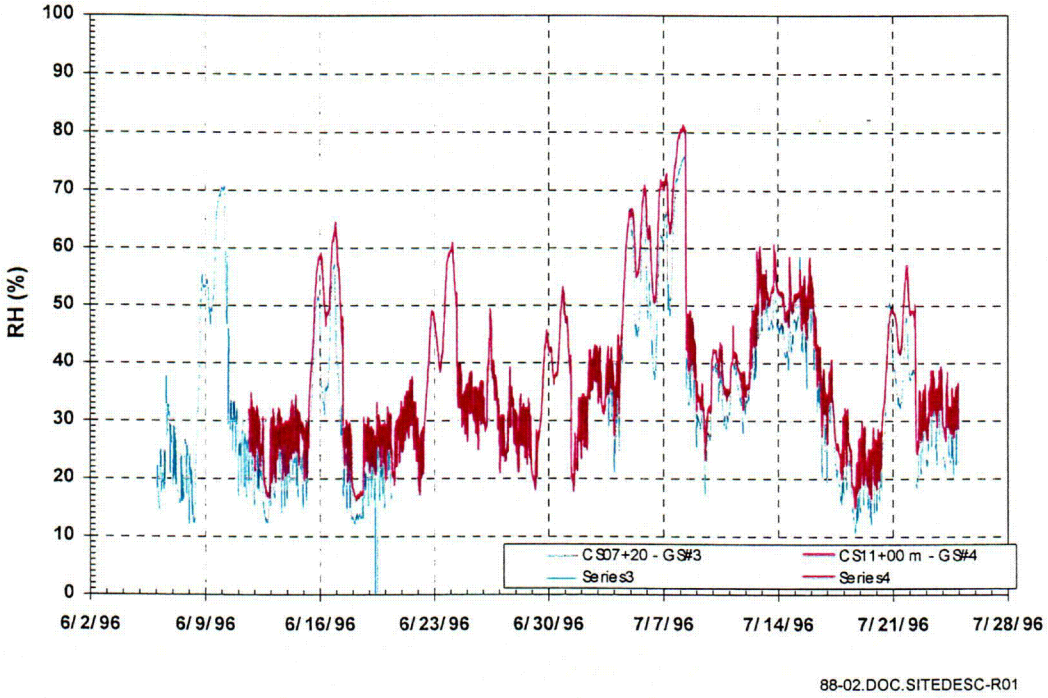

Source: Wang et al. (1996, Figure 3.4.1)

Figure 8.8-2. Relative Humidity at Exploratory Studies Facility Stations CS 07+20 m and CS 11+100 m at the Top and the Base of the Paintbrush Nonwelded Tuff, Respectively, between Alcove 3 and Alcove 4 in the Exploratory Studies Facility North Ramp

C060

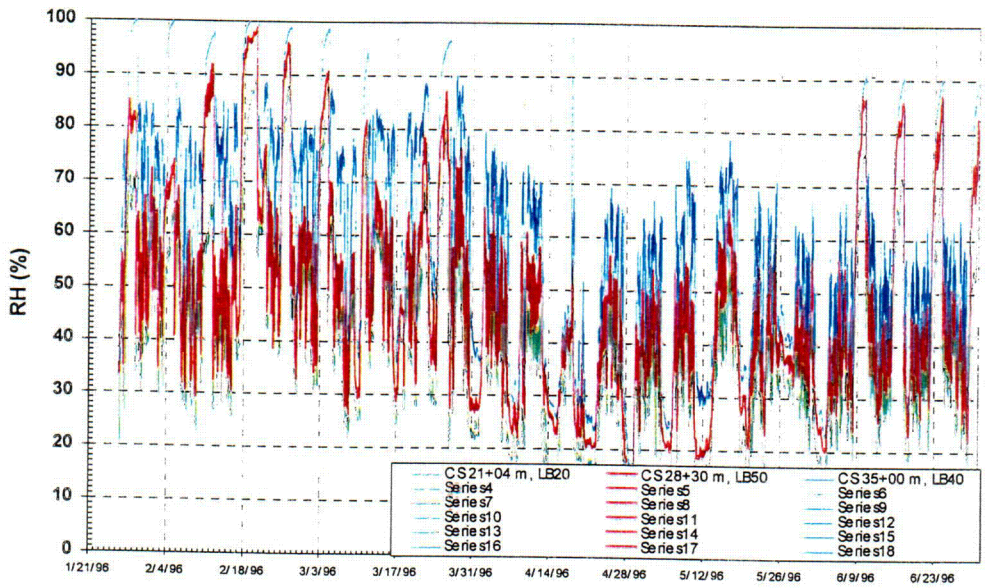

88-03.DOC.SITEDESC-R01

Source: Wang et al. (1996, Figure 3.2.1)

Figure 8.8-3. Relative Humidity at Exploratory Studies Facility Stations CS 21+0 m, CS 28+30 m, and CS 35+00 m in the Topopah Spring Welded Tuff Close to the Thermal Test Alcove in the Exploratory Studies Facility Main Drift

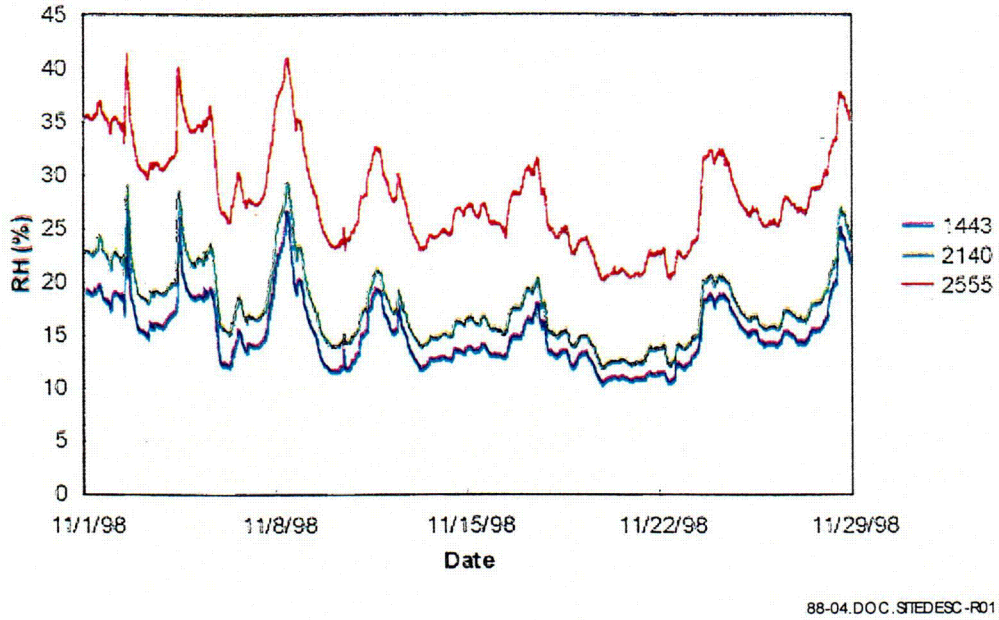

Source: CRWMS M&O (2000a, Figure 74)

Figure 8.8-4. Temporal Variations in Relative Humidity in the Exploratory Studies Facility Cross Drift

C062

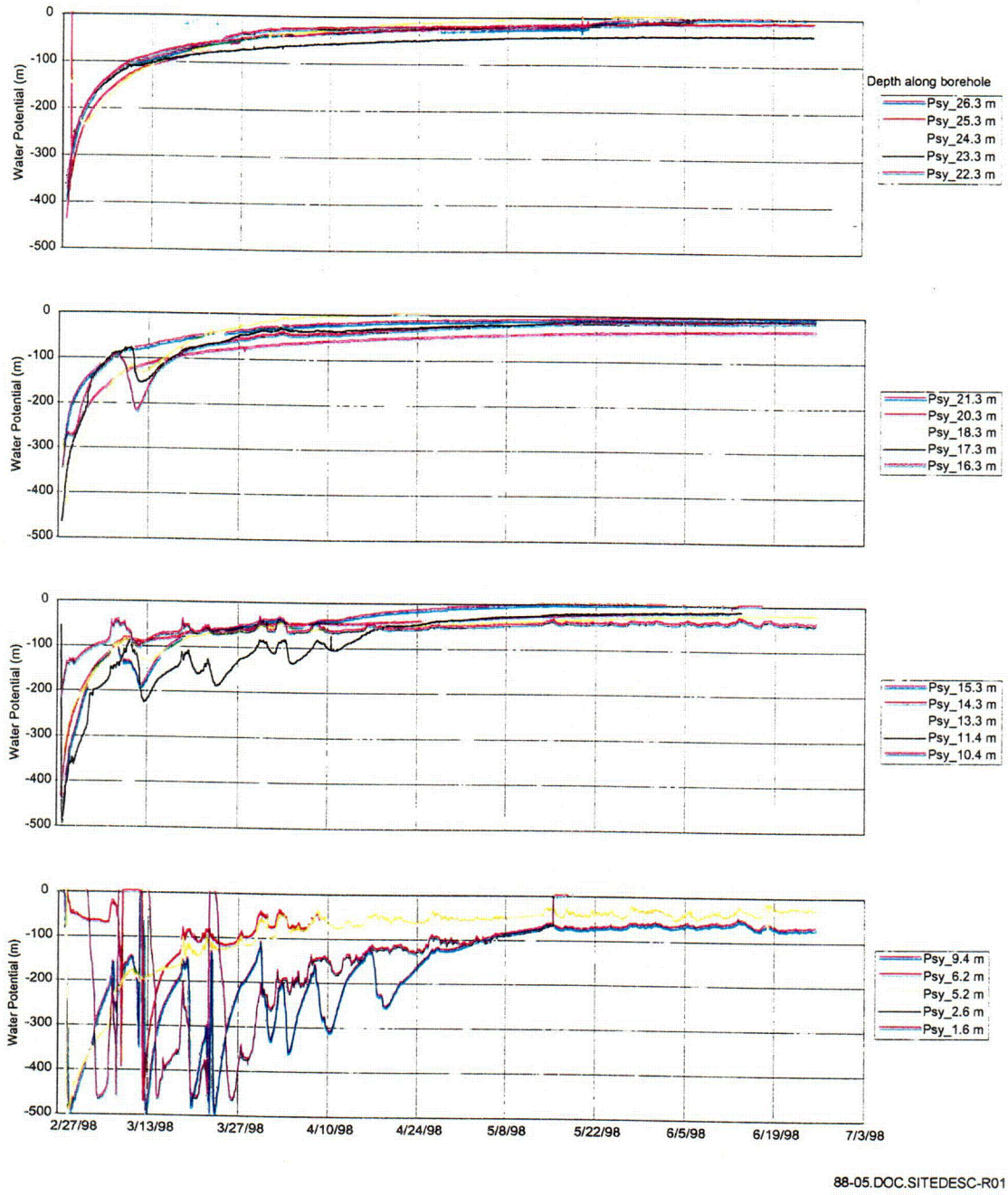

Source: CRWMS M&O (2000a, Figure 70)

Figure 8.8-5. Changes in Water Potential Observed along the Wetting-Front Monitoring Borehole at the Enhanced Characterization of the Repository Block Cross Drift Starter Tunnel

C063

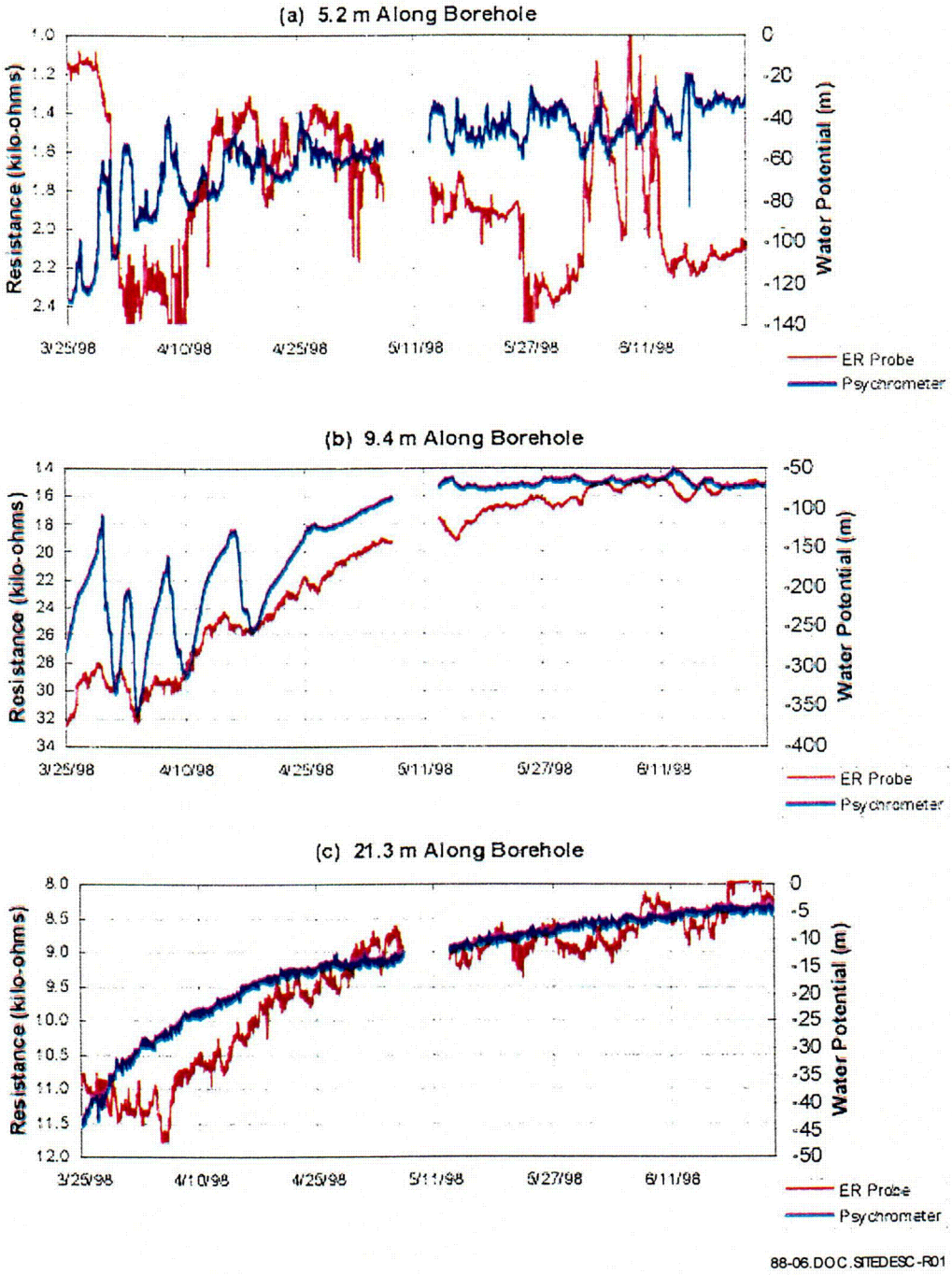

Source: CRWMS M&O (2000a, Figure 72)

Figure 8.8-6. Changes in Water Potential and Wetting-Front Position below the Cross Drift Starter Tunnel Measured Using Psychrometers and Electrical Resistivity Probes

C064

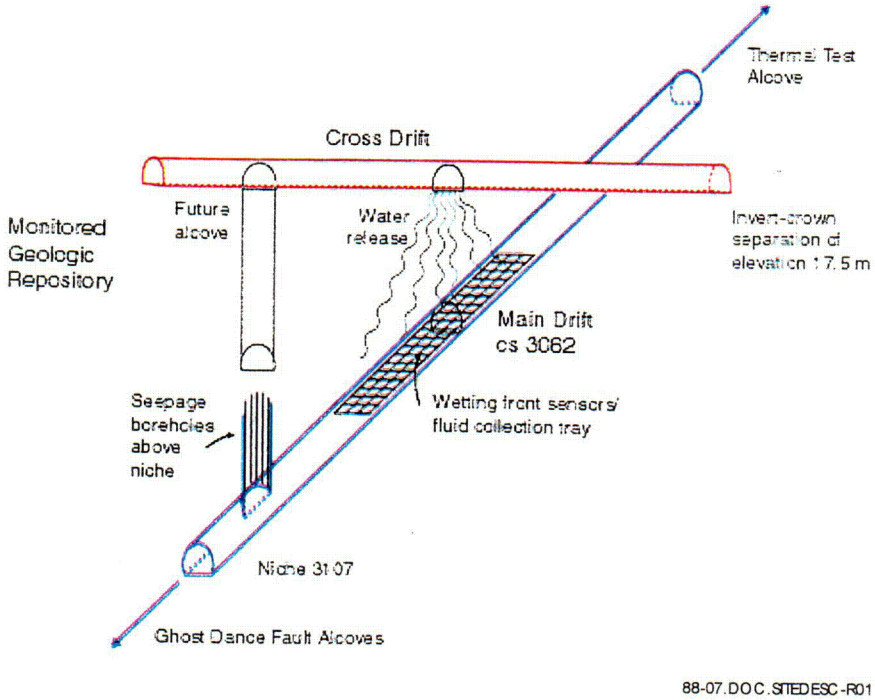

Source: CRWMS M&O (2000a, Figure 5)

Figure 8.8-7. Schematic Diagram of the Exploratory Studies Facility Main Drift-Cross Drift Crossover Point

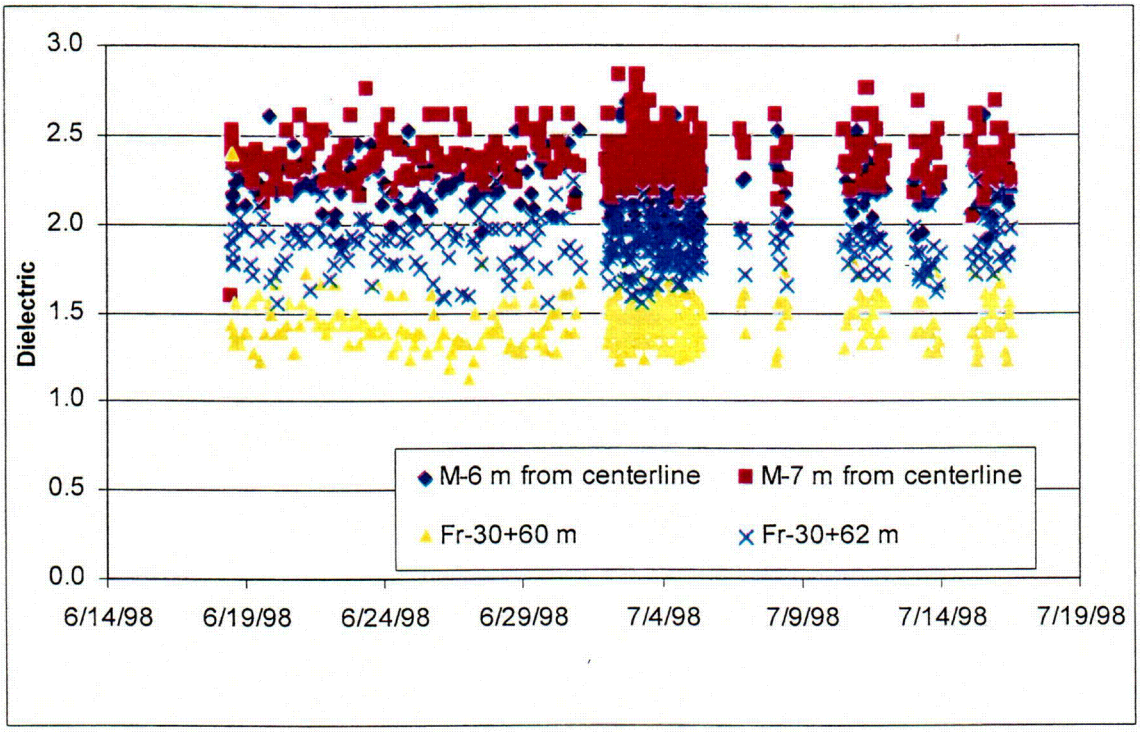

88-08.DOC.SITEDESC-R01

Source: CRWMS M&O (2000a, Figure 73)

Figure 8.8-8. Example of Data from Time-Domain-Reflectometry Probes at the Exploratory Studies Facility Main Drift-Cross Drift Crossover Location

C066

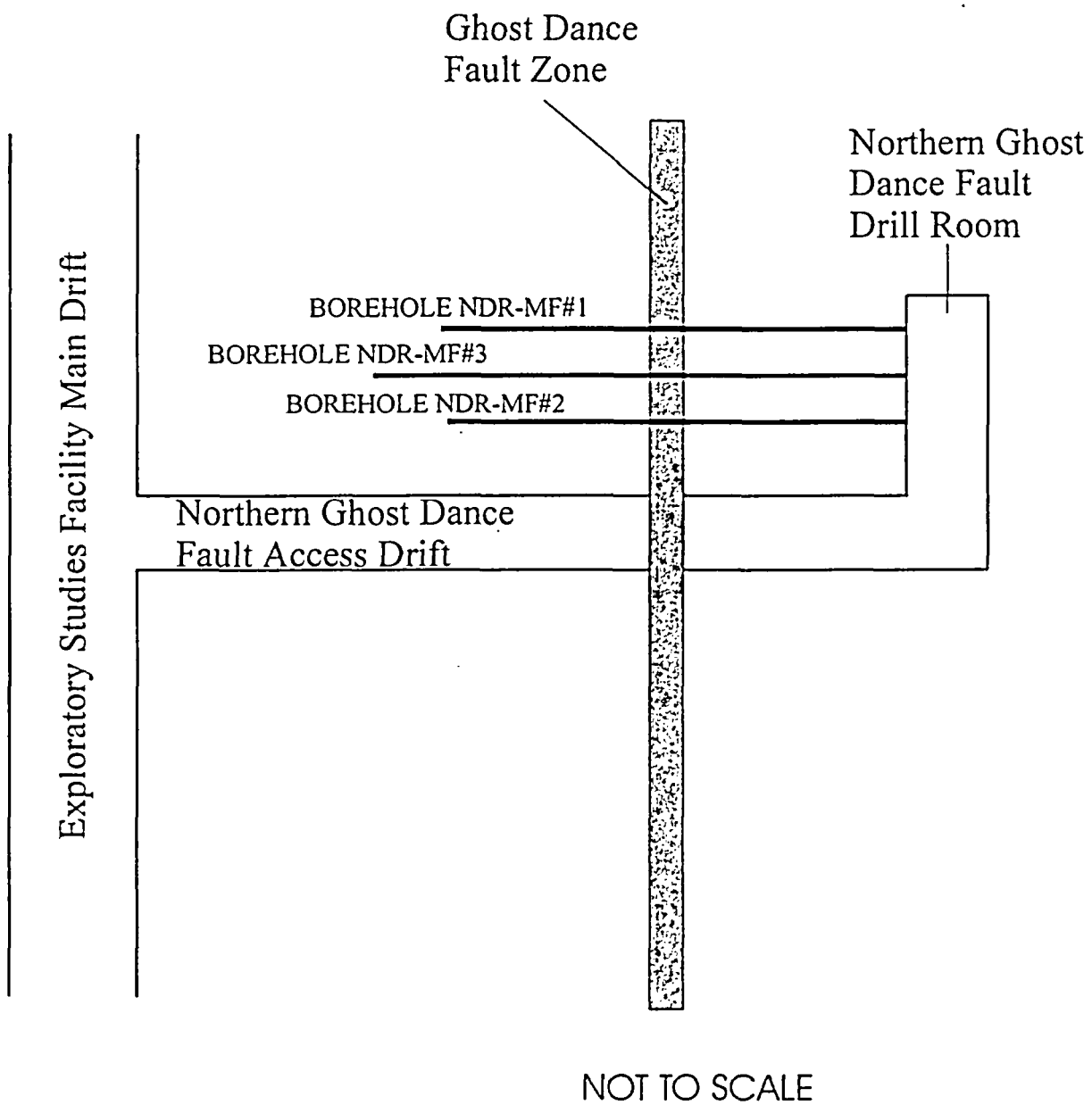

Source: LeCain, G.D. et al. (2000, Figure 3)

Figure 8.8-9. Schematic Diagram of the Northern Ghost Dance Fault Alcove and Test Boreholes

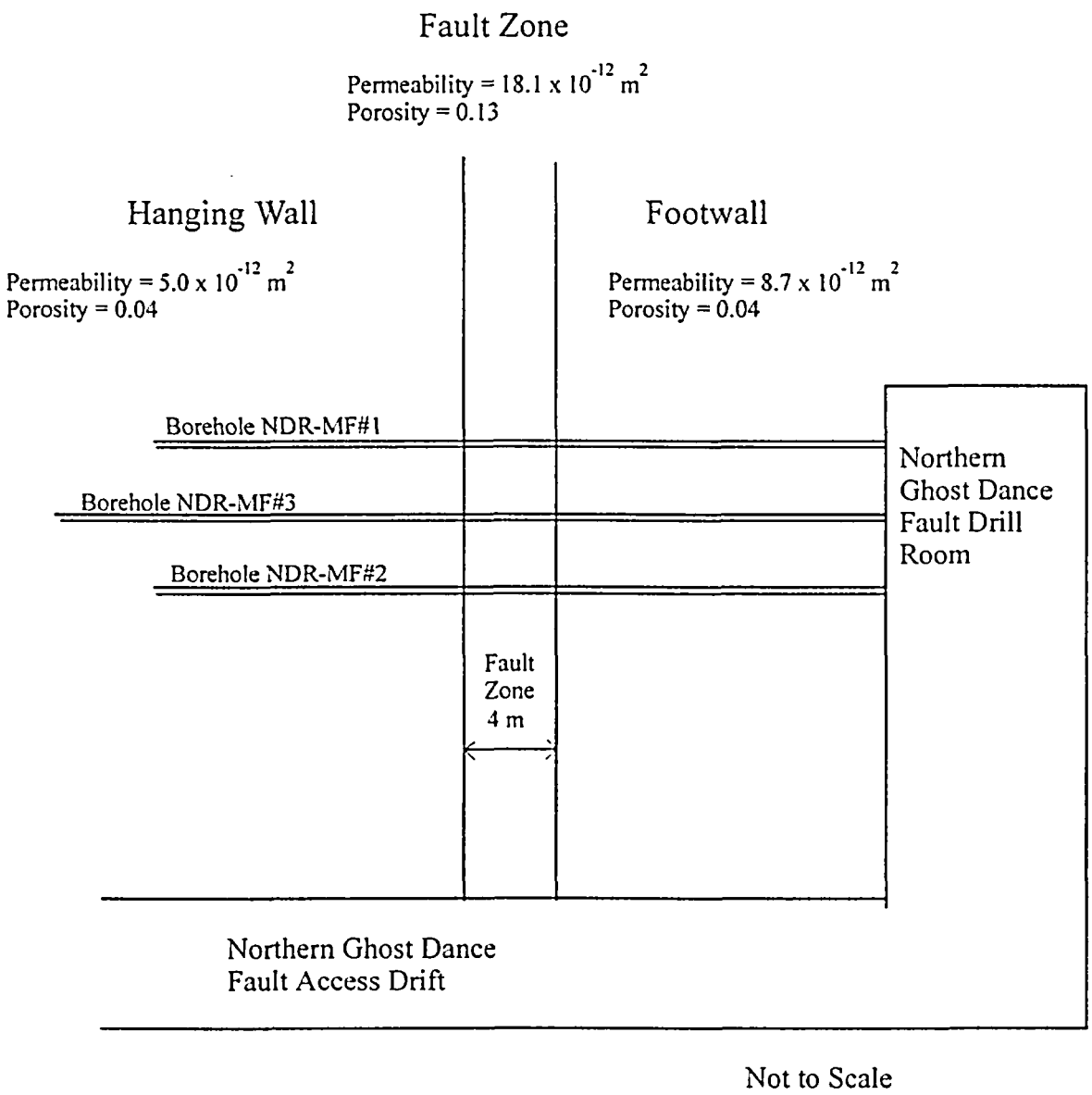

Source: Data from LeCain et al. (2000, Tables 13 and 14)

Figure 8.8-10. Schematic Overhead Diagram Showing the AIR3D Numerical-Modeling Permeability and Porosity Values of the Ghost Dance Fault Hanging Wall, Fault Zone, and Footwall

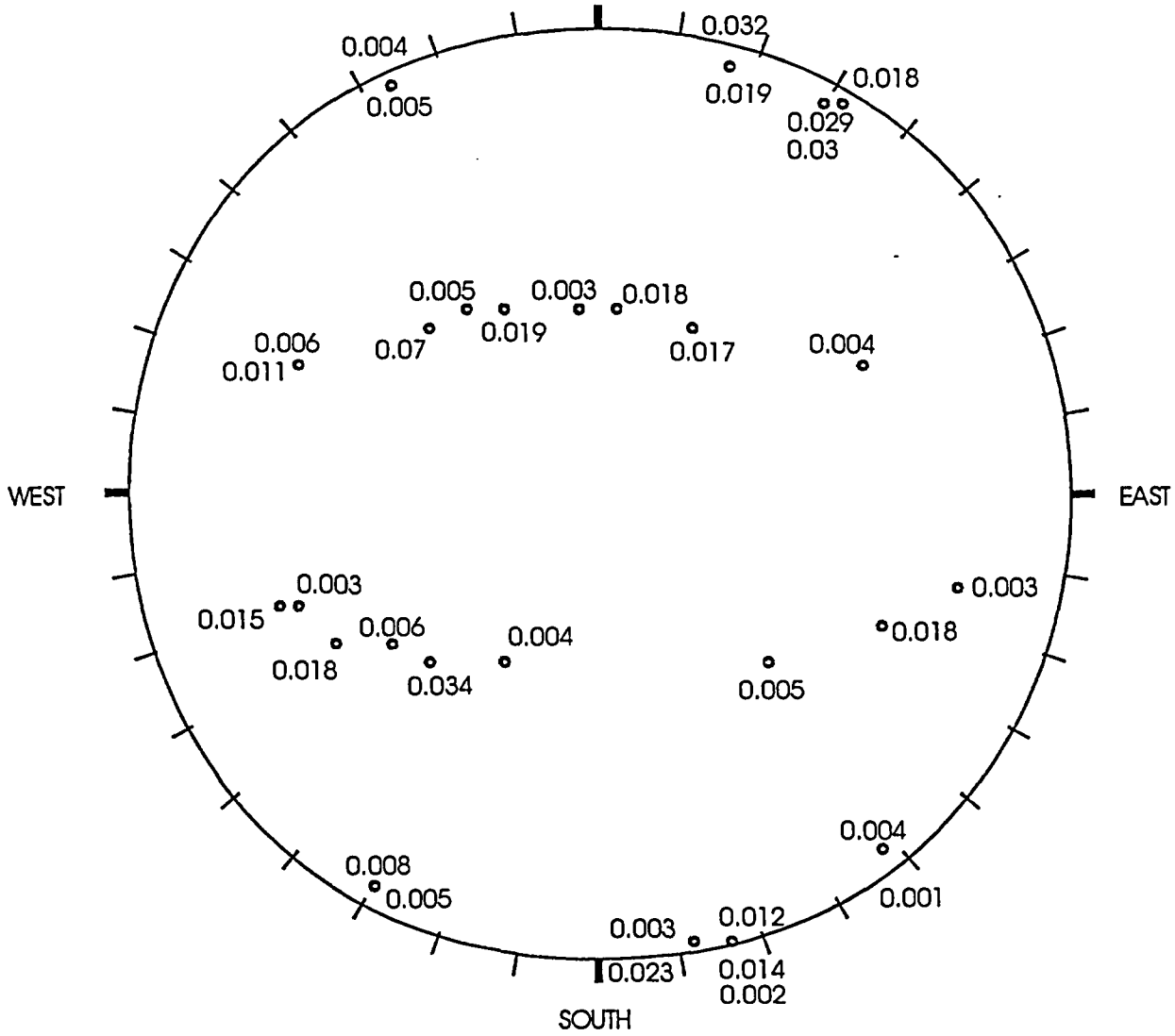

Source: LeCain, G.D. et al. (2000, Figure 18)

Figure 8.8-11. Lower-Hemisphere, Stereonet Plot of Transport Porosity Values and the Three-Dimensional Orientation, by Bearing and Plunge, of the Associated Tracer Tests

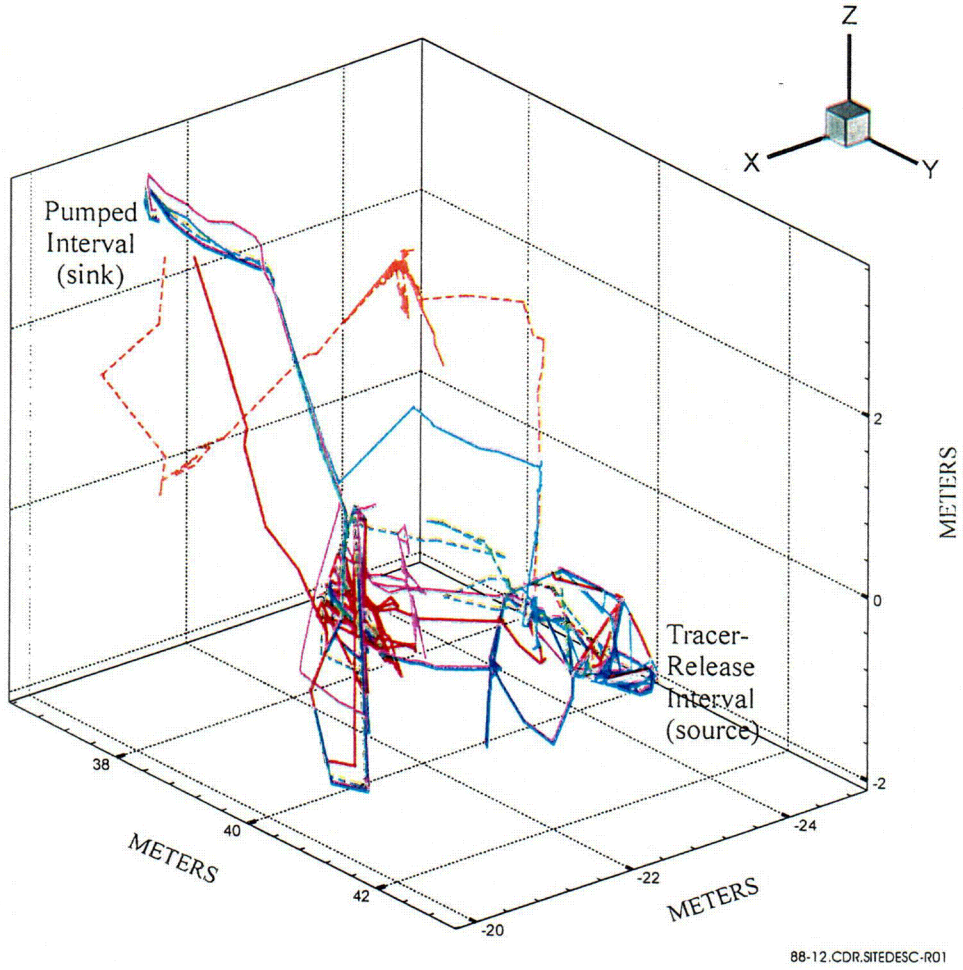

Source: Modified from LeCain, G.D. et al. (2000, Figure 23)

Figure 8.8-12. Diagram Showing Particle Paths Predicted by the Discrete-Feature Model for Six Particles

C067

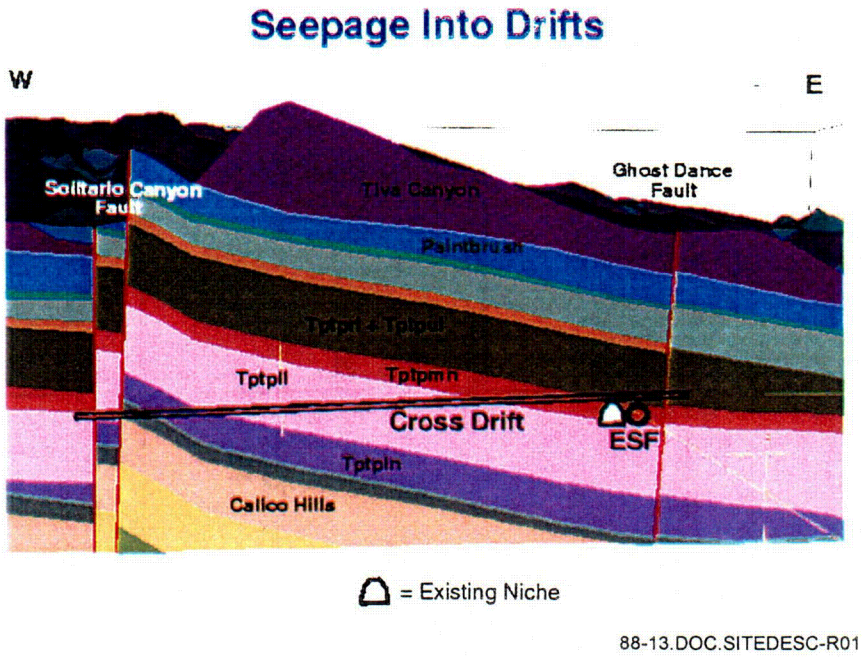

Source: CRWMS M&O (2000a, Figure 3)

Figure 8.8-13. Schematic Illustration of Stratigraphic Units Penetrated by the Cross Drift at the Potential Repository Horizon

C068

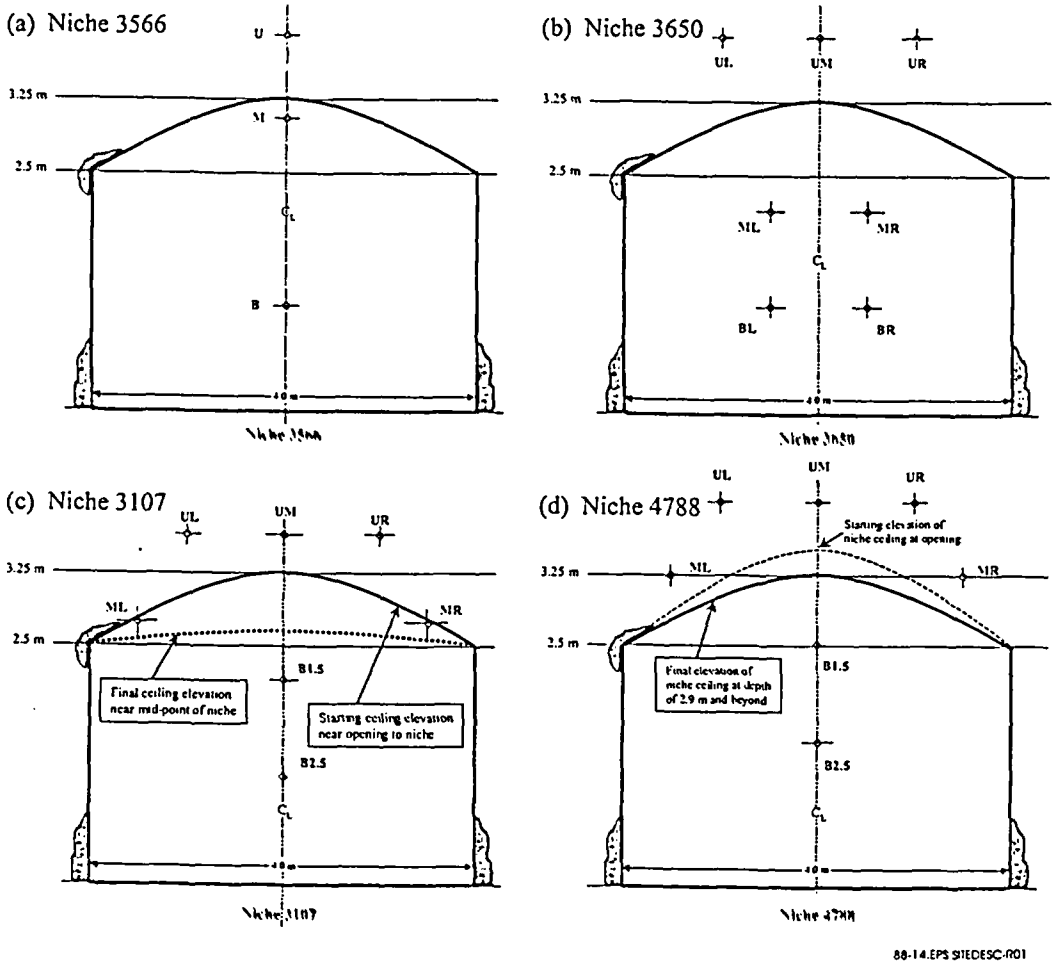

Source: CRWMS M&O (2000a, Figure 7)

Figure 8.8-14. Schematic Illustration of the End View of Borehole Clusters at Four Niches

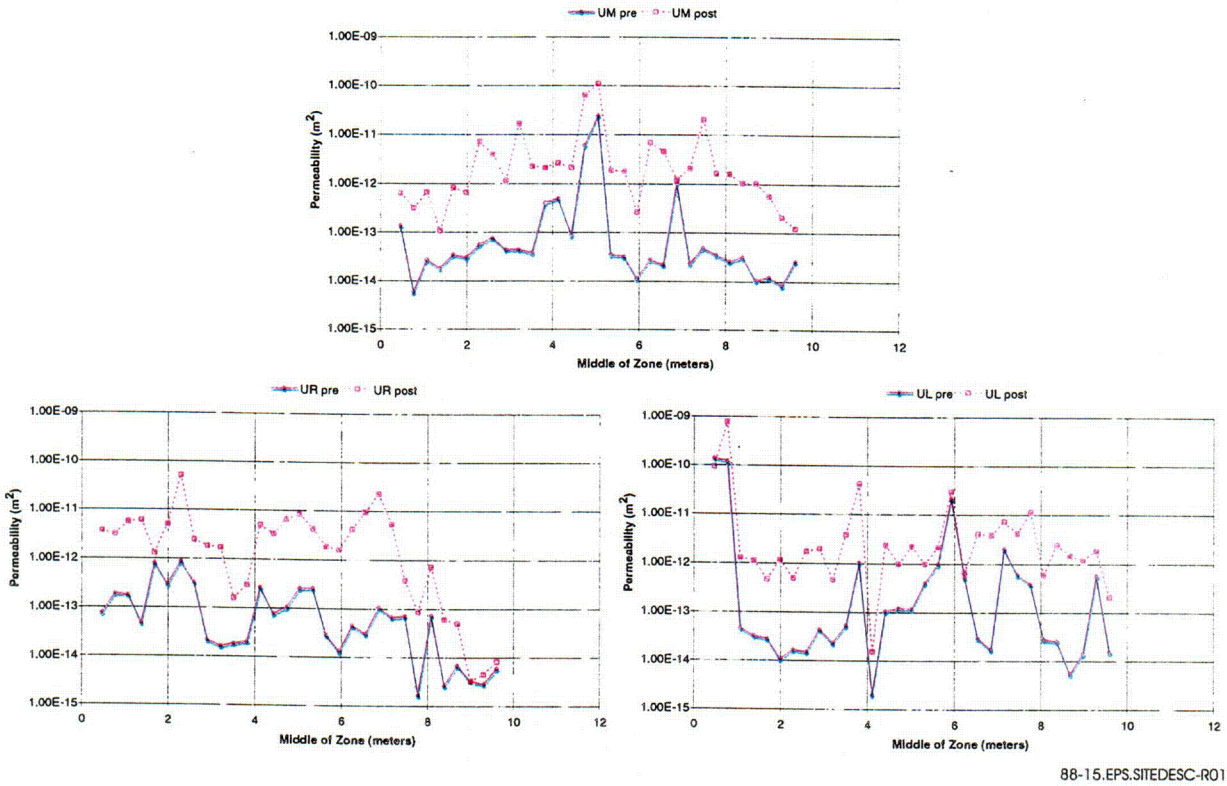

Source: CRWMS M&O (2000a, Figure 11)

Figure 8.8-15. Pre-Excavation and Post-Excavation Air Permeability Profiles along Upper Boreholes at Niche 3650

C069

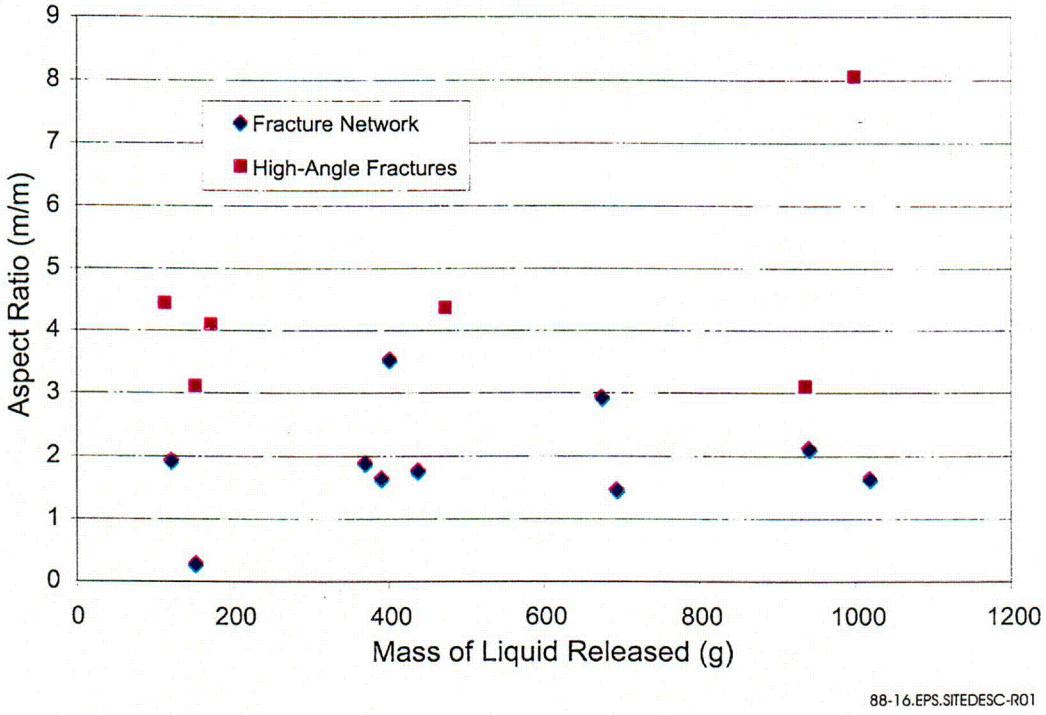

Source: CRWMS M&O (2000a, Figure 17)

Figure 8.8-16. Mass of Water Released in Niche Liquid-Release Tests versus Aspect Ratio

C069A

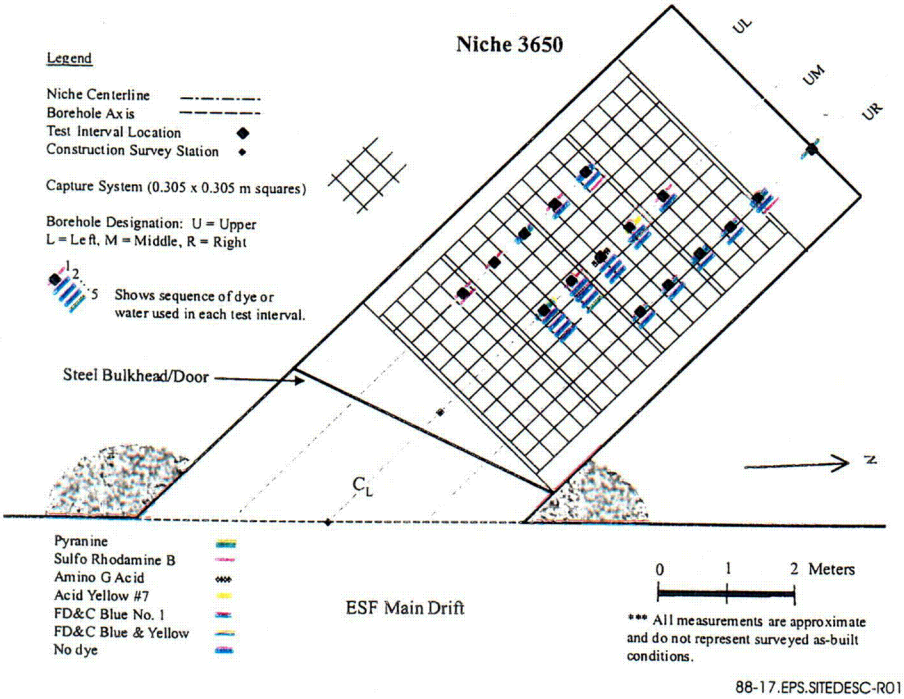

Source: CRWMS M&O (2000a, Figure 18)

Figure 8.8-17. Schematic Illustration of Seepage Capture System and Test Intervals at Niche 3650

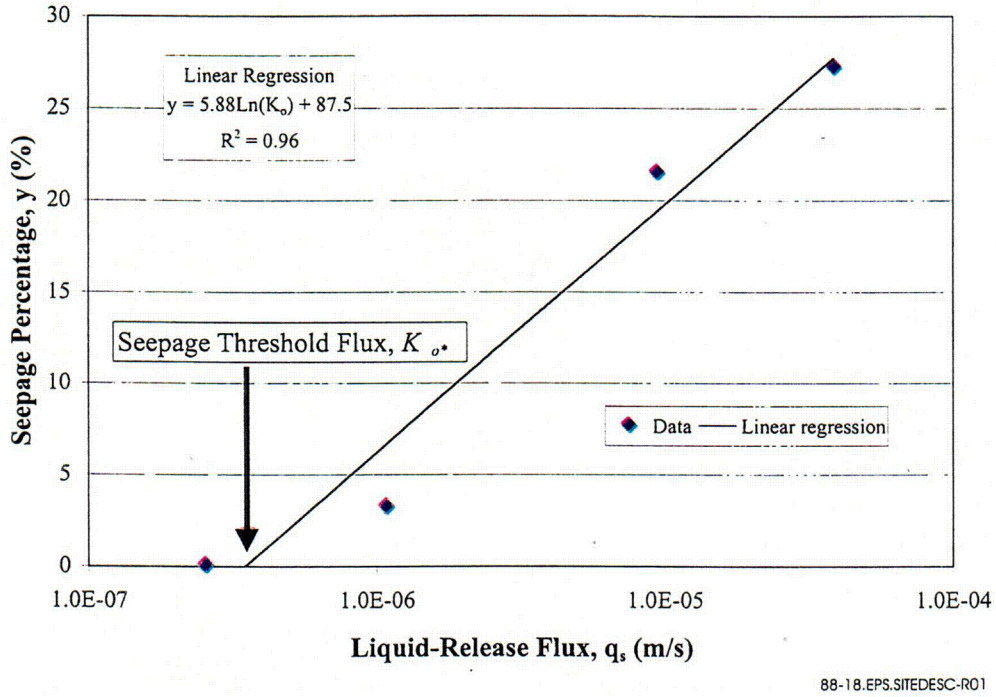

Source: CRWMS M&O (2000a, Figure 20)

Figure 8.8-18. Liquid-Release Flux versus Seepage Percentage for Seepage Tests Conducted in the 5.49-Meter to 5.79-Meter Interval of the Upper Middle Borehole at Niche 3560

C071

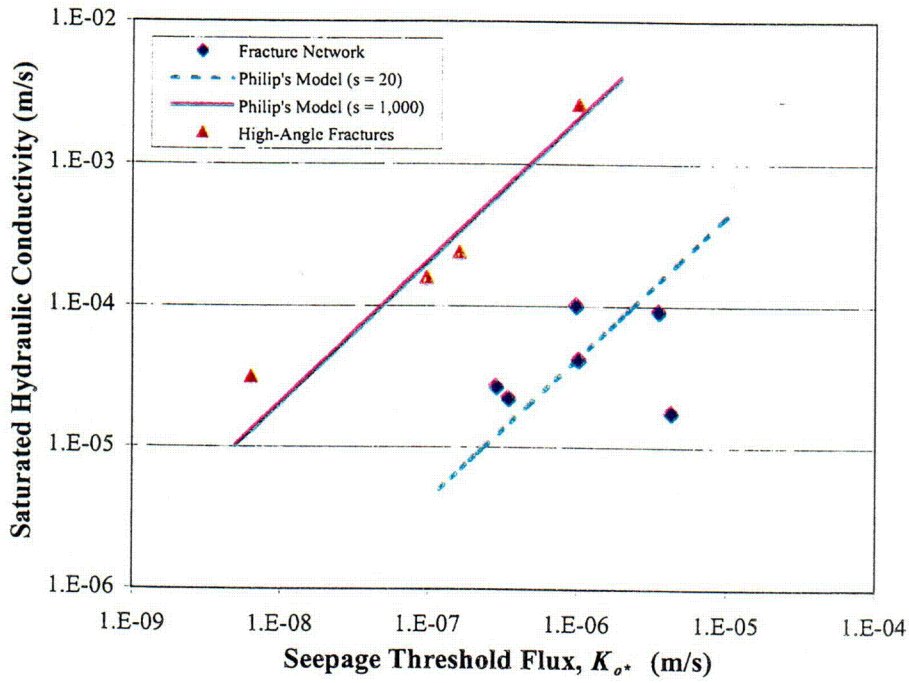

88-19.EPS.SITEDESC-R01

Source: CRWMS M&O (2000a, Figure 21)

Figure 8.8-19. Seepage Threshold Fluxes Determined from Tests Conducted in Niche 3560

C072

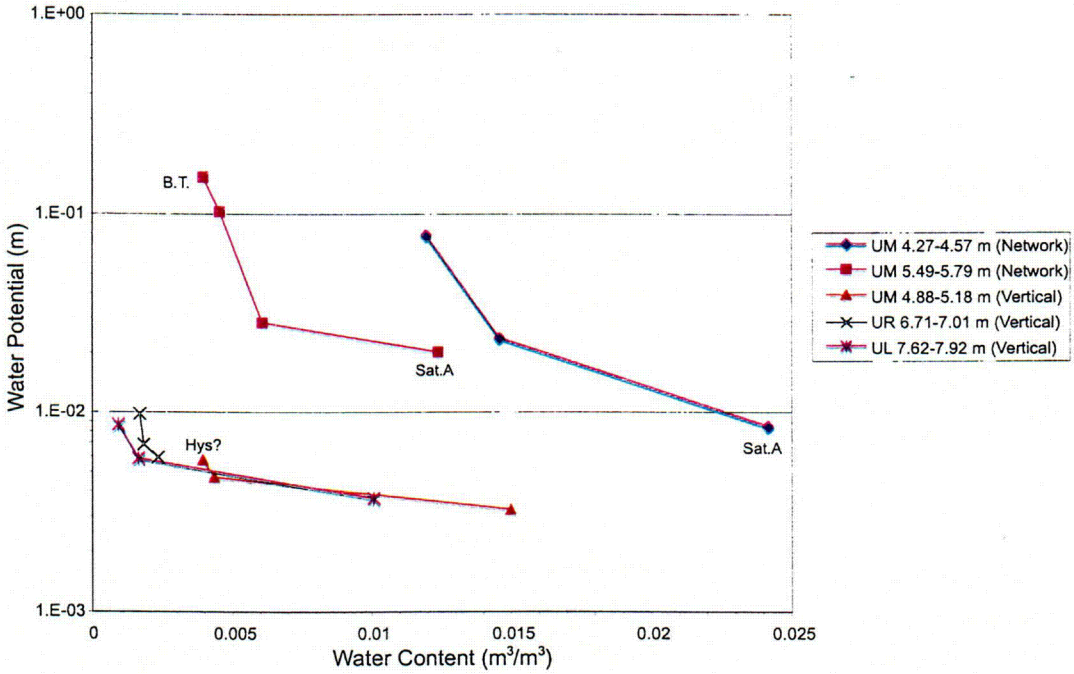

NOTE: B.T. = Data point was measured at or below the seepage threshold flux and may be influenced by the capillary barrier. Hys? = This data point may be influenced by fracture hysteresis. Sat.A = The flux was equal to or slightlly greater than the equivalent saturated hydraulic conductivity (determined using the air permeability data) for this data point.

88-20.EPS.SITEDESC-R01

Source: CRWMS M&O (2000a, Figure 22)

Figure 8.8-20. Water Retention Curves for High-Angle Fractures and Fracture Networks Derived from Seepage Tests in Niche 3650

C073

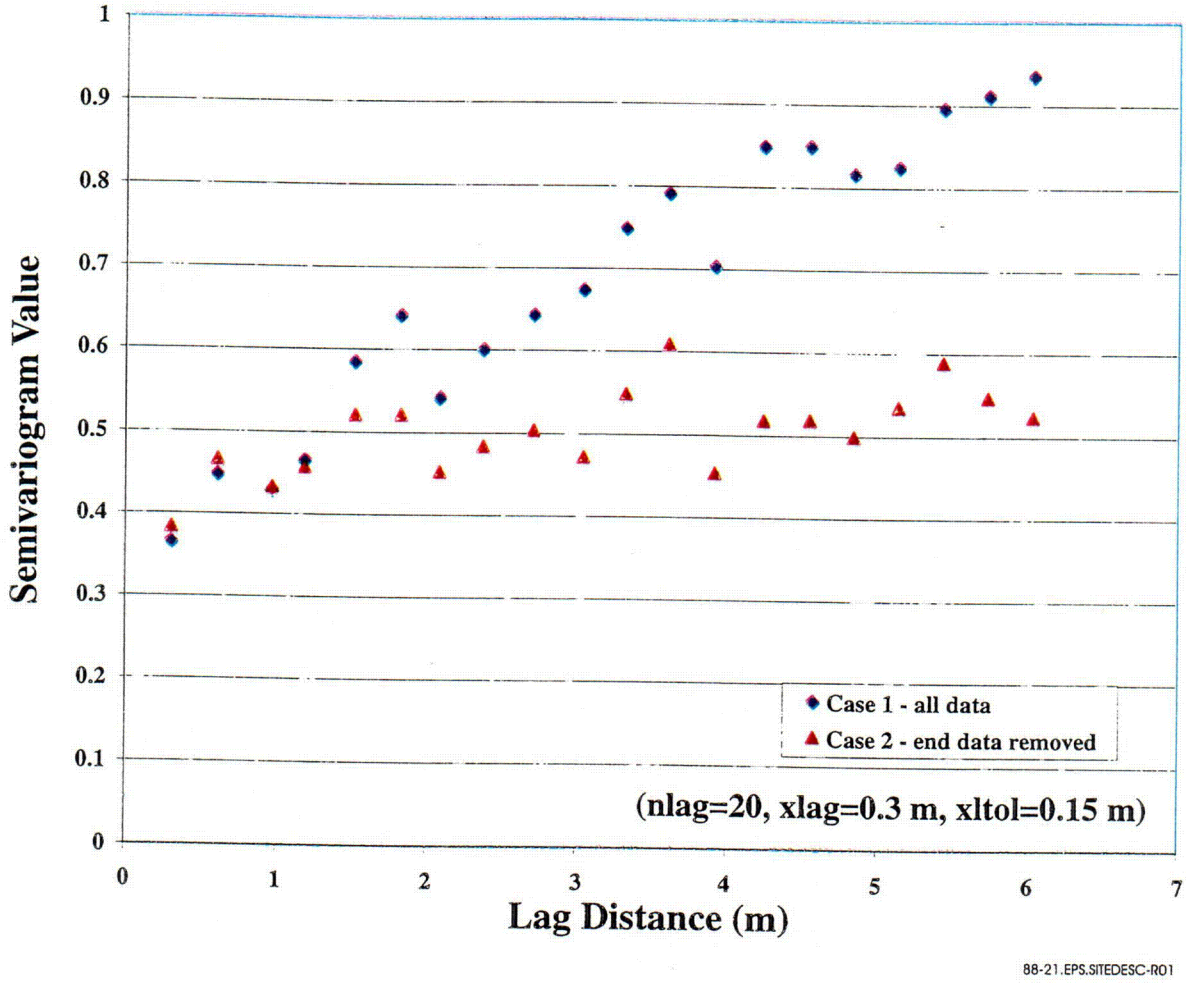

Source: CRWMS M&O (2000s, Figure 15)

Figure 8.8-21. Semivariogram for Log-Air-Permeability Values from Post-Excavation Testing at Niche 3650

C 074

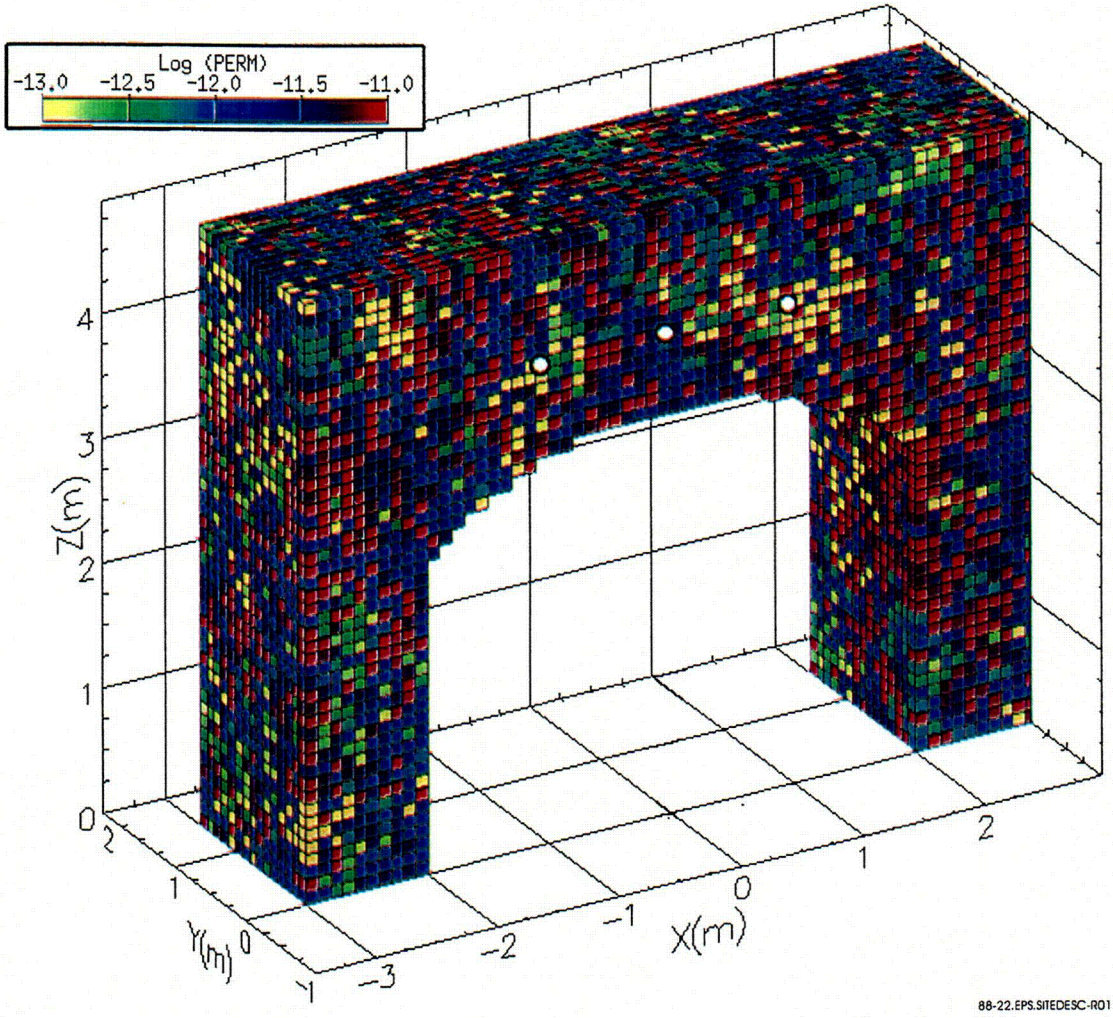

Source: CRWMS M&O (2000s, Figure 18)

Figure 8.8-22. Discretization Grid and Log-Permeability Field for the Three-Dimensional Seepage Model

C075

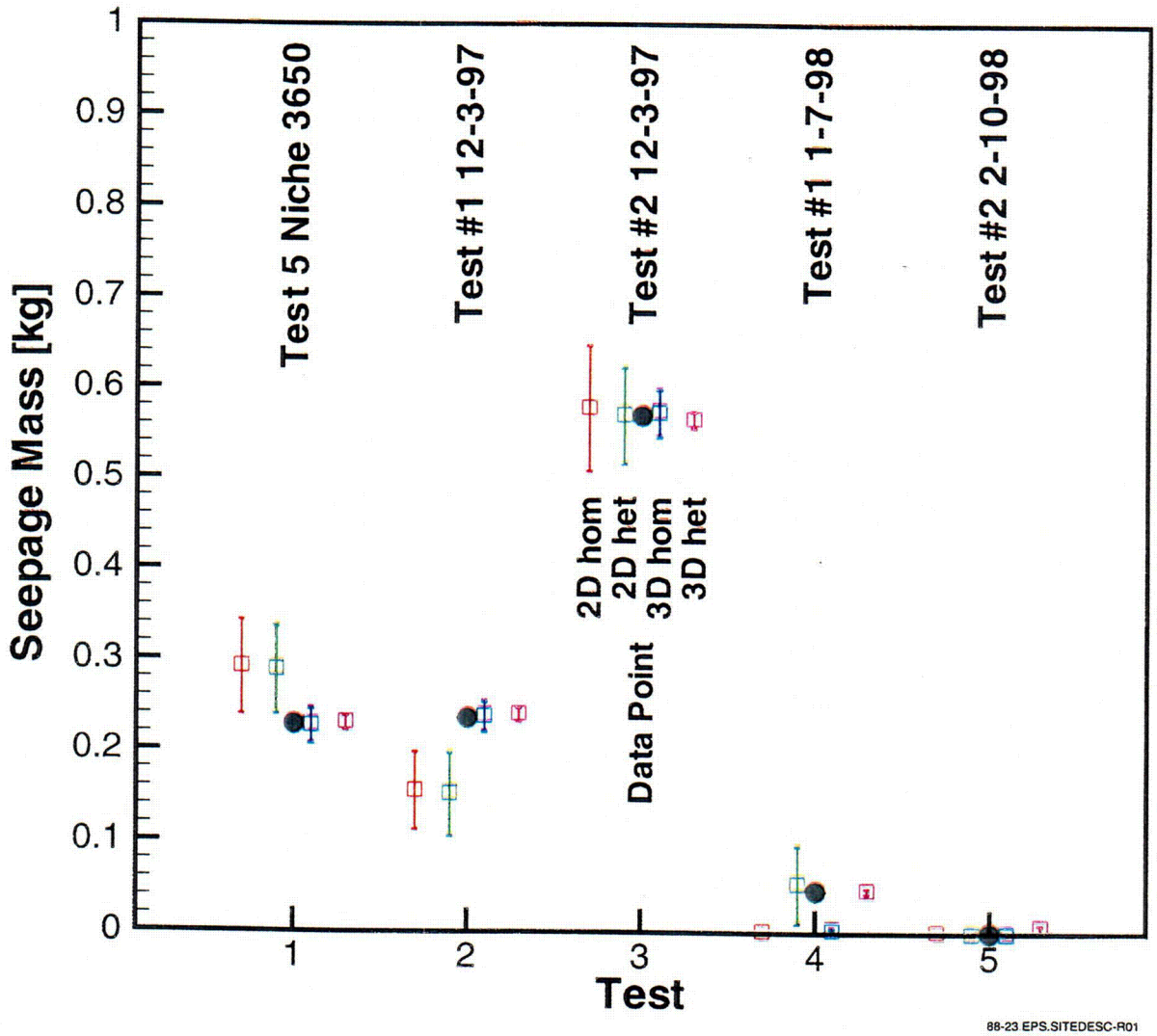

Source: CRWMS M&O (2000s, Figure 19)

NOTE: Circles are measured values; squares are calculated values; 95 percent-error bands indicate prediction uncertainty of calibrated seepage calibration model.

Figure 8.8-23. Comparison of Measured and Calculated Seepage Mass for Five Test Events Simulated in the Inverse Calibration of the Seepage Model

C076

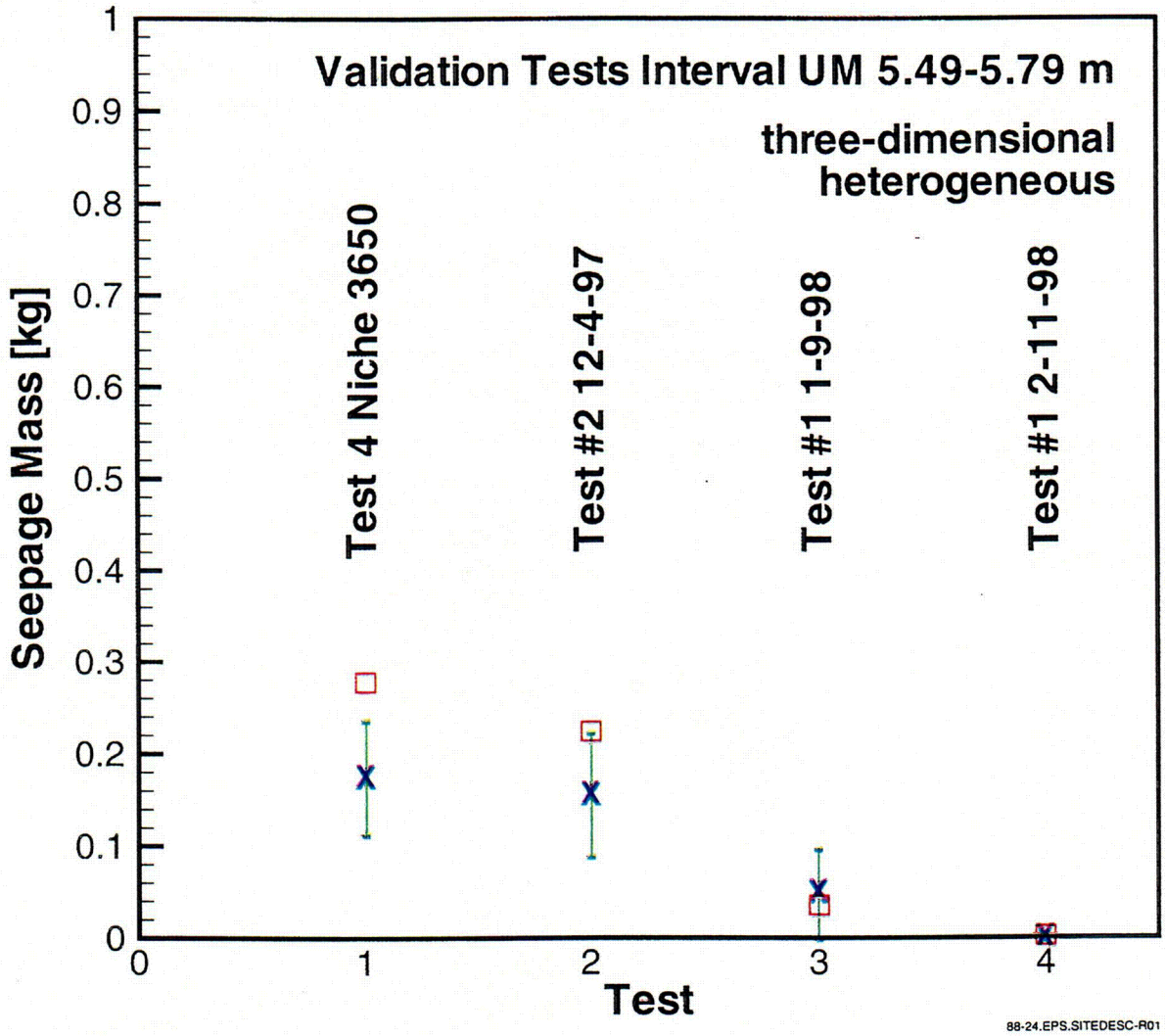

Source: CRWMS M&O (2000s, Figure 61)

NOTE: The seepage mass predicted with the best-estimate parameter set is shown as an X; the measured value is represented by a square; 95 percent error bars are determined by linear-uncertainty propagation analysis.

Figure 8.8-24. Results of the Three-Dimensional Heterogeneous Validation Simulations for the Seepage Model

C077

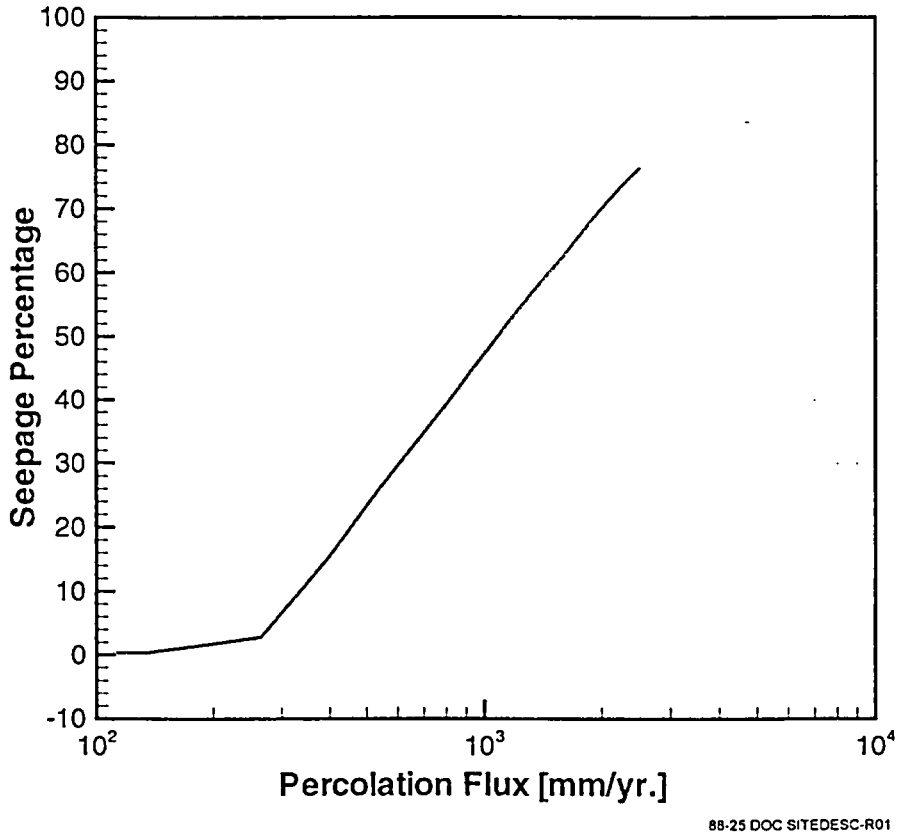

Source: CRWMS M&O (2000s, Figure 27)

Figure 8.8-25. Results of Three-Dimensional Heterogeneous Simulations of a Range of Percolation Fluxes Using the Seepage Model

INTENTIONALLY LEFT BLANK